Towards Universal Integrated Laser Sources with Nonlinear Photonics

Thesis by
Luis M. Ledezma

In Partial Fulfillment of the Requirements for the
Degree of
Doctor of Philosophy

CALIFORNIA INSTITUTE OF TECHNOLOGY
Pasadena, California

2023
Defended May 19, 2023

To my wife,
Vanessa,
and my sons,
Sebastian and *Julian*.

ACKNOWLEDGEMENTS

Sometime in August of 2018, I found myself in Prof. Alireza Marandi's office. I had recently left industry to join JPL as a researcher and I was looking for potential collaborators at Caltech. I was an experienced microwave integrated circuit designer in the area of RF power amplifiers. These are very nonlinear devices so I was used to seeing harmonics appear at multiples of the input frequency. This was understandable: the transistor drain current is a non-linear function of the gate voltage, so you can expand it as a Taylor series; the second order term gives you a second harmonic, and so on. But there was a problem. The largest device I designed was oscillating at half the input frequency, and that was *not* predicted by the Taylor expansion! A friendly senior engineer laughed and said "you have a parametric oscillation." A what!? Such was my first encounter with parametric processes.

At JPL, I was reinventing myself as a photonic integrated circuit designer and had already designed a few simple linear components in silicon photonics by the time I met Alireza. I knew that Alireza's research had something to do with optical parametric oscillators; maybe, working with him, I could leverage my previous experience in nonlinearities and (accidental) parametric oscillators to join the world of photonics. I asked him if he had considered moving some of his research onto an integrated platform. He had. Actually, before moving to Caltech, and in collaboration with Prof. Marko Lončar from Harvard, they had shown outstanding second harmonic generation in a new upcoming integrated platform called *thin-film lithium niobate*. Still, he did not have anyone at Caltech working on that area. We wrote a small proposal together that allowed me to spend some time every week in his lab. Then, we wrote two more small proposals with Ryan Briggs from JPL. With one, we etched the first waveguides of our group. With the other, we did the first periodic poling. Both were unacceptable by today's standards, but they got us started. I must have made a good impression on Alireza because one day he asked me if I would consider applying to Caltech to join his group as a Ph.D. student.

I am very grateful to Alireza for all the guidance and advice that he has given me over all these years. He has an exceptional intuition for technical problems, is an expert in optical experimental techniques, and thinks deeply about how to present our work within a larger context. I have learned much from our interactions and I will be forever in his debt.

I would like to thank professors Hajimiri, Vahala, and Faraon for serving on my committee and for their thoughtful questions and suggestions. It was a pleasure attending Prof. Vahala's classes. He is an excellent teacher, and I owe a significant portion of my formal education in quantum optics to him; after all, he taught a third of all the classes I took at Caltech.

I thank my long-time friends and collaborators at JPL, Mark Taylor and Ezra Long, who understood when I had to abandon their projects to pursue my Ph.D. I also appreciate the generosity and kindness of many other JPLers that provided support in one way or another during these years, including Mahmood Bagheri, Sean Cornish, Uriel Escobar, Siamak Forouhar, Mark Gatti, Stephanie Leifer, Steve Montanez, Jose Velazco, and Lin Yi.

I need to dedicate an entire paragraph to Ryan Briggs from JPL as I cannot overemphasize how much he has helped me. He took me under his wing and was always generous sharing his knowledge about integrated photonics, nanofabrication, laser theory, and measurement techniques. Sometime in December 2018, in Caltech's KNI, I watched over Ryan's shoulder as he etched the first lithium niobate waveguide in our group; that was my very first time inside a cleanroom and the start of my nanofabrication journey.

The nonlinear photonics group led by Alireza is a well-oiled machine of very bright and capable individuals. I have had the opportunity to collaborate directly with Arkadev Roy, Robby Gray, Ryoto Sekine, and Benjamin Gutierrez. All of them have uncannily fast minds and a good set of complimentary skills. Arkadev never stopped surprising me with his breadth of knowledge and his ability to keep up with the state of the art. Robby can analyze complex problems and provide valuable feedback in a matter of seconds. Robby is also one of the kindest humans I have had the pleasure to meet. I was really lucky to count with Ryoto's help during the Covid lockdown, when he took responsibility for all the measurements for our first integrated photonics paper. He has also been instrumental in building the nanofabrication capabilities in our group. I have been working recently with Ben and he is very eager to learn. I cannot wait to see the results of his research in the upcoming years.

I also had the pleasure to work with amazing postdoctoral scholars. Luis Costa (now at JPL) taught me everything I know about running experiments with fibers, and I suspect he has forgotten more things about interferometers than I've ever learned. Raj Nehra's passion for quantum optics is contagious, and he didn't mind explaining the same concepts again and again whenever I asked. Interactions with Qiushi Guo greatly improved my cleanroom practices; my chips were never the same.

While I have had little official collaboration with the rest of the group, I have enjoyed multiple enlightening discussions with Christian Leefmans, Gordon Li, Mingchen Liu, Midya Parto, Elina Sendonaris, James Williams, and Thomas Zacharias. I also had the pleasure to work with Selina Zhou and Louise Schul while they were undergraduates at Caltech. They both managed skillfully the little time they had available for research and have left a very positive impression on me.

I appreciate the help of the KNI staff. They are very knowledgeable and supportive, and make KNI a great place to learn about nanofabrication. I would like to thank the Biological Imaging Facility (BIF) at the Beckman Institute for allowing us to use their two-photon microscope for characterizing our ferroelectric poling. Especial thanks to Dr. Giada Spigolon for all her support and training over all these years. The EE administrative staff was always helpful and made my experience at Caltech rather smooth. Especial thanks to Tanya Owen who helped me navigate every step, from admission, to candidacy, to defense. Also to Liliana Chavarria and Caroline Murphy for day-to-day support.

I would like to thank the NASA Space Technology Graduate Research Opportunities (NSTGRO) program for financial and technical support during my last two-years at Caltech. I'm especially grateful to Mark Stephen from NASA's Goddard Space Flight Center for hosting me during the summer of 2022 and providing valuable insight into some of NASA's needs and perspectives on integrated photonics.

I have enjoyed our collaboration with Prof. Scott Diddams and his groups from UC-Boulder and NIST. He is a towering figure in the field of frequency combs, and it has been an honor to have his feedback in some of my work.

Finally, I must admit with some guilt that by deciding to pursue a Ph.D., I have robbed my family of many hours of my time. I hope that I was able to provide some quality when quantity was not available. My wife, Vanessa, was always supportive and encouraging, especially in times of despair and exhaustion. I couldn't have done it without her and this is as much her achievement as it is mine. I hope that my sons, Sebastian and Julian, will read this and understand what kept me so busy these years. Although, I suspect they liked that daddy was also subject to schoolwork.

ABSTRACT

Lasers are ubiquitous in modern technology with different applications typically requiring different laser wavelengths. However, a given laser can operate only in a relatively narrow spectral region given by the particular material used to build the laser. This leads to using several lasers when several wavelengths are required. Nonlinear photonic devices pose a solution to this problem by transferring energy from single lasers to vast regions of the electromagnetic spectrum. But, despite more than 60 years of development in nonlinear photonics, most nonlinear devices remain large, expensive, and confined to research laboratories.

In this dissertation, we demonstrate a new generation of integrated nonlinear photonic devices based on the quadratic $\chi^{(2)}$ nonlinearity. Using the up-and-coming thin-film lithium niobate platform, we demonstrate ultrafast optical parametric amplifiers, parametric generation of ultrashort mid-infrared pulses, long pulses and frequency combs tunable over an octave bandwidth, and the first $\chi^{(2)}$ CW parametric oscillator directly pumped by a single commercial diode laser. These results represent key milestones towards compact and inexpensive universal laser sources.

PUBLISHED CONTENT AND CONTRIBUTIONS

[1] A. Roy*, **L. Ledezma***, L. Costa, R. Gray, R. Sekine, Q. Guo, M. Liu, R. M. Briggs, and A. Marandi, “Visible-to-mid-IR tunable frequency comb in nanophotonics,” no. arXiv:2212.08723, Dec. 2022. DOI: `10.48550/arXiv.2212.08723`. arXiv: `arXiv:2212.08723`,
L.L. participated in the conception of the project, designed and fabricated the device, and participated in the device characterization and in the writing of the manuscript.
* denotes equal contributions.

[2] **L. Ledezma**, A. Roy, L. Costa, R. Sekine, R. Gray, Q. Guo, R. M. Briggs, and A. Marandi, “Widely-tunable optical parametric oscillator in lithium niobate nanophotonics,” *arXiv:2203.11482 [physics]*, Mar. 2022. arXiv: `2203.11482 [physics]`,
L.L. participated in the conception of the project, designed and fabricated the device, characterized the device and analyzed the data, and lead the writing of the manuscript.

[3] R. Nehra, R. Sekine, **L. Ledezma**, Q. Guo, R. M. Gray, A. Roy, and A. Marandi, “Few-cycle vacuum squeezing in nanophotonics,” *Science*, vol. 377, no. 6612, pp. 1333–1337, Sep. 16, 2022. DOI: `10.1126/science.abo6213`. [Online]. Available: `https://www.science.org/doi/10.1126/science.abo6213`,
L.L. participated in the device design, performed simulations, performed periodic poling during fabrication, and participated in the writing of the manuscript.

[4] Q. Guo*, R. Sekine*, **L. Ledezma***, R. Nehra, D. J. Dean, A. Roy, R. M. Gray, S. Jahani, and A. Marandi, “Femtojoule femtosecond all-optical switching in lithium niobate nanophotonics,” *Nature Photonics*, pp. 1–7, Jul. 2022, ISSN: 1749-4893. DOI: `10.1038/s41566-022-01044-5`,
L.L. participated in the device design and simulations, periodic poling during fabrication, and participated in the writing of the manuscript.
* denotes equal contributions.

[5] G. Li, R. Sekine, R. Nehra, R. M. Gray, **L. Ledezma**, Q. Guo, and A. Marandi, “All-optical ultrafast ReLU function for energy-efficient nanophotonic deep learning,” *Nanophotonics*, May 2, 2022, Publisher: De Gruyter, ISSN: 2192-8614. DOI: `10.1515/nanoph-2022-0137`. [Online]. Available: `https://www.degruyter.com/document/doi/10.1515/nanoph-2022-0137/html`,
L.L. performed device simulations and periodic poling during fabrication.

[6] **L. Ledezma***, R. Sekine*, Q. Guo*, R. Nehra, S. Jahani, and A. Marandi, “Intense optical parametric amplification in dispersion-engineered

nanophotonic lithium niobate waveguides," *Optica*, vol. 9, no. 3, pp. 303–308, Mar. 2022, ISSN: 2334-2536. DOI: 10.1364/OPTICA.442332,
L.L. participated in the conception of the project, designed the device, performed the periodic poling during fabrication, analyzed the data, and lead the writing of the manuscript.
* denotes equal contributions.

[7] A. Roy, R. Nehra, S. Jahani, **L. Ledezma**, C. Langrock, M. Fejer, and A. Marandi, "Temporal walk-off induced dissipative quadratic solitons," *Nature Photonics*, vol. 16, no. 2, pp. 162–168, Feb. 2022, ISSN: 1749-4893. DOI: 10.1038/s41566-021-00942-4,
L.L. performed device simulations and participated in the writing of the manuscript.

[8] T.-H. Wu, **L. Ledezma**, C. Fredrick, P. Sekhar, R. Sekine, Q. Guo, R. Briggs, A. Marandi, and S. A. Diddams, "Ultraviolet to Near-infrared Frequency Comb Generation in Lithium Niobate Nanophotonic Waveguides with Chirped Poling," in *Conference on Lasers and Electro-Optics (2022), Paper FW4J.2*, Optica Publishing Group, May 2022, FW4J.2. DOI: 10.1364/CLEO_QELS.2022.FW4J.2.

[9] A. Roy*, **L. Ledezma***, L. Costa, R. Gray, R. Sekine, Q. Guo, M. Liu, R. M. Briggs, and A. Marandi, "Tunable frequency combs in nanophotonic parametric oscillators from visible to mid-IR," in *Optica Advanced Photonics Congress 2022 (2022), Paper JTh4A.7*, Optica Publishing Group, Jul. 2022, JTh4A.7. DOI: 10.1364/BGPPM.2022.JTh4A.7.

[10] **L. Ledezma**, A. Roy, L. Costa, R. Sekine, R. Gray, Q. Guo, R. Nehra, and A. Marandi, "Widely Tunable Mid-IR Optical Parametric Oscillator in Nanophotonic PPLN," in *2022 Conference on Lasers and Electro-Optics (CLEO)*, May 2022, pp. 1–2.

[11] **L. Ledezma**, R. Nehra, R. Sekine, R. Gray, Q. Guo, and A. Marandi, "30-dB broadband phase-sensitive amplification in integrated lithium niobate," in *OSA Nonlinear Optics 2021 (2021), Paper NW3A.3*, Optica Publishing Group, Aug. 2021, NW3A.3. DOI: 10.1364/NLO.2021.NW3A.3.

[12] **L. Ledezma**, R. Sekine, Q. Guo, R. Nehra, S. Jahani, and A. Marandi, "100 dB/cm broadband optical parametric amplification in dispersion engineered nanophotonic lithium niobate waveguides," in *2021 Conference on Lasers and Electro-Optics (CLEO)*, May 2021, pp. 1–2.

TABLE OF CONTENTS

LIST OF ILLUSTRATIONS

NOMENCLATURE

CW. Continuous wave.

DBR laser. Distributed Bragg reflector laser.

DFB laser. Distributed-feedback laser.

DFG. Difference frequency generation.

FSR. Free-spectral range.

FWM. Four-wave mixing; $\chi^{(3)}$ interaction.

GVD. Group velocity dispersion.

GVM. Group velocity mismatch.

IR. Infrared.

LNOI. Lithium niobate on insulator. Used as a synonym of TFLN.

OPA. Optical parametric amplification/amplifier.

OPG. Optical parametric generation/generator.

OPO. Optical parametric oscillation/oscillator.

OSA. Optical spectrum analyzer.

PPLN. Periodically poled lithium niobate.

QPM. Quasi phase-matching.

SBS. Stimulated Brillouin scattering.

SDE. Stochastic differential equation.

SFG. Sum frequency generation.

SHG. Second harmonic generation.

SOA. Semiconductor optical amplifier.

SPDC. Spontaneous parametric down-conversion.

SRS. Stimulated Raman scattering.

SWIR. Short-wave infrared.

TFLN. Thin-film lithium niobate. Used as a synonym of LNOI.

TWM. Three-wave mixing; $\chi^{(2)}$ interaction.

Chapter 1

INTRODUCTION

"Using a term like nonlinear science is like referring to the bulk of zoology as the study of non-elephant animals."

— Stanisław Ulam

1.1 The promise of parametric nonlinear optics

Lasers have revolutionized our world and it is hard to find a modern technology field that has not been impacted by lasers, with different applications typically requiring different laser wavelengths. For instance, mid-infrared wavelengths are required for spectroscopy, whereas visible lasers can be used to excite atomic transitions. However, a given laser can only operate in a relatively narrow spectral band given by the particular gain medium used to build the laser. So, needing several wavelengths usually means needing several lasers. One dramatic example is the tunable laser spectrometer (TLS) on board NASA's Curiosity Mars Rover [1], shown in Figs. 1.1a,b. It has two interband cascade lasers denoted by black vertical lines in Fig. 1.1c. The first, near 2.78 μm, targets carbon dioxide and water. The second one, near 3.27 μm, targets methane. What if scientists decide to explore spectra at different wavelengths, such as those indicated by the vertical red dashed lines in Figure 1.1c?

One way to address this wavelength rigidity of lasers is to use nonlinear optics. The field of nonlinear optics deals with frequency conversion, so its main application is to modify the wavelength of a laser. We can also use nonlinear optics to transfer light from those places where we have lasers, to those places where we do not. This transfer of energy between different wavelengths can be used to generate optical fields or to amplify already existing ones. I should clarify at this point that the field of nonlinear optics can be roughly divided into parametric and non-parametric processes. In parametric processes, the energy and momentum of the optical fields are conserved, so the quantum-state of the nonlinear material is not altered by interaction with the optical fields. Examples of parametric processes include second-harmonic generation, self-phase modulation, and self-focusing. In contrast, non-parametric processes, like two-photon absorption and saturated absorption, involve excitations of the atoms in the material. We will deal only with parametric processes

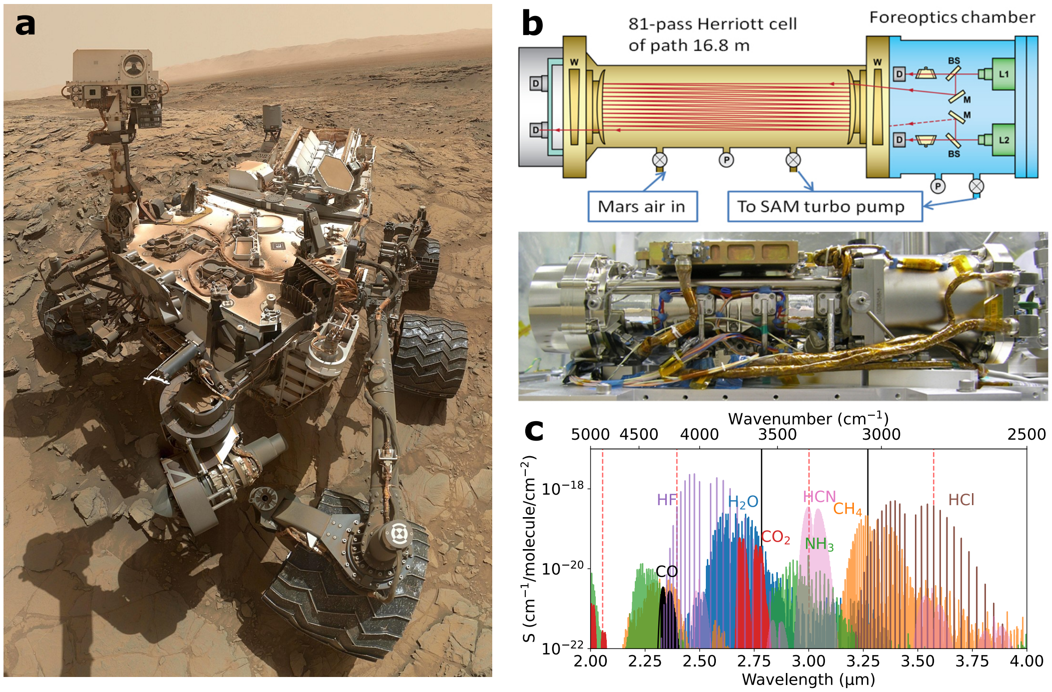

Figure 1.1: **Tunable laser spectrometer aboard NASA's Curiosity Mars rover.** **a**, Self-portrait by Curiosity at the foot of Mount Sharp in October 2015. **b**, Block diagram and photograph of the tunable laser spectrometer (TLS) aboard NASA's Curiosity Mars rover. **c**, Absorption lines of several molecules in the 2.0 - 4.0 μm spectral range. The two black vertical lines denote the two lasers on the TLS near 2.78 μm and 3.27 μm. The red dashed lines indicate other potentially interesting regions that are not reachable with the TLS. Images courtesy NASA/JPL-Caltech.

in this thesis, and in particular, we will deal only with second-order parametric processes.

Parametric nonlinear interactions are more flexible than laser gain, as the entire transparency window of the nonlinear material can be used. This allows coverage of large swaths of the electromagnetic spectrum. In turn, parametric interactions are constrained to energy and momentum conservation. These constraints can be used to design devices targeting specific wavelengths, as we demonstrate with the devices described in this thesis.

The field on nonlinear optics had to wait for the development of the laser due to the weak nature of most nonlinearities. But once the laser was here, the development of nonlinear optics was swift. The laser was demonstrated by Maiman in 1960 [2]. Less than a year later, Franken observed second harmonic generation [3]. In less than a decade, all the remaining fundamental parametric processes had been experimentally observed [4]–[6], the theoretical foundations well established [7]–[9], and the first edition of “Quantum Electronics” by Prof. Yariv already published [10]. It is astonishing then that some six decades later, parametric devices are still large, expensive, and confined to laboratory settings in industry and academia.

Of course, progress *was* was made during this time. Better lasers were developed, new and improved nonlinear materials became available, quasi-phase matching with periodic poling or orientation patterning opened up new degrees of freedom, and optical waveguides provided spatial confinement eliminating inconvenient diffraction effects. All these advances led to more efficient devices, but not necessarily to cheaper or scalable ones.

Further advances in cost and scalability can be gained by confining light to high-index-contrast waveguides capable of featuring sharp turns and bends with low loss, enabling the integration of several components in a single chip. This is the premise behind the photonic integrated circuits revolution of the past two decades. This tight-confinement of optical fields provides two additional advantages for nonlinear optics. First, the small mode areas lead to large intensities increasing the efficiency of nonlinear processes. Second, the waveguide geometry seriously affects the modal dispersion, so the frequency dependence of the propagation constant is not given by the materials used alone, but can be engineered by modifications in the waveguide geometry.

Exploiting strong quadratic nonlinear effects also requires a novel material platform. Common materials in integrated photonics, such as silicon or silicon nitride, have a centrosymmetric crystal structure that forbids second-order nonlinear processes. Efforts to break this symmetry, for instance, by applying a strong static electric field, are under way, but produce relatively weak nonlinear interactions [11]. A more straightforward option is to use a non-centrosymmetric material that readily exhibits a non-zero second-order susceptibility tensor. At the time of writing, *thin-film lithium niobate* represents the most promising integrated platform for quadratic nonlinear photonics. Research in this platform has grown quickly over the past decade, mimicking the early days of nonlinear optics [12].

1.2 Quadratic parametric processes

When the light intensity in the material is high, the polarization density $\mathbf{P}$ can no longer be considered to be proportional to the electric field $\mathbf{E}$. As long as the electric field is not too large, we can expand $\mathbf{P}$ as a Taylor series in $\mathbf{E}$, $\mathbf{P} =$

$\epsilon_0\left(\chi^{(1)}\mathbf{E} + \chi^{(2)}\mathbf{E}^2 + \chi^{(3)}\mathbf{E}^3 + \dots\right)$. In this thesis, we are interested in the first nonlinear term, that is, $\mathbf{P}^{(2)} = \epsilon_0\chi^{(2)}\mathbf{E}^2$. This is the strongest nonlinear term if the second-order tensor $\chi^{(2)}$ is nonzero. In centrosymmetric materials, $\chi^{(2)}$ is identically zero, so the strongest nonlinear term is $\mathbf{P}^{(3)} = \epsilon_0\chi^{(3)}\mathbf{E}^3$.

The nonlinear polarization can be considered a source term in Maxwell's equations (Chapter 2). From the square term $\mathbf{E}^2$, we can identify two fundamental quadratic processes: sum-frequency generation (SFG) and difference-frequency generation (DFG). In both processes, there are a total of three-waves interacting, two inputs and one output. In SFG, two waves at frequencies ω_1 and ω_2 interact to produce a wave at $\omega_3 = \omega_1 + \omega_2$. In DFG, two waves at frequencies ω_2 and ω_3 interact to produce a wave at $\omega_1 = \omega_3 - \omega_2$. Quadratic nonlinear materials are optical frequency mixers!

For the purpose of this thesis, the most important parametric process is optical parametric amplification (OPA). In CW OPA with input signals at frequencies ω_p and $\omega_s < \omega_p$, energy is transferred from a pump wave at frequency ω_p, to the signal wave at frequency ω_s. This is accompanied by the generation of an idler wave at frequency $\omega_i = \omega_p - \omega_s$, so OPA is a DFG process. In this case, the signal will grow exponentially, at least while the pump remains relatively undepleted. This process is phase-insensitive, i.e., the signal will experience gain independently of its phase relative to the pump. This was the special case in which the idler field was zero at the beginning of the process.

The general case of parametric amplification includes all three waves at the input of the amplifier, and it is phase-sensitive, i.e., the gain varies depending on the relative phases of all three waves. This "gain" could also be less than unity, so energy can flow from the signal and idler towards the pump. Of course, this is just sum-frequency generation. When three waves are present on a quadratic nonlinear material, the relative phases between all three waves determine whether DFG or SFG occurs. We say that DFG and SFG are conjugate processes.

Another special case of parametric amplification is *degenerate* parametric amplification. In this case, there are only two inputs, the pump at frequency ω_p, and the signal at frequency $\omega_s = \omega_p/2$. Since the idler and the signal are degenerate with each other, that is, $\omega_i = \omega_s = \omega_p/2$, this is equivalent to having all three waves present at the beginning of the interaction. This process is always phase-sensitive and it is the one we demonstrate in Chapter 3. The conjugate (SFG) process to degenerate OPA is second-harmonic generation, in which energy flows from the signal at $\omega_s = \omega_p/2$ towards the pump at ω_p.

Finally, there is a case of DFG/OPA far more special than the rest: the case in which there is only a single input, the pump at ω_p. The classical coupled wave equations predict no DFG output in this case. But in the laboratory, photons at ω_p will *spontaneously* split into pairs of photons at ω_s and ω_i satisfying $\omega_p = \omega_s + \omega_i$. This result, known as spontaneous parametric downconversion (SPDC), is predicted by quantum mechanics and has its origin in the commutation relation between bosonic creation and annihilation operators [7]. An intuitive picture of this phenomenon is to assume that there are always fluctuating fields at ω_s and ω_i that get amplified by OPA. We review the rigorous background behind this model along with its limitations in Chapter 8. Lastly, when the OPA gain is large enough, these spontaneously generated fields will be amplified to macroscopic levels in a process known as optical parametric generation (OPG) or parametric superfluorescence [6]. We demonstrate this process in Chapter 3 as well.

1.3 Parametric devices

The goal of this thesis is to demonstrate nanophotonic devices based on parametric processes. The first one is the optical parametric amplifier (OPA). Unless otherwise noticed, we will not distinguish between the process and the device and will use OPA to refer to both. We demonstrate an ultrafast degenerate OPA and efficient optical parametric generation (OPG) in Chapter 3.

Shortly after our demonstration of ultrafast OPA, we pursued three projects that showcase the wide range of applicability of OPAs. The first one is an ultrafast switch that can also act as a saturable absorber [13]. The second one is the generation and measurement of wideband squeezed states of light on a single chip [14]. The third one is an all-optical rectified linear unit (ReLU) synthesizer [15]. All of these exploit the phase-sensitive nature of degenerate parametric amplification.

Despite all these exciting demonstrations of OPAs, the most important device demonstrated in this thesis is the optical parametric oscillator (OPO). Its principle of operation is analogous to that of a laser, with an OPA taking the place of the gain medium inside a resonator. The OPA is pumped by a laser at frequency ω_p, while the resonator provides feedback for one or both of the waves generated at frequencies ω_s and ω_i. Spontaneous parametric downconversion starts the emission process, which is continued by parametric amplification, and finally stabilized by gain saturation due to depletion of the pump laser.

The analogy between OPOs and lasers goes only so far. OPOs are fundamentally more flexible than lasers in terms of emission wavelengths, since the output fields can occupy the entire transparency window of the material, only limited by conservation of energy and momentum. Furthermore, an OPO behaves as a *fully inverted two-level* system, which is not physically possible with laser gain. OPOs are also more complex than lasers, due to having three optical waves at different wavelengths, leading to several possible resonator configurations.

1.4 Quasi-phase matching and periodic poling

So far, we have not considered the traveling-wave aspects of parametric processes. The different phase velocities of different interacting fields combined with the phase-sensitive nature of parametric processes lead to back-and-forth switching between the conjugate DFG and SFG processes along the interaction length. This can be quantified by the phase-mismatch $\Delta\beta = \beta_p - \beta_s - \beta_i$, and the corresponding *coherence length*, $l_c = \pi/\Delta\beta$, over which the energy flow switches direction. Left alone, this would lead to negligible net nonlinear interactions.

There are several ways to provide phase matching, but the most versatile is *quasi-phase matching*. The critical insight is that by changing the sign of the nonlinear coefficient every coherence length the switch between conjugate processes can be avoided. The sign of the nonlinear coefficient can be changed by reverting the orientation of the material. There are two main ways to do this. If the material is ferroelectric, then the permanent polarization domains can be inverted by application of a strong electric field. This is known as *periodic poling* and is the method we use in this thesis. The second way to invert the material orientation periodically is known as orientation patterning, and it can be used to quasi-phase match non-ferroelectric nonlinear materials like III-V semiconductors. It consists on epitaxial growth of the material with the desired crystal orientations.

To provide quasi-phase matching with periodic poling, we use a poling period $\Lambda = 2\pi/\Delta\beta$, by applying an electric field across electrodes patterned with the desired period. Figure 1.2a shows pictures of our poling setup at Caltech. A signal generator output pulses in the 100 μs to 5 ms range. These are further amplified to voltage between 300 V and 800 V, depending on the particular chip. The chips are inspected with a two-photon microscope that scans the sample with an ~800 nm femtosecond laser and collects the image through a ~400 nm filter. Fig. 1.2b,c show example images. Black pixels represent areas with no second harmonic generation,

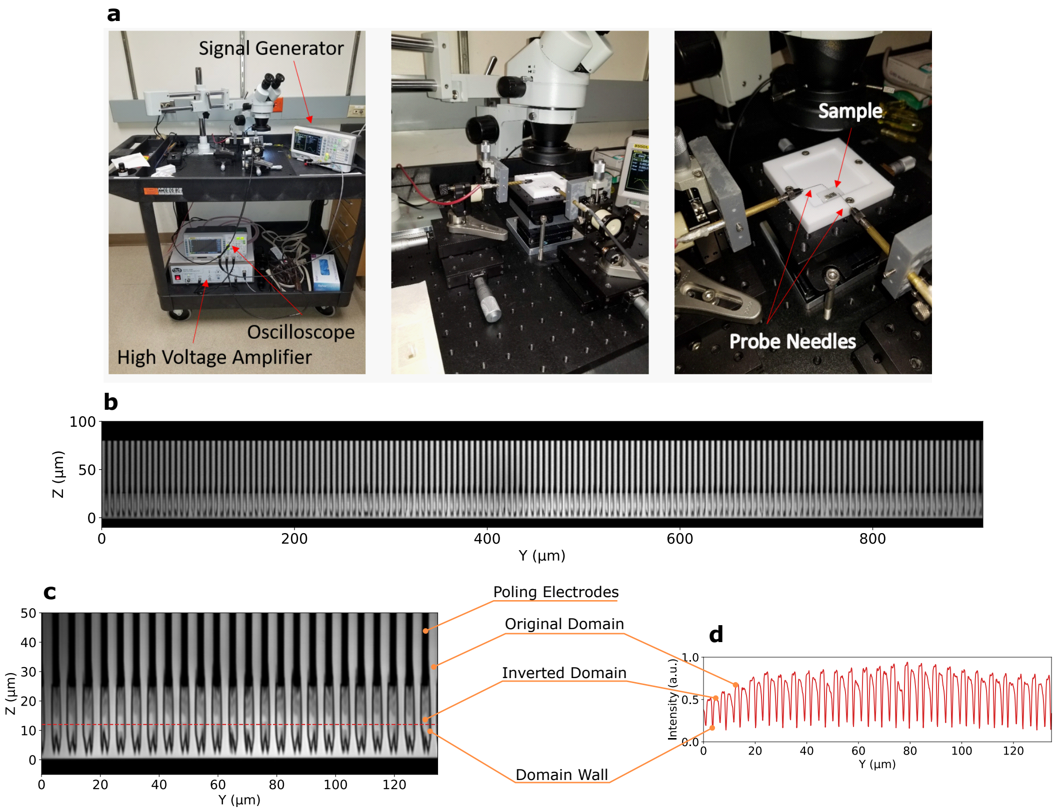

Figure 1.2: **Poling thin-film lithium niobate chips.** **a**, Poling setup at Caltech. A waveform generator is used to produce short pulses (100 μs to 5 ms) which are amplified to a voltage typically between 300 V and 800 V. This voltage is applied to the on-chip poling electrodes through a pair of probe needles. **b**, Second-harmonic microscope image with low magnification, showing uniform poling over the entire field of view. **c**, Zoomed-in image, showing details of the poled domains from a top-view. Dark pixels indicate low second harmonic generation. **d**, Profile trace taken from **c** on the red dashed-line. Low values indicate domain walls due to low net second-harmonic generation.

for instance, on the metallic electrodes. Bright pixels indicate the presence of second-harmonic generation from lithium niobate.

The poling process starts on the proximity of the electrodes fingers shown near the top of Fig. 1.2b,c. Here is where the electric field is most intense and produces domain inversion. The inverted domains then propagate along the optical axis, corresponding to the vertical direction in the pictures. The inverted domains can be identified by the surrounding domain walls that look dark since the net SHG there is low (due to interference between adjacent domains with opposite polarization). The domain walls can be clearly identified in the profile view of Fig. 1.2d, corresponding to the red dashed line of Fig. 1.2c. The brightness change along the image (seen as

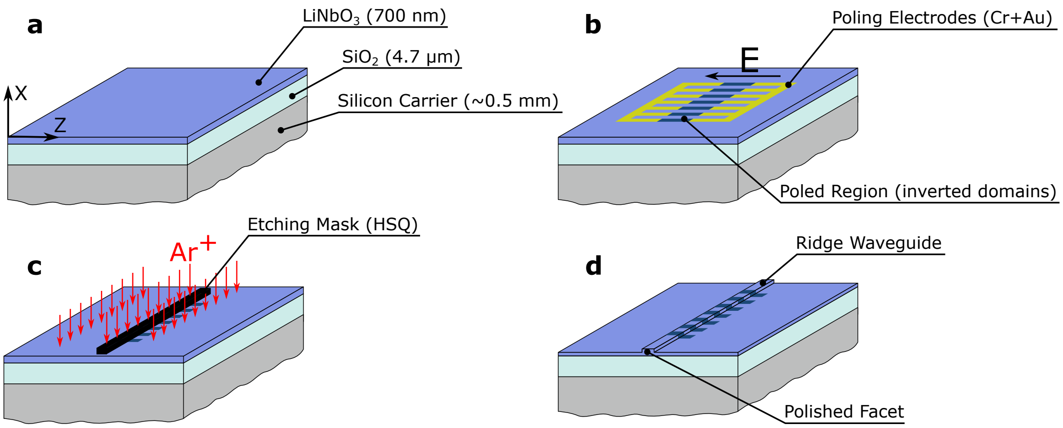

Figure 1.3: **Fabrication process on thin-film lithium niobate.** **a**, Commercially available x-cut wafer. **b**, Poling electrodes are patterned and an electric field is applied across them to produce periodic domain inversion. **c**, After patterning an HSQ mask with e-beam lithography, the pattern is transferred to the lithium niobate layer using Ar$^+$ etching. **d**, The waveguide facets are polished to enable optical coupling.

a large-scale amplitude modulation on Fig. 1.2d) is due to focusing artifacts on the microscope.

1.5 Fabrication process summary

All the devices demonstrated in this dissertation were fabricated at the Kavli Nanoscience Institute at Caltech (KNI). A typical processing flow is shown in Fig. 1.3. We start from a commercially available wafer (Fig. 1.3a), with a 700-nm thick, x-cut, lithium-niobate layer on top of a 4.7 μm silica layer on a silicon carrier. We first deposit metal electrodes (15 nm Cr + 55 nm Au) and perform periodic poling as described above. We then pattern the photonic waveguides on a hydrogen silsesquioxane (HSQ) mask using e-beam lithography. We transfer this pattern to the lithium niobate layer by dry inductively coupled plasma - reactive ion etching with Ar$^+$. We then remove the remaining resist and sidewall redeposition material using an NH_4OH, H_2O_2, H_2O mixture in a 1:1:5 ratio. Finally, we polish the facets of the chip to enable optical coupling.

1.6 Summary of contributions and thesis overview

By the beginning of my time at Caltech, several breakthroughs had been attained in thin-film lithium niobate. Low-loss waveguides had been reported [16], high-quality commercial wafers were available from several suppliers, and ultra-fast electro-optic modulators had been developed [17]. Furthermore, the demonstration of extremely

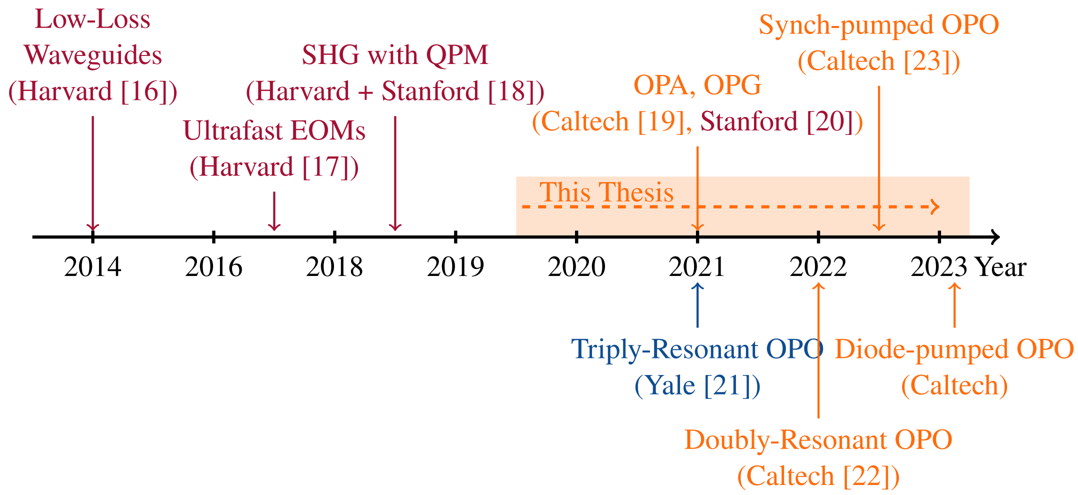

Figure 1.4: **Timeline of thin-film lithium niobate nonlinear photonics.** Only the first demonstration of devices related to this thesis are shown.

efficient, quasi-phase matched, second-harmonic generation [18] foreshadowed a new era of on-chip nonlinear photonics.

The way was paved in front of me: I had to join the race to demonstrate the key remaining parametric processes on nanophotonic chips, including parametric amplification, generation, and oscillation. I used the thin-film lithium niobate material platform to do so. While it is hard to document all the progress in this fast moving field, I have tried to illustrate the contributions of this thesis with respect to the state of the art by showing a timeline of the significant milestones in Fig. 1.4. For brevity, I have only included the first demonstrations (to the best of my knowledge) of specific quadratic nonlinear processes, and have not included other remarkable advances in the field that exploit previously demonstrated capabilities.

It would be a mistake to assume that the main advantage of photonic integration is a smaller size. The devices demonstrated in thin-film lithium niobate outperform the previous generation of parametric devices in almost every metric. The OPA demonstrated in this thesis showcases the largest parametric gain reported, and also the largest gain-bandwidth. The doubly-resonant OPOs can be tuned over vast ranges. The diode-pumped OPO can operate for hours without any active locking. The nanophotonic aspect enables all of this. Higher reliability is a product of the alignment-free nature of the devices. Higher efficiency and gain is due to the same strong confinement that allows sharp bends and turns. Large bandwidths are possible due to the opportunity to engineer the waveguide dispersion.

Nanophotonic lithium niobate tops this list of features with a bonus: it can be poled. This sets it apart from other promising materials, including III–V semiconductors, in that it is much easier to attain quasi-phase matching by poling than by orientation patterning.

I have arranged the chapters in this thesis in a chronological order, mostly because they follow a typical technology development path. We start with a traveling-wave parametric amplifier, which under high-gain conditions leads to optical parametric generation. We present then three optical parametric oscillators that differ mainly by their mode of operation. The first one is pumped with nanosecond pulses featuring peak power levels ranging from tens of milliwatts to several watts. The second one is pumped by a picosecond electro-optic frequency comb. The third one operates in the CW regime and it is pumped by a commercially available distributed Bragg reflector AlGaAs laser. This represents, to the best of my knowledge, the first $\chi^{(2)}$ optical parametric oscillator directly pumped by a compact semiconductor laser diode without the need for bulky isolators or amplifiers.

While most of the dissertation deals with experimental demonstrations of parametric devices in nanophotonics, Chapter 8 explores a rigorous approach to the simulation of spontaneous down-conversion and optical parametric generation. Using phase space methods, we find a set of stochastic differential equations that resemble the classical pulse propagation equations but that are formally equivalent to the full quantum time evolution. This type of simulations is becoming critical with the advent of quantum optics with ultrashort pulses, where a direct quantum simulation in Hilbert space is prohibitively expensive.

References

[1] C. R. Webster and P. R. Mahaffy, "Determining the local abundance of Martian methane and its 13C/12C and D/H isotopic ratios for comparison with related gas and soil analysis on the 2011 Mars Science Laboratory (MSL) mission," *Planetary and Space Science*, Methane on Mars: Current Observations, Interpretation and Future Plans, vol. 59, no. 2, pp. 271–283, Feb. 2011, ISSN: 0032-0633. DOI: `10.1016/j.pss.2010.08.021`.

[2] T. H. Maiman, "Stimulated optical radiation in ruby," *Nature*, vol. 187, no. 4736, pp. 493–494, Aug. 1960, ISSN: 1476-4687. DOI: `10.1038/187493a0`.

[3] P. A. Franken, A. E. Hill, C. W. Peters, and G. Weinreich, "Generation of optical harmonics," *Physical Review Letters*, vol. 7, no. 4, pp. 118–119, Aug. 1961. DOI: `10.1103/PhysRevLett.7.118`.

[4] C. C. Wang and G. W. Racette, “Measurement of parametric gain accompanying optical difference frequency generation,” *Applied Physics Letters*, vol. 6, no. 8, pp. 169–171, Apr. 1965, ISSN: 0003-6951. DOI: `10.1063/1.1754219`.

[5] J. A. Giordmaine and R. C. Miller, “Tunable coherent parametric oscillation in $LiNbO_3$ at optical frequencies,” *Physical Review Letters*, vol. 14, no. 24, pp. 973–976, Jun. 1965. DOI: `10.1103/PhysRevLett.14.973`.

[6] S. E. Harris, M. K. Oshman, and R. L. Byer, “Observation of tunable optical parametric fluorescence,” *Physical Review Letters*, vol. 18, no. 18, pp. 732–734, May 1967. DOI: `10.1103/PhysRevLett.18.732`.

[7] W. H. Louisell, A. Yariv, and A. E. Siegman, “Quantum fluctuations and noise in parametric processes. I.,” *Physical Review*, vol. 124, no. 6, pp. 1646–1654, Dec. 1961. DOI: `10.1103/PhysRev.124.1646`.

[8] J. A. Armstrong, N. Bloembergen, J. Ducuing, and P. S. Pershan, “Interactions between light waves in a nonlinear dielectric,” *Physical Review*, vol. 127, no. 6, pp. 1918–1939, Sep. 1962. DOI: `10.1103/PhysRev.127.1918`.

[9] D. A. Kleinman, “Theory of Optical Parametric Noise,” *Physical Review*, vol. 174, no. 3, pp. 1027–1041, Oct. 1968. DOI: `10.1103/PhysRev.174.1027`.

[10] A. Yariv, *Quantum Electronics*. Wiley, 1967.

[11] D. Heydari, M. Cătuneanu, E. Ng, D. J. Gray, R. Hamerly, J. Mishra, M. Jankowski, M. M. Fejer, K. Jamshidi, and H. Mabuchi, “Degenerate optical parametric amplification in CMOS silicon,” *Optica*, vol. 10, no. 4, pp. 430–437, Apr. 2023, ISSN: 2334-2536. DOI: `10.1364/OPTICA.478702`.

[12] D. Zhu, L. Shao, M. Yu, R. Cheng, B. Desiatov, C. J. Xin, Y. Hu, J. Holzgrafe, S. Ghosh, A. Shams-Ansari, E. Puma, N. Sinclair, C. Reimer, M. Zhang, and M. Lončar, “Integrated photonics on thin-film lithium niobate,” *Advances in Optics and Photonics*, vol. 13, no. 2, pp. 242–352, Jun. 2021, ISSN: 1943-8206. DOI: `10.1364/AOP.411024`.

[13] Q. Guo, R. Sekine, L. Ledezma, R. Nehra, D. J. Dean, A. Roy, R. M. Gray, S. Jahani, and A. Marandi, “Femtojoule femtosecond all-optical switching in lithium niobate nanophotonics,” *Nature Photonics*, pp. 1–7, Jul. 2022, ISSN: 1749-4893. DOI: `10.1038/s41566-022-01044-5`.

[14] R. Nehra, R. Sekine, L. Ledezma, Q. Guo, R. M. Gray, A. Roy, and A. Marandi, “Few-cycle vacuum squeezing in nanophotonics,” *Science*, vol. 377, no. 6612, pp. 1333–1337, Sep. 16, 2022. DOI: `10.1126/science.abo6213`.

[15] G. Li, R. Sekine, R. Nehra, R. M. Gray, L. Ledezma, Q. Guo, and A. Marandi, “All-optical ultrafast ReLU function for energy-efficient nanophotonic deep learning,” *Nanophotonics*, May 2, 2022, Publisher: De Gruyter, ISSN: 2192-8614. DOI: `10.1515/nanoph-2022-0137`.

[16] C. Wang, M. J. Burek, Z. Lin, H. A. Atikian, V. Venkataraman, I.-C. Huang, P. Stark, and M. Lončar, “Integrated high quality factor lithium niobate microdisk resonators,” *Optics Express*, vol. 22, no. 25, pp. 30 924–30 933, Dec. 2014, ISSN: 1094-4087. DOI: `10.1364/OE.22.030924`.

[17] C. Wang, M. Zhang, X. Chen, M. Bertrand, A. Shams-Ansari, S. Chandrasekhar, P. Winzer, and M. Lončar, “Integrated lithium niobate electro-optic modulators operating at CMOS-compatible voltages,” *Nature*, vol. 562, no. 7725, p. 101, Oct. 2018, ISSN: 1476-4687. DOI: `10.1038/s41586-018-0551-y`.

[18] C. Wang, C. Langrock, A. Marandi, M. Jankowski, M. Zhang, B. Desiatov, M. M. Fejer, and M. Lončar, “Ultrahigh-efficiency wavelength conversion in nanophotonic periodically poled lithium niobate waveguides,” *Optica*, vol. 5, no. 11, pp. 1438–1441, Nov. 2018, ISSN: 2334-2536. DOI: `10.1364/OPTICA.5.001438`.

[19] L. Ledezma, R. Sekine, Q. Guo, R. Nehra, S. Jahani, and A. Marandi, “Intense optical parametric amplification in dispersion-engineered nanophotonic lithium niobate waveguides,” *Optica*, vol. 9, no. 3, pp. 303–308, Mar. 2022, ISSN: 2334-2536. DOI: `10.1364/OPTICA.442332`.

[20] M. Jankowski, M. Jankowski, M. Jankowski, N. Jornod, N. Jornod, C. Langrock, B. Desiatov, A. Marandi, M. Lončar, and M. M. Fejer, “Quasi-static optical parametric amplification,” *Optica*, vol. 9, no. 3, pp. 273–279, Mar. 2022, ISSN: 2334-2536. DOI: `10.1364/OPTICA.442550`.

[21] J. Lu, A. A. Sayem, Z. Gong, J. B. Surya, C.-L. Zou, and H. X. Tang, “Ultralow-threshold thin-film lithium niobate optical parametric oscillator,” *Optica*, vol. 8, no. 4, pp. 539–544, Apr. 2021, ISSN: 2334-2536. DOI: `10.1364/OPTICA.418984`.

[22] L. Ledezma, A. Roy, L. Costa, R. Sekine, R. Gray, Q. Guo, R. M. Briggs, and A. Marandi, “Widely-tunable optical parametric oscillator in lithium niobate nanophotonics,” *arXiv:2203.11482 [physics]*, Mar. 2022. arXiv: `2203.11482 [physics]`.

[23] A. Roy, L. Ledezma, L. Costa, R. Gray, R. Sekine, Q. Guo, M. Liu, R. M. Briggs, and A. Marandi, “Visible-to-mid-IR tunable frequency comb in nanophotonics,” *arXiv*, Dec. 2022. DOI: `10.48550/arXiv.2212.08723`.

Chapter 2

BASICS OF NONLINEAR INTERACTIONS IN NANOPHOTONIC WAVEGUIDES

> *"...30 ohms (that gives optimal power handling) does not equal 50, even for relatively large values of 30"*
>
> — Thomas H. Lee*, Planar Microwave Engineering*

In this chapter, we review the basics of nonlinear optics in nanophotonic waveguides, and discuss the key approximations made in our simulations models. They main difference between propagation in highly confining waveguides, and propagation in weakly guiding waveguides, is that the full vectorial nature of the modes need to be considered. However, by appropriate normalization of the fields and overlap integrals, it is possible to recast the nonlinear coupling coefficients in the same form as plane wave interactions.

We also review the derivation of a first-order nonlinear wave propagation equation. Notably, we do not follow the commonly used slowly-varying envelope approximation (SVEA), but instead use a method first described by Fejer [1], and later by Payne and Snyder [2], to get an exact first-order propagation equation directly from Maxwell's equations. How is this possible? The answer is that after an exact set of first-order propagation equations is obtained, a result equivalent to the SVEA is recovered by just neglecting the back-propagating terms. It had been noticed before that the SVEA is related to discarding back-propagating terms [3], but this derivation makes it crystal clear.

Finally, starting from the main propagation equation, we derive the single-envelope equation, the coupled-wave equation, and the CW three-wave-mixing equation. These are the equations that are solved numerically for device design and simulation.

2.1 Waveguide modes

We describe the fields propagating along the z-direction in a single-mode waveguide as

$$\mathbf{E}(\mathbf{r},\omega) = A(z,\omega)\mathbf{e}(x,y)e^{-i\beta z}, \quad \mathbf{H}(\mathbf{r},\omega) = A(z,\omega)\mathbf{h}(x,y)e^{-i\beta z}, \tag{2.1}$$

where $A(z, \omega)$ is the dimensionless amplitude of the mode, $\beta = \beta(\omega)$ is the propagation constant of the mode, and $\mathbf{e}(x, y)$ and $\mathbf{h}(x, y)$ are the modal electric and magnetic fields that can be found with a numerical mode solver. The modal fields of mode m and n satisfy the following orthogonality relation

$$\int_{\infty} \mathbf{e_m} \times \mathbf{h_n^*} \cdot \mathrm{d}\mathbf{S} = \int_{\infty} \mathbf{e_m^*} \times \mathbf{h_n} \cdot \mathrm{d}\mathbf{S} = 2\delta_{mn} P, \tag{2.2}$$

where δ_{mn} is Kronecker delta, and P is a mode normalization constant which we pick as $P = 1$ W or simplicity.

The power carried by a single mode is then:

$$\begin{aligned} \int_{\infty} I(x, y) dx dy &= \int_{\infty} \mathrm{Re}\{S_z(x, y)\} dx dy & (2.3) \\ &= |A(z, \omega)|^2 \int_{\infty} \frac{1}{2} \mathrm{Re}\{\mathbf{e} \times \mathbf{h}^* \cdot \mathbf{z}\} dx dy = P |A(z, \omega)|^2, & (2.4) \end{aligned}$$

where $S_z(x, y)$ is the mode Poynting's vector component in the direction of propagation, and $I(x, y) = \mathrm{Re}\{S_z(x, y)\}$ is the mode intensity. Since we normalize the modal fields $\mathbf{e}(x, y)$ and $\mathbf{h}(x, y)$ such that $P = 1$ W, $|A(z, \omega)|^2$ gives directly the power carried by the mode. We define a mode area (A_{mode}) by the relation $I_{\max} A_{\mathrm{mode}} = P$. The simulated mode area for the waveguide used in our OPOs is plotted in Fig. 2.1(a) as a function of wavelength. It is apparent that large field intensities are achievable with modest power levels, leading to efficient nonlinear interactions. It is convenient to introduce the following dimensionless modal fields $\mathbf{e}'(x, y)$ and $\mathbf{h}'(x, y)$ in order to obtain expressions similar to those of plane-wave interactions [4],

$$\mathbf{e}'(x, y) = \sqrt{\frac{A_{\mathrm{mode}}}{2ZP}} \mathbf{e}(x, y), \qquad \mathbf{h}'(x, y) = \sqrt{\frac{Z A_{\mathrm{mode}}}{2P}} \mathbf{h}(x, y), \tag{2.5}$$

where $Z = (\epsilon_0 c n)^{-1}$ is the modal impedance, and n is the mode effective index.

2.2 Nonlinear polarization

The polarization density $\mathbf{P}$ is in general a function of the applied electric field. If we expand this function as a Taylor expansion we get:

$$\begin{aligned} \mathbf{P} &= \epsilon_0 \Big(\chi^{(1)} \mathbf{E} + \chi^{(2)} : \mathbf{EE} + \chi^{(3)} \vdots \mathbf{EEE} + \ldots \Big) & (2.6) \\ &= \mathbf{P}_{\mathrm{L}} + \mathbf{P}_{\mathrm{NL}}, & (2.7) \end{aligned}$$

where $\mathbf{P}_{\mathrm{L}}$ and $\mathbf{P}_{\mathrm{NL}}$ are the linear and nonlinear components.

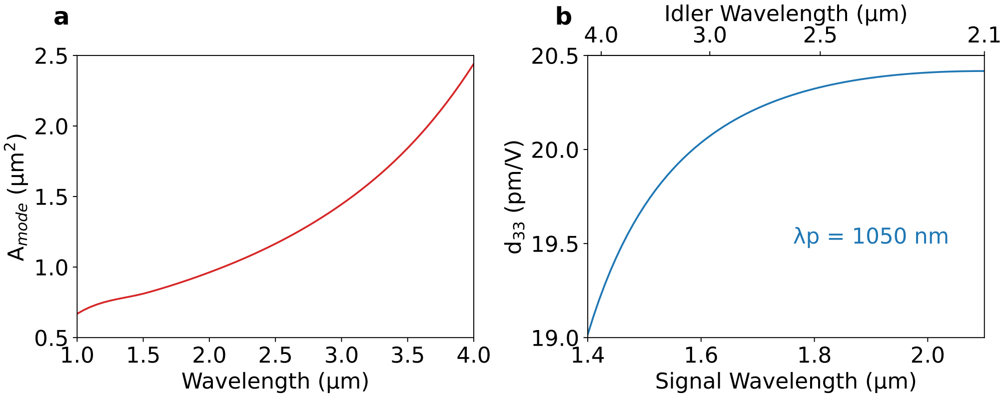

Figure 2.1: **Wavelength dependence of mode area and d$_{33}$.** **(a)** Mode area as a function of wavelength for the waveguide with top width of 2.5 μm and 350 nm of etch depth on a 700-nm-thick lithium niobate layer. **(b)** Largest tensor component (d$_{33}$) of 5% MgO-doped lithium niobate obtained by Miller's delta scaling for a fixed pump wavelength.

In a non-centrosymmetric material with a second-order nonlinear tensor $d_{i,j,k}$, the Cartesian components of the induced nonlinear polarization are

$$P_i(\omega) = 2\epsilon_0 \sum_{jk} \bar{d}_{ijk} \int d_{33}(\omega, \omega')E_j(\omega')E_k(\omega - \omega')d\omega', \tag{2.8}$$

where $i, j, k = \{x, y, z\}$, and $d_{i,j,k}$ has been normalized to its largest component (d_{33}). To account for dispersion in d_{33} we can do a Miller's delta scaling of the measured values reported in [5], as shown in Fig. 2.1(b) for a fixed pump wavelength. Note that if $\chi^{(2)}$ is not dispersive then we can get it out of the integral in Eq. (2.8) to get

$$P_i(\omega) = \epsilon_0 \sum_{jk} \chi^{(2)}_{ijk} \int E_j(\omega')E_k(\omega - \omega')d\omega' = \epsilon_0 \sum_{jk} \chi^{(2)}_{ijk} E_j * E_k, \tag{2.9}$$

bringing this to the time domain yields,

$$P_i(t) = \epsilon_0 \sum_{jk} \chi^{(2)}_{ijk} E_j(t)E_k(t), \tag{2.10}$$

and if the field is linearly polarized along the optical axis of the crystal then it reduces to the scalar form,

$$P(t) = \epsilon_0 \chi^{(2)} E^2(t). \tag{2.11}$$

2.3 The general coupled wave equations

Consider a pulse propagating in a waveguide. The field can be written as a superposition of the waveguide modes as follows:

$$\mathbf{E}(\mathbf{r},\omega) = \sum_m A_m(z,\omega)\mathbf{e_m}(x,y,\omega)e^{-i\beta_m z} = \sum_m A_m(z,\omega)\mathbf{E_m}(\mathbf{r},\omega), \tag{2.12}$$

$$\mathbf{H}(\mathbf{r},\omega) = \sum_m A_m(z,\omega)\mathbf{h_m}(x,y,\omega)e^{-i\beta_m z} = \sum_m A_m(z,\omega)\mathbf{H_m}(\mathbf{r},\omega). \tag{2.13}$$

The total fields satisfy Maxwell's equations,

$$\nabla \times \mathbf{E}(\omega) = -i\omega\mu_0\mathbf{H}(\omega) \tag{2.14}$$

$$\nabla \times \mathbf{H}(\omega) = i\omega\epsilon_0 n^2(\omega)\mathbf{E}(\omega) + i\omega\mathbf{P}_{\mathrm{NL}}(\omega). \tag{2.15}$$

Now, consider the following combination of the cross product between the total fields $(\mathbf{E},\mathbf{H})$ and the conjugated fields of the n-th waveguide mode $\left(\mathbf{E_n^*},\mathbf{H_n^*}\right)$:

$$\nabla \cdot \left(\mathbf{E}\times\mathbf{H_n^*} + \mathbf{E_n^*}\times\mathbf{H}\right) \tag{2.16}$$

$$= (\nabla\times\mathbf{E})\cdot\mathbf{H_n^*} - \mathbf{E}\cdot\nabla\times\mathbf{H_n^*} + \left(\nabla\times\mathbf{E_n^*}\right)\cdot\mathbf{H} - \mathbf{E_n^*}\cdot\nabla\times\mathbf{H}, \tag{2.17}$$

and, after substituting the corresponding Maxwell's equations, we get:

$$\nabla \cdot \left(\mathbf{E}\times\mathbf{H_n^*} + \mathbf{E_n^*}\times\mathbf{H}\right) = -i\omega\mu_0\mathbf{H}\cdot\mathbf{H_n^*} + i\omega\epsilon_0 n^2\mathbf{E}\cdot\mathbf{E_n^*} \tag{2.18}$$

$$+ i\omega\mu_0\mathbf{H_n^*}\cdot\mathbf{H} - \mathbf{E_n^*}\cdot\left(i\omega\epsilon_0 n^2\mathbf{E} + i\omega\mathbf{P}_{\mathrm{NL}}\right) \tag{2.19}$$

$$= -i\omega\mathbf{P}_{\mathrm{NL}}\cdot\mathbf{E_n^*}. \tag{2.20}$$

Integrating both sides over a surface transversal to the propagation direction:

$$\int_A \nabla\cdot\left(\mathbf{E}\times\mathbf{H_n^*} + \mathbf{E_n^*}\times\mathbf{H}\right)\mathrm{d}S = -i\omega\int_A \mathbf{P}_{\mathrm{NL}}\cdot\mathbf{E_n^*}\,\mathrm{d}S\,. \tag{2.21}$$

Now use the following corollary of the divergence theorem:

$$\int_A \nabla\cdot\mathbf{F}\,\mathrm{d}S = \oint_{l(A)} \mathbf{F}\cdot\mathbf{n}\,\mathrm{d}l + \frac{\partial}{\partial z}\int_S \mathbf{F}\cdot\mathrm{d}\mathbf{S}\,, \tag{2.22}$$

to get,

$$\oint_{l(A)} \left(\mathbf{E}\times\mathbf{H_n^*} + \mathbf{E_n^*}\times\mathbf{H}\right)\cdot\mathbf{n}\,\mathrm{d}l + \frac{\partial}{\partial z}\int_S \left(\mathbf{E}\times\mathbf{H_n^*} + \mathbf{E_n^*}\times\mathbf{H}\right)\cdot\mathrm{d}\mathbf{S} \tag{2.23}$$

$$= -i\omega\int_A \mathbf{P}_{\mathrm{NL}}\cdot\mathbf{E_n^*}\,\mathrm{d}S\,. \tag{2.24}$$

If we now extend the area of integration up to infinity, then the first integral on the left-hand side is a vanishing boundary term, so we get,

$$\frac{\partial}{\partial z}\int_S \left(\mathbf{E}\times\mathbf{H_n^*}+\mathbf{E_n^*}\times\mathbf{H}\right)\cdot \mathrm{d}\mathbf{S} = -i\omega\int_A \mathbf{P}_{\mathrm{NL}}\cdot\mathbf{E_n^*}\,\mathrm{d}S\,. \tag{2.25}$$

Now we are ready to substitute the modal expansion of the total fields (2.13), obtaining,

$$\frac{\partial}{\partial z}\left[\sum_m A_m\int_S \left(\mathbf{E_m}\times\mathbf{H_n^*}+\mathbf{E_n^*}\times\mathbf{H_m}\right)\cdot \mathrm{d}\mathbf{S}\right] = -i\omega\int_A \mathbf{P}_{\mathrm{NL}}\cdot\mathbf{E_n^*}\,\mathrm{d}S\,, \tag{2.26}$$

$$\frac{\partial}{\partial z}\left[\sum_m A_m e^{-i(\beta_m-\beta_n)z}\int_S \left(\mathbf{e_m}\times\mathbf{h_n^*}+\mathbf{e_n^*}\times\mathbf{h_m}\right)\cdot \mathrm{d}\mathbf{S}\right] = -i\omega\int_A \mathbf{P}_{\mathrm{NL}}\cdot\mathbf{E_n^*}\,\mathrm{d}S\,. \tag{2.27}$$

We can now use the orthogonality relation (2.2),

$$4\frac{\partial}{\partial z}\left[\sum_m A_m e^{-i(\beta_m-\beta_n)z}N_m(\omega)\delta_{mn}\right] = -i\omega\int_A \mathbf{P}_{\mathrm{NL}}\cdot\mathbf{E_n^*}\,\mathrm{d}S\,, \tag{2.28}$$

$$\frac{\partial A_n}{\partial z} = \frac{-i\omega}{4P}\int_A \mathbf{P}_{\mathrm{NL}}\cdot\mathbf{E_n^*}\,\mathrm{d}S\,. \tag{2.29}$$

Finally, we can substitute the modal field $\mathbf{E_n}(\mathbf{r},\omega) = \mathbf{e_n}(x,y)e^{-i\beta_n z}$, to get the equation for the evolution of the amplitude of the n-th mode:

$$\boxed{\frac{\partial A_n(z,\omega)}{\partial z} = \frac{-i\omega}{4P}e^{i\beta_n z}\int_A \mathbf{P}_{\mathrm{NL}}(\omega)\cdot\mathbf{e_n^*}(\omega)\,\mathrm{d}S\,.} \tag{2.30}$$

This equation tells us how to evolve each modal amplitude for the field at frequency ω. It also works for backward propagating modes by setting the propagation constant of the field to be negative. Note that if $\mathbf{P}_{\mathrm{NL}} = 0$, then the amplitude of the mode is constant, as expected. Also note that the nonlinear polarization, $\mathbf{P}_{\mathrm{NL}}(\omega)$, is a function of the *total* electric field at all frequencies, and through Eq. (2.30) it couples modes to each other.

We now proceed to derive several propagation equations from Eq. (2.30) by expressing $\mathbf{P}_{\mathrm{NL}}(\omega)$ as a function of the appropriate field envelopes. Without loss of generality, we will consider exclusively the case of single-mode waveguides, and we will drop the modal subscript.

2.4 Single-envelope equation

In this case we assume there is a single wideband field. This is a necessary assumption in case of very wideband interactions in which there is no clear distinction between frequency bands, e.g., in supercontinuum generation processes. It also serves as a general propagation equation, in the sense that equations for multiple envelopes can be derived from it. We will follow this approach.

Let us first introduce a fast-evolving envelope $B(z,\omega) = A(z,\omega)e^{-i\beta z}$, so that the electric field becomes

$$\mathbf{E}(\mathbf{r},\omega) = Az,\omega)\mathbf{e_n}(x,y)e^{-i\beta_n z} = B(z,\omega)\mathbf{e_n}(x,y). \tag{2.31}$$

Using (2.8), and assuming that the nonlinear susceptibility is instantaneous, each Cartesian component of the nonlinear polarization becomes

$$P_i(\omega) = \epsilon_0 \sum_{jk} \chi^{(2)}_{ijk} \int B(z,\omega')B(z,\omega-\omega')e_j(\omega')e_k(\omega-\omega')d\omega'. \tag{2.32}$$

To use Eq. (2.30), we need the inner product of this polarization with the modal field $\mathbf{e}^*_\mathbf{m}(\omega)$ integrated over the transversal area of the waveguide,

$$\int \mathbf{e}^*_\mathbf{m} \cdot \mathbf{P}_{\text{NL}}(\omega)\,\mathrm{d}S \tag{2.33}$$

$$= \epsilon_0 \sum_{ijk} \chi^{(2)}_{ijk} \int\int B(z,\omega')B(z,\omega-\omega')e^*_i(\omega)e_j(\omega')e_k(\omega-\omega')d\omega'\,\mathrm{d}S, \tag{2.34}$$

and rearranging,

$$\int B(z,\omega')B(z,\omega-\omega')\left[\epsilon_0 \sum_{ijk} \chi^{(2)}_{ijk} \int e^*_i(\omega)e_j(\omega')e_k(\omega-\omega')\,\mathrm{d}S\right]d\omega', \tag{2.35}$$

the term in brackets depends only on the waveguide modes and not on the amplitudes of the field, so it can be calculated once the material and geometry of the waveguides are known. Let us call this term $X(\omega,\omega')$, to obtain

$$\int \mathbf{e}^*_\mathbf{m} \cdot \mathbf{P}_{\text{NL}}(\omega)\,\mathrm{d}S = \int B(z,\omega')B(z,\omega-\omega')X(\omega,\omega')d\omega', \tag{2.36}$$

$$\text{with } X(\omega,\omega') = \epsilon_0 \sum_{ijk} \chi^{(2)}_{ijk} \int e^*_i(\omega)e_j(\omega')e_k(\omega-\omega')\,\mathrm{d}S. \tag{2.37}$$

Here comes the price to pay for this single envelope method; we will assume that $X(\omega,\omega') = X_0$ (a constant). This is not as bad at it seems. Actually, since we can re-scale the modal fields $\mathbf{e}(x, y, \omega)$ arbitrarily while picking the slack in the normalization constant $P(\omega)$, it may be possible to tailor the frequency dependence of X such that $X(\omega, \omega') \approx X_0$. We then have

$$\int \mathbf{e}_\mathbf{m}^* \cdot \mathbf{P}_\mathrm{NL}(\omega)\,\mathrm{d}S = X_0 \int B(z, \omega')B(z, \omega - \omega')d\omega' = X_0 B(z, \omega) * B(z, \omega), \tag{2.38}$$

which can be evaluated efficiently using Fourier transforms,

$$\int \mathbf{e}_\mathbf{m}^* \cdot \mathbf{P}_\mathrm{NL}(\omega)\,\mathrm{d}S = X_0 \mathcal{F}\left\{b^2(z, t)\right\}. \tag{2.39}$$

Note that this expression is not as neat if we express it in terms of the slowly-evolving amplitude $A(z, \omega)$.

Finally, substituting Eq. (2.39) back into Eq. (2.30) we get,

$$\frac{\partial B(z, \omega)}{\partial z} + i\beta(\omega)B(z, \omega) = \frac{-i\omega X_0}{4P} \mathcal{F}\left\{b^2(z, t)\right\}. \tag{2.40}$$

2.5 CW three-wave mixing

The propagation equations for three monochromatic fields at frequencies ω_1, ω_2 and $\omega_3 = \omega_1 + \omega_2$ can be obtained from Eq. (2.40) by using the fast-evolving envelope

$$B(z, \omega) = B_1(z)\delta(\omega - \omega_1) + B_2(z)\delta(\omega - \omega_2) + B_3(z)\delta(\omega - \omega_3) \tag{2.41}$$

$$+ B_1^*(z)\delta(\omega + \omega_1) + B_2^*(z)\delta(\omega + \omega_2) + B_3^*(z)\delta(\omega + \omega_3), \tag{2.42}$$

which in the time domain reads

$$b(z, t) = B_1(z)e^{i\omega_1 t} + B_2(z)e^{i\omega_2 t} + B_3(z)e^{i\omega_3 t} + \text{c.c.} \tag{2.43}$$

After substituting in Eq. (2.40), all the possible quadratic terms appear, including second-harmonics and optical-rectification of each wave. Ignoring these, and after some algebra, we obtain the following set of equations commonly found in the literature:

$$\frac{\partial A_1}{\partial z} = -i\kappa_1 A_2^* A_3 e^{-i\Delta k z}, \quad \frac{\partial A_2}{\partial z} = -i\kappa_2 A_1^* A_3 e^{-i\Delta k z}, \quad \frac{\partial A_3}{\partial z} = -i\kappa_3 A_1 A_2 e^{i\Delta k z}, \tag{2.44}$$

where $\Delta k = k_3 - k_2 - k_1 - k_g$ is the phase mismatch, and $k_g = 2\pi/\Lambda_\mathrm{QPM}$ is the momentum contribution from a quasi-phase matching grating with period Λ_QPM. The nonlinear coupling coefficients κ_j are given by [4],

$$\kappa_j = \frac{\sqrt{2} d_\mathrm{eff} \omega_j}{\sqrt{\epsilon_0 c^3 n_1 n_2 n_3 A_\mathrm{eff}}}, \tag{2.45}$$

where n is the effective refractive index of the mode, and d_{eff} is the effective nonlinear coefficient, which equals $d_{33} 2/\pi$ when using periodic quasi-phase matching with 50% duty cycle. The effective nonlinear interaction area (A_{eff}) is

$$A_{\text{eff}} = \frac{A_{\text{mode},1} A_{\text{mode},2} A_{\text{mode},3}}{\Theta^2}, \quad \Theta = \left| \sum_{i,j,k} \bar{d}_{i,j,k} \int e'^{*}_{3,i} e'_{2,j} e'_{1,k} \, dxdy \right|, \tag{2.46}$$

where the modal overlap integral (Θ) takes into account the full vectorial nature of the modes in tight-confined waveguides, and we have used the scaled modes from Eq. (2.5).

2.6 Wideband degenerate three-wave mixing

Similarly, we can start from Eq. (2.40) to obtain the propagation equation for two pulses centered at frequencies ω_p and $\omega_s \approx \omega_p/2$. We can identify this interaction as second-harmonic generation or degenerate optical parametric amplification, depending on the direction of energy flow between the pulses.

We start from the fast-evolving envelope:

$$B(z,\omega) = B_p(z,\omega) + B_s(z,\omega), \tag{2.47}$$

where the pump B_p is nonzero only around ω_p, while the signal B_s is nonzero only around $\omega_s = \omega_p/2$. Inserting in Eq. (2.40), neglecting other quadratic processes, like SHG of the pump, SFG of signal and pump, and so on, we obtain

$$\partial_z A_p(z,\omega) = \frac{-i\omega X_0}{8P} e^{i\beta z} B_s(z,\omega) * B_s(z,\omega), \tag{2.48}$$

$$\partial_z A_s(z,\omega) = \frac{-i\omega X_0}{4P} e^{i\beta z} B_s^*(z,-\omega) * B_p(z,\omega), \tag{2.49}$$

where I have used a combination of slow-evolving, $A(z,\omega)$, and fast-evolving, $B(z,\omega)$, envelopes because variety is the spice of life.

References

[1] M. M. Fejer, "Single crystal fibers: Growth dynamics and nonlinear optical interactions," Ph.D. dissertation, Stanford University, Stanford, CA, 1986.

[2] F. Payne and A. Snyder, "The slowly varying envelope approximation in non-linear optics," in *IEE Colloquium on Non-Linear Optical Waveguides*, Jun. 1988, pp. 9/1–9/4.

[3] Y. R. Shen, *Principles of Nonlinear Optics*. Wiley-Interscience, New York, NY, USA, Jan. 1984.

[4] M. Jankowski, C. Langrock, B. Desiatov, A. Marandi, C. Wang, M. Zhang, C. R. Phillips, M. Lončar, and M. M. Fejer, "Ultrabroadband nonlinear optics in nanophotonic periodically poled lithium niobate waveguides," *Optica*, vol. 7, no. 1, pp. 40–46, Jan. 2020, ISSN: 2334-2536. DOI: `10.1364/OPTICA.7.000040`.

[5] I. Shoji, T. Kondo, A. Kitamoto, M. Shirane, and R. Ito, "Absolute scale of second-order nonlinear-optical coefficients," *Journal of the Optical Society of America B*, vol. 14, no. 9, pp. 2268–2294, Sep. 1997, ISSN: 1520-8540. DOI: `10.1364/JOSAB.14.002268`.

Chapter 3

ULTRAFAST OPTICAL PARAMETRIC AMPLIFIERS

> *"Indeed, the last essential quantum-mechanical stage of a measuring apparatus is a high-gain amplifier; it produces an output that we can lay our grubby, classical hands on."*
>
> — Carlton Caves, *Quantum Limits on Noise in Linear Amplifiers*

Amplification is an important element of a wide range of optical systems, from computing [2] and sensing [3] to quantum information processing [4] and communications [5]. In integrated photonics, achieving intense amplification remains an important challenge. In silicon-based platforms, significant attention has been focused on cubic nonlinearities to realize amplification through four-wave mixing (FWM) [6], [7], stimulated Raman scattering (SRS) [8], and stimulated Brillouin scattering (SBS) [9]. Despite recent promising advances, the weak nature of these nonlinearities and the adverse effects of other competing non-linearities hamper the amount of gain and bandwidth associated with these mechanisms. Another option that provides gain in integrated platforms is the semiconductor optical amplifier (SOA). SOAs have evolved in the past decades as one of the leading optical gain mechanisms [10], [11], and heterogeneous integration of III-V SOAs with other platforms, especially silicon, has been one of the most active research directions in integrated photonics [11]. However, their limited bandwidth and integration challenges hinder their utilization in several applications, such as those that require accessing gain in multiple places on a chip. Furthermore, semiconductor gain is not phase sensitive, limiting its use in quantum and communication applications that require noiseless amplification, e.g., processing of quantum microcombs [12] and few-cycle squeezed vacuum [13]. Hence, an integrated platform with a native gain mechanism that enables intense and phase-sensitive optical amplification of ultra-short pulses can address several of the current challenges in photonics.

Quadratic nonlinearities provide an alternative path for achieving strong optical amplification through three-wave mixing [14], [15]. Such processes have been ex-

---

Part of this chapter is adapted from L. Ledezma, R. Sekine, Q. Guo, *et al.*, "Intense optical parametric amplification in dispersion-engineered nanophotonic lithium niobate waveguides," *Optica*, vol. 9, no. 3, pp. 303–308, Mar. 2022, ISSN: 2334-2536. DOI: `10.1364/OPTICA.442332`.

tensively used in bulk optical systems leading to amplification at wavelengths where other gain mechanisms are not easily available [16], [17]. Recently, integrated photonic platforms with strong quadratic nonlinearities have attracted significant attention, as they can provide a range of functionalities unavailable in other platforms [18]–[21]. Examples of these processes include second-harmonic and supercontinuum generation [22], [23], electro-optic modulation [24], [25], quadratic parametric oscillators [26], [27], and bright sources of entangled photons [28]. Despite the recent significant progress, realization of intense optical amplification in quadratically nonlinear integrated photonics has remained elusive.

In integrated photonics, strong quadratic nonlinear interactions have been enabled by the tight spatial confinement of waveguide modes and the possibility of providing momentum conservation through modal [29] or quasi-phase matching [22], [23]. Further enhancement has also been achieved by using resonators [26], [27], however, resonant dynamics associated with the cavity lifetime are typically not appropriate for amplification in many applications, as they limit the gain bandwidth.

In this chapter, I describe an integrated, high-gain, broadband, traveling-wave, optical parametric amplifier based on quadratic nonlinearities. We show phase-sensitive amplification by operating the amplifier at degeneracy. The large parametric gain of our device is enough to amplify quantum fluctuations to macroscopic levels, therefore allowing the amplifier to function as an optical parametric generator of infrared radiation. Our design strategy is based on quasi-phase matching combined with spatio-temporal confinement of pulses in dispersion-engineered lithium niobate waveguides; a combination that is not easily available on other nonlinear photonic platforms.

3.1 Device design and fabrication

We focus on optical parametric amplification (OPA) at degeneracy through three-wave mixing in a $\chi^{(2)}$ waveguide (Fig. 3.1). As shown in Fig. 3.2a, for efficient short-pulse OPA, negligible group velocity dispersion (GVD) at the signal and pump wavelengths (ω_s and ω_p) is required to preserve the temporal confinement of these pulses and hence their high peak intensities along the waveguide. Additionally, the group velocity mismatch (GVM) between the pump and signal frequencies needs to be minimized so that both pulses travel together along the waveguide, maximizing their parametric interaction. The effects of GVD and GVM on the OPA gain spectrum are shown in Fig. 3.2b for a 6-mm-long waveguide for three different

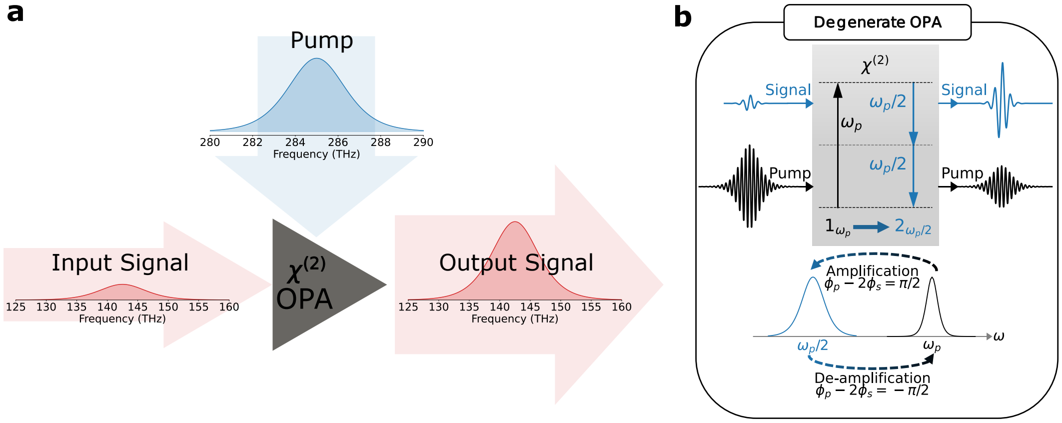

Figure 3.1: **Ultrafast parametric amplification.** **a**, In degenerate optical parametric amplification through three-wave mixing in a $\chi^{(2)}$ medium, energy is transferred from the pump pulse near ω_p to a signal pulse near $\omega_p/2$, providing amplification for the signal. **b**, Corresponding quantum interpretation, in which a pump photon splits into two signal photons. This is a phase-sensitive process; when the relative phase between pump and signal changes by π, the flow of energy reverses, resulting in de-amplification of the signal.

waveguide geometries. These numerical simulations confirm the importance of dispersion engineering for maximizing the gain and bandwidth of OPA around degeneracy.

Some of these results can be intuitively understood in the time domain. A large signal bandwidth implies the amplifier is capable of transferring energy to short signal pulses, for whatever pump used. If the pump is also short, however, then it must propagate at a similar group velocity, otherwise they will overlap only in a small fraction of the waveguide lowering the gain, as shown in the green traces of Fig. 3.2a,b. A low GVM is then needed in order to amplify a short signal with a short pump. If the pump is long, then the GVM restriction can be relaxed at the expense of lower gain.

The effect of dispersion on the gain-bandwidth of pulsed OPAs can also be considered in the frequency domain as originating from the phase-matching bandwidth. Consider the three-wave phase mismatch $\Delta\beta = \beta(\omega_p) - \beta(\omega_s) - \beta(\omega_i)$, expanded in Taylor series around the signal frequency ω_0 and the pump frequency $2\omega_0$. We can use the following frequency deviations: $\Omega_s = \omega_s - \omega_0$, $\Omega_i = \omega_i - \omega_0$, and

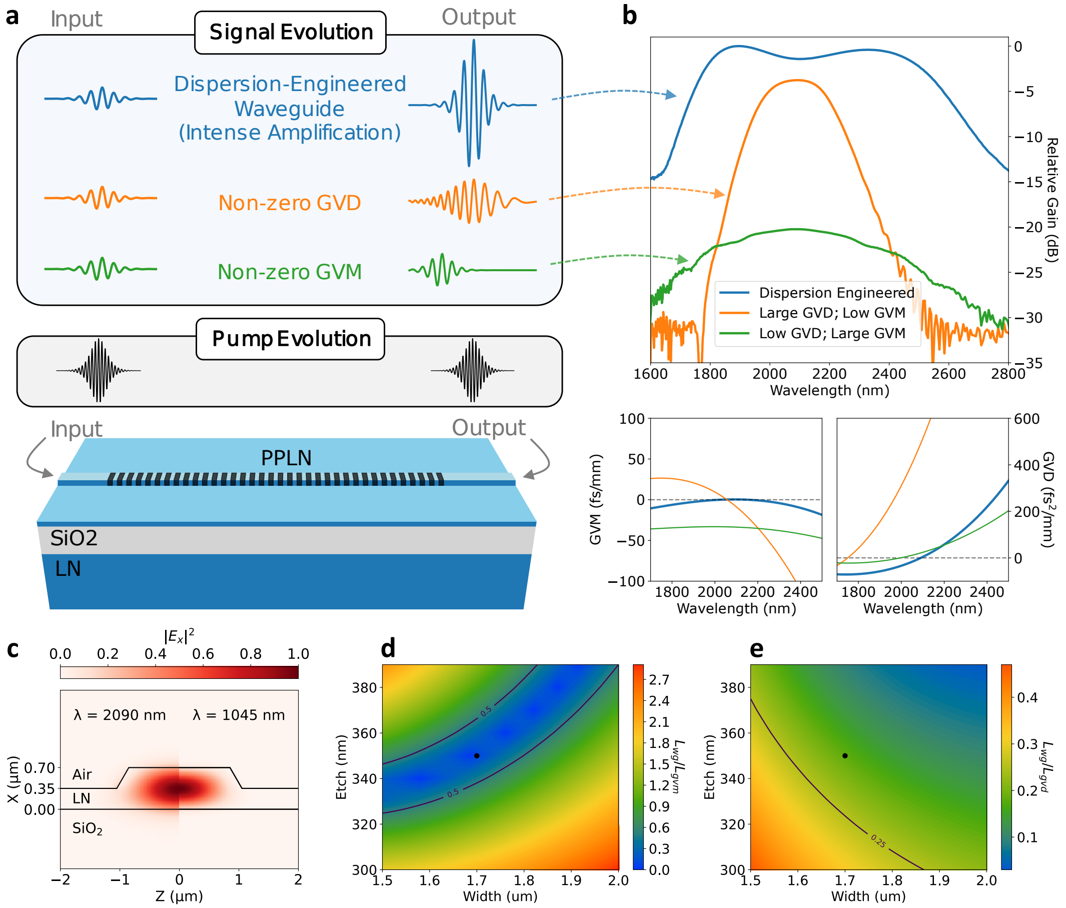

Figure 3.2: **OPA in dispersion-engineered PPLN waveguides.** **a**, In a PPLN waveguide, group velocity dispersion (GVD) leads to pulse temporal spreading with a decrease in peak power and gain, while group velocity mismatch (GVM) causes temporal walk-off between the pump and signal pulses reducing their interaction. **b**, Simulated relative gain spectrum for the three dispersion cases shown in **a** in a 6-mm-long waveguide with 75-fs pump pulses, along with the simulated GVM (with respect to the pump at 1045 nm) and GVD. **c**, Electric field profiles of the fundamental quasi-TE modes for the dispersion-engineered waveguide at the pump and signal wavelengths. **d, e** Geometry maps used for dispersion engineering shown as ratios of waveguide length L_{wg} to walk-off length L_{gvm} and to dispersion length L_{gvd}. The black dot denotes the waveguide geometry we selected.

$\Omega_p = \omega_s + \omega_i - 2\omega_0 = \Omega_s + \Omega_i$, to obtain

$$\begin{aligned}\Delta\beta = {} & \beta(2\omega_0) + \beta'(2\omega_0)\Omega_p + \frac{\beta''(2\omega_0)}{2}\Omega_p^2 \\ & - 2\beta(\omega_0) - \beta'(\omega_0)(\Omega_s + \Omega_i) - \frac{\beta''(\omega_0)}{2}\left(\Omega_s^2 + \Omega_i^2\right),\end{aligned}$$

which, after collecting terms, simplifies to

$$\Delta\beta = \Delta\beta_0 + \mathrm{GVM}\cdot\Omega_p + \mathrm{GVD}(2\omega_0)\cdot\Omega_p^2 - \mathrm{GVD}(\omega_0)\cdot\left(\Omega_s^2+\Omega_i^2\right),$$

where $\mathrm{GVM} = \beta'(2\omega_0) - \beta'(\omega_0)$ and $\mathrm{GVD}(\omega) = \beta''(\omega)/2$. The term $\Delta\beta_0$ is made zero by quasi-phase matching. This expression supports the claim that GVM becomes increasingly important as the pump pulse bandwidth increases, while GVD at the signal and idler limit the bandwidth, even for long pump pulses.

We design our waveguides for degenerate OPA of signal wavelengths around 2 μm, with a pump centered at 1045 nm (Fig. 3.2c). Note the similarity between both field distributions that produces a large modal overlap and a strong nonlinear interaction (see 2). After selecting a thin film thickness of 700 nm, the width and etch depth of the waveguide can be varied to create maps of GVD at 2 μm and GVM between the 1-μm pump and 2-μm signal. We can also factor-in the waveguide length and pulse width by the following procedure. The GVM between signal and pump defines a walk-off length given by $L_{\mathrm{gvm}} = \tau/\mathrm{GVM}$, where τ is the pulse width. If the waveguide width is L_{wg}, then we want to minimize the ratio $L_{\mathrm{wg}}/L_{\mathrm{gvm}}$. A map of this ratio, for $L_{\mathrm{wg}} = 6$ mm and $\tau = 35$ fs, is shown in Fig. 3.2d, along with the corresponding contour levels at 0.5 (where the waveguide is half the walk-off length). Similarly, a dispersion length can be defined as $L_{\mathrm{gvd}} = \tau^2/\mathrm{GVD}$, and the metric would be the ratio $L_{\mathrm{wg}}/L_{\mathrm{gvd}}$. The corresponding map is shown in Fig. 3.2e, along with the contour level at 0.25 (where the waveguide is only a quarter of the dispersion length).

For both contours in Fig. 3.2d,e, the black dot corresponds to our chosen waveguide geometry: a top width of 1,700 nm, an etch depth of 350 nm, and total thin film thickness of 700 nm. This geometry corresponds to the blue trace in Fig. 3.2a,b. The orange trace represents a waveguide with low GVM but large GVD (900-nm top width, 680-nm thickness, 420-nm etch depth), while the green trace is for a waveguide with low GVD but large GVM (3-μm top width, 750-nm thickness, 150-nm etch depth). The GVM and GVD as function of wavelength are shown in the bottom panel of Fig. 3.2b. For a 35-fs-long signal pulse, the optimized waveguide (blue traces) has a dispersion length of more than 30 mm at 2090 nm, and a walk-off length between the pump (1045 nm) and the signal (2090 nm) of almost 100 mm. In comparison, the other two cases have either a short dispersion length of 2 mm at 2090 nm (orange trace) or a short walk-off length of just 1 mm (green trace).

With this dispersion-engineered waveguide, where pump and signal pulses co-propagate at the same group velocity with negligible linear distortion, one can approximate the parametric process with a continuous wave model [23]. At degeneracy, the pump frequency is twice the signal frequency, leading to phase-sensitive amplification. A signal with the correct phase with respect to the pump (Fig. 3.1b) is amplified by a factor of $\exp(2gL)$ in a device of length L. The gain parameter is $g = \sqrt{\eta P_{\mathrm{pump}} - (\Delta k/2)^2}$, where P_{pump} is the pump power, η is the nonlinear efficiency, and Δk is the phase mismatch after quasi-phase matching ($\Delta k = \beta_p - 2\beta_s - 2\pi/\Lambda$), with a constant poling period Λ. When the relative phase between signal and pump is changed by π, the device transitions from a degenerate OPA to a second harmonic generator with energy flowing from the signal to the pump (Fig. 3.1b), resulting in de-amplification of the signal by a factor of $\exp(-2gL)$.

To fabricate the device, we used a commercial wafer (NANOLN), with a 700-nm-thick X-cut MgO-doped LN thin-film on 2-μm-thick SiO_2. The fabrication process begins with periodically poling the chip. The poling electrodes (15 nm Cr/55 nm Au) were patterned using electron beam lithography, electron beam evaporation and metal lift-off. Then, a series of ~300 V pulses were applied across the electrodes to produce periodic domain inversion over a 6-mm length with a period of ~5 μm. We visually inspected the poling quality using second harmonic microscopy (an example image is shown in Fig. 3.3b). The metal electrodes were removed by chemical etching. The waveguides were patterned by e-beam lithography using hydrogen silsesquioxane (HSQ) as the e-beam resist. The pattern was transferred to the LN layer by dry etching with Ar^+ plasma. Finally, the waveguide facets were polished to reduce the coupling losses. A scanning electron microscope (SEM) image of a pair of waveguides near the chip facet is shown in Fig. 3.3c.

3.2 Results and discussion

Optical parametric amplification

We measured the small-signal gain of a 6-mm-long dispersion-engineered periodically poled lithium niobate (PPLN) waveguide with the setup shown in Fig. 3.3a. The 1-μm source (the pump) was a 1-W Yb mode-locked laser that produces nearly transform-limited 75-fs-long pulses at a 250-MHz repetition rate (Menlo Systems Orange). Part of the pump was sent directly to the chip, while the rest was fed into a synchronously pumped degenerate OPO [30] to produce the ~35-fs-long signal pulses centered at 2090 nm. The 1-μm and 2-μm pulses were combined at a dichroic mirror, and coupled into the waveguides using a reflective objective (New-

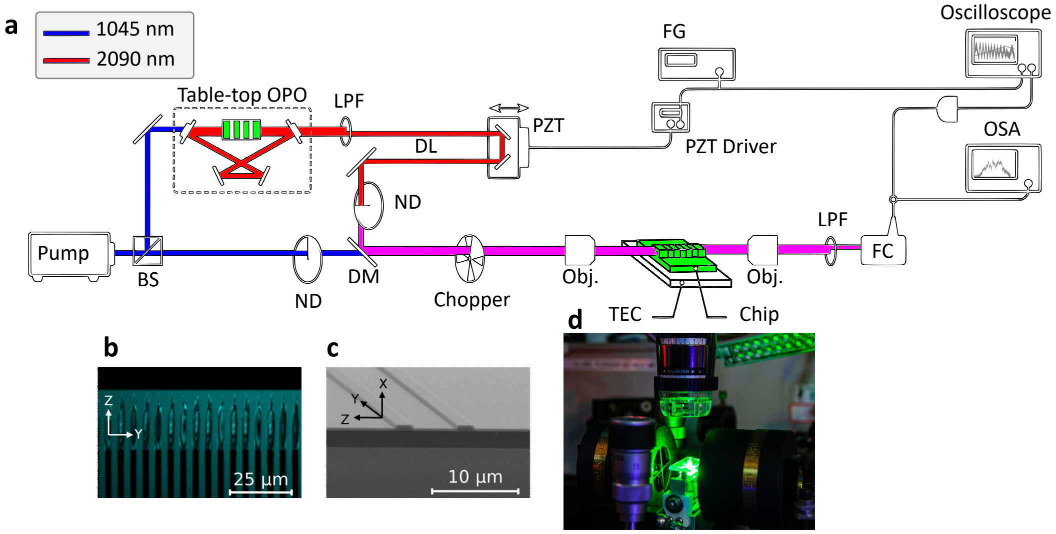

Figure 3.3: **Measuring ultrafast degenerate OPAs. a**, We use ~75-fs pump pulses and ~35-fs signal pulses (generated from a free-space OPO) to characterize the OPA in a dispersion-engineered PPLN waveguide. **b** Second-harmonic microscope image of the periodic poling before waveguide fabrication. **c** Scanning electron microscope image of the chip facets after polishing. **d** Image of the chip under test. The green glow is due to second-harmonic generation of the near-IR pump. BS: beam splitter, OPO: optical parametric oscillator, LPF: long pass filter, DL: optical delay line, PZT: piezoelectric transducer, ND: variable neutral density filter, DM: dichroic mirror, Obj.: reflective objective, TEC: thermoelectric cooling stage, FC: fiber coupler, OSA: optical spectrum analyzer.

port 50102-02). The two pulses were temporally overlapped by adjusting the optical delay line, and their relative phase was scanned by the piezoelectric transducer on the delay line. The chip temperature was set to 15 °C using a thermoelectric cooling stage (TEC) to optimize the phase matching condition. The output of the chip was collected with another reflective objective and the remaining pump power was filtered. The estimation of the input/output coupling losses is described in the next section.

The phase difference between pump and signal is scanned by a piezoelectric transducer (PZT) in a delay arm, and the transmitted signal is measured with a 2-μm detector followed by an oscilloscope (Fig. 3.4a). The ripples show the entire pulse being amplified and de-amplified as the phase of the signal is scanned. We also measured the spectra with an optical spectrum analyzer (OSA) covering 1200 nm to 2400 nm (Yokogawa AQ6375B) with a 2-nm resolution bandwidth for the two cases of pump on and pump off (Fig. 3.4b), with an acquisition time for the OSA being much longer than the periodicity of the phase scan. The ripples in the spectrum with the pump on again confirm the phase-sensitive amplification of the broadband signal.

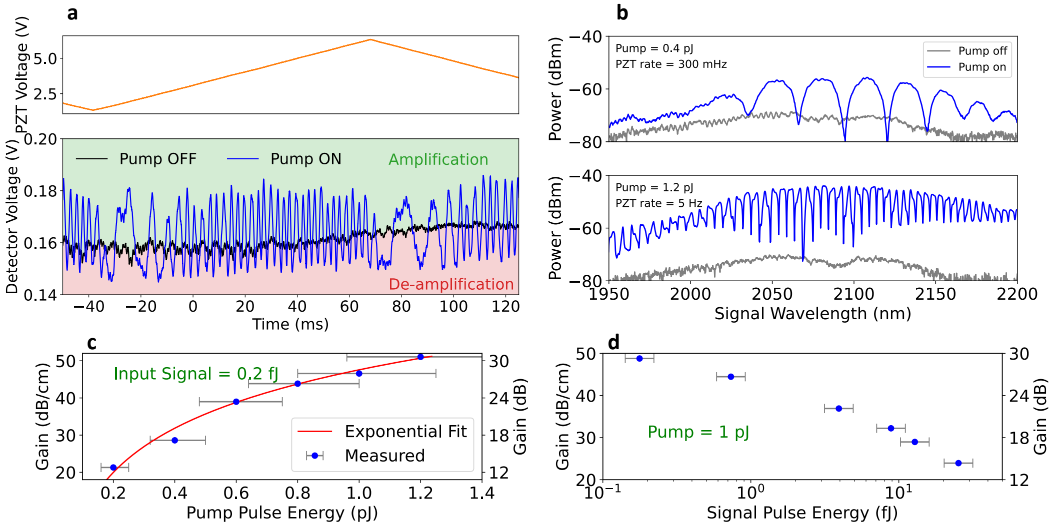

Figure 3.4: **Small-signal gain of the degenerate OPA. a**, Top: triangular voltage driving the PZT in the delay line. Bottom: measured detector output with and without the pump. Ripples demonstrate phase-sensitive amplification of the entire signal pulse. **b**, Measured signal spectrum with and without the pump. Scanning the signal phase while acquiring the spectrum produces ripples due to the phase-sensitive nature of the amplification. **c**, Measured gain versus pump pulse energy along with the expected exponential behavior. Input signal pulse energy in the waveguide is fixed at 0.2 fJ. **d**, Measured gain versus input signal pulse energy for 1-pJ pump pulse energy showing evidence of gain saturation over the entire range of signal energies measured.

We also scan the pump power and record the maximum gain in the measured spectra. Figure 3.4c shows this gain along with the expected exponential response exhibiting a maximum parametric gain of ~30 dB (~50 dB/cm) on the chip for a pump pulse energy of just 1.2 pJ in the waveguide. The agreement with the theoretical estimate suggests that the low-pump-depletion approximation is still valid and larger gain values are available by a further increase in pump energy.

Figure 3.4d shows the behavior of gain versus input signal energy for a pump pulse energy of 1 pJ. The decrease in gain over the entire measured range indicates that the gain is already saturating even for input signal energies as low as 0.2 fJ, which is the lowest energy that we could accurately measure in our setup. This suggest that the amplifier can provide larger levels of gain for signal energies in the aJ range. We explore this possibility in the next section.

Optical Parametric Generation

To measure the largest possible bandwidth and unsaturated gain in our dispersion-engineered PPLN waveguides, we removed the input signal (leaving only vacuum fluctuations present near the 2-μm signal wavelength). When the gain of an OPA is large, spontaneously generated signal photons can grow to macroscopic levels in a process known as parametric superfluorescence or optical parametric generation (OPG), with an expected number of photons at the output given by [31] $\langle n \rangle = \sinh^2(gL) \approx 0.25\exp(2gL)$. For a fixed device length, the rate of growth of OPG pulse energy versus pump pulse energy can be used to extract the OPA gain as follows. The number of OPG photons is $\langle n \rangle = \sinh^2(gL)$, which for parametric gains larger than ~10 dB can be approximated well by $0.25\exp(2gL)$. The OPG energy is proportional to $\langle n \rangle$, so we have $E_{\mathrm{OPG}} = a\exp(2gL) = a\exp\left(b\sqrt{E_{\mathrm{pump}}}\right)$, where a is the overall detection efficiency (including output coupling losses) and b is a constant that depends on factors such as input coupling losses, pump peak-to-average power ratio, waveguide length, and waveguide nonlinear efficiency. We have also assumed that $g \approx \sqrt{\eta P_{\mathrm{pump}}} \propto \sqrt{E_{\mathrm{pump}}}$ within the gain-bandwidth. The measured OPG energy can be fitted to an exponential versus $\sqrt{E_{\mathrm{pump}}}$ to extract a and b. This leads to an estimated OPA gain for degenerate operation given by $G_s = \exp(2gL) = E_{\mathrm{OPG}}/a$. This method of characterization has the additional advantage of not requiring a coherent input signal, and hence the output pulses reveal the full gain bandwidth of the amplifier. Removing the input signal also maximizes the dynamic range of operation of the OPA, eliminating gain saturation effects for a large range of pump levels up to the OPG threshold. For larger pump energies, it is possible to operate the OPG in the saturated regime where high efficiency broadband downconversion can be followed by spectral broadening [32].

To confirm the validity of such a simplified model, we compared the results of pulsed simulations with the CW theory. These are expected to agree on the quasi-static regime of low GVM and low-GVD in which our waveguide operates. Seeding the OPA with an input noise having an energy of half-a-photon per frequency mode, and a uniformly distributed random phase, has been known to provide the same average signal output power as the quantum mechanical solution [33]. This is equivalent to neglecting thermal excitations and modeling the remaining vacuum fluctuations as complex Gaussian random variables with zero mean and a variance [34] of half-a-photon. Fig. 3.5a shows the simulated average output power (integrated from 1,600 nm to 3,000 nm) for the 6-mm-long dispersion-engineered waveguide, along with the expected curve from the CW theory and our measured data. The simulation

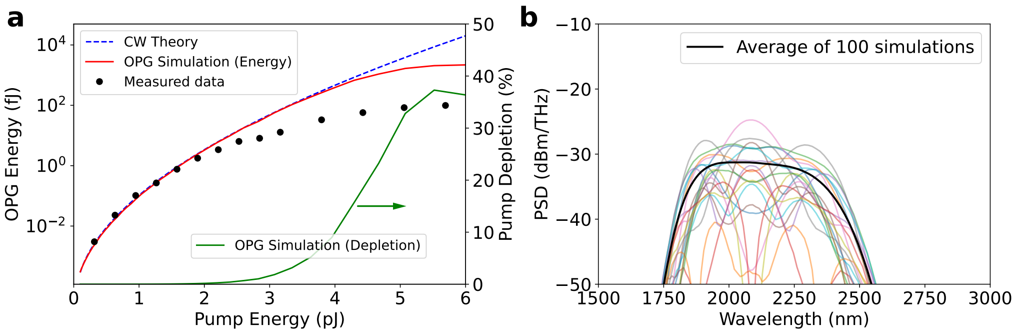

Figure 3.5: **Numerical simulation of optical parametric generation.** **a**, Simulated OPG energy as a function of pump energy along with the CW theory and measured data. The pump is a 100-fs-long hyperbolic secant pulse center at 1045 nm. The results are the average of 100 simulations. In each simulation, the input signal is a realization of a complex Gaussian random variable with zero mean and half-a-photon variance. The simulation results deviate from the CW theory for pump energy levels above ~4 pJ beyond which efficient parametric generation occurs and the no-pump-depletion approximation is no longer valid. The simulated pump depletion level ($P_{\mathrm{OPG}}/P_{\mathrm{pump}}$) is shown on the right hand axis. **b**, Output power spectral density for 20 OPG simulations illustrating its stochastic nature, as well as the average for 100 simulations.

deviates from the theory at pump energies larger than 4 pJ due to efficient parametric generation (OPG) producing pump depletion (also shown in Fig. 3.5a). The simulations results shown in Fig. 3.5a are the ensemble average of 100 simulations, each simulation producing a different result due to the stochastic nature of the input signal. This is illustrated in Fig. 3.5b, where the output spectra OPG for a pump energy of 3 pJ is shown for the first 20 simulations along with the average of 100 simulations.

We characterized our 6-mm-long waveguide through an OPG measurement using the setup from Fig. 3.3a without the input signal path to the chip. The input/output coupling losses were estimated based on a combination of linear and non-linear measurements as follows. Comparing the optical power before and after the chip gives the total loss $L_t = L_i + L_{wg} + L_o$, where L_i is the input coupling loss, L_{wg} is the waveguide loss, and L_o is the output coupling loss. We estimated the waveguide loss, L_{wg}, to be much less than 1 dB based on Q-factor measurements in other chips using the same fabrication process. Since the total loss L_t is ~29 dB (at 2 μm) we neglect the waveguide loss in what follows.

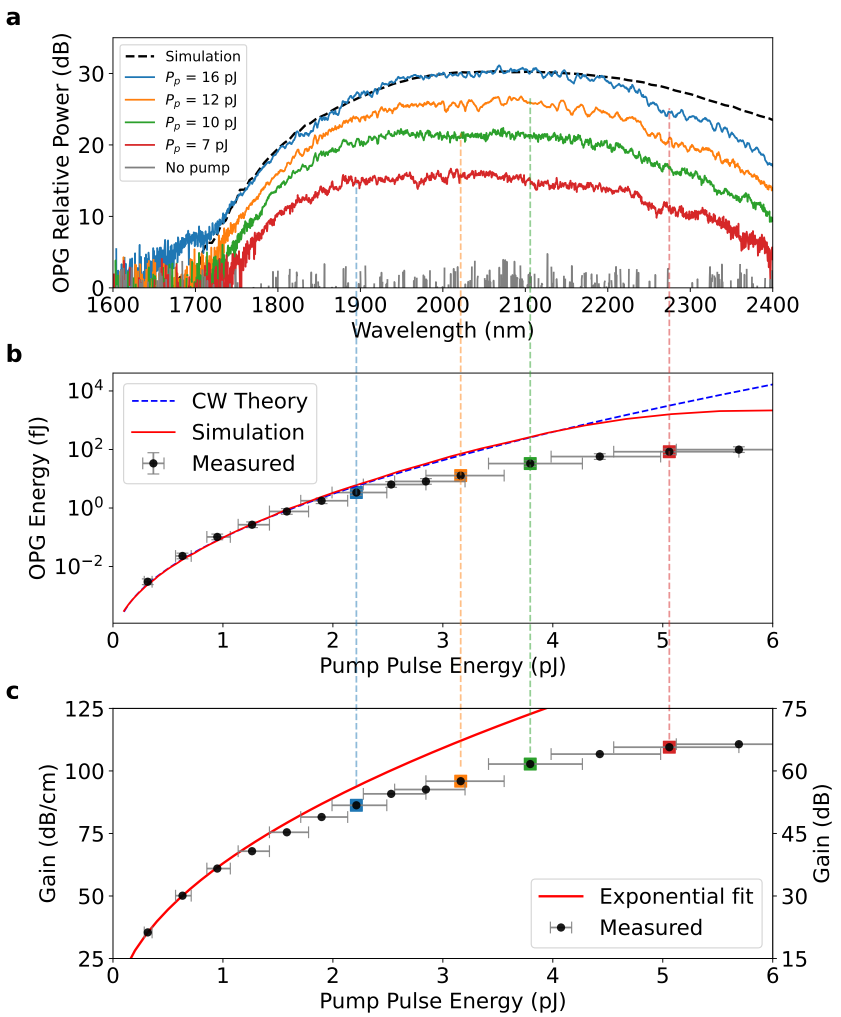

Figure 3.6: **Measurements in the large-gain regime through optical parametric generation.** **a**, OPG spectra for different pump energies. Dashed line is average of 100 numerical simulations using a semi-classical quantum noise seed. The OPG power is referenced to the noise floor of the analyzer. All traces are taken with a 2-nm resolution bandwidth. **b**, OPG pulse energy versus pump pulse energy in the waveguide for a 6-mm-long device. **c**, Extracted parametric gain versus pump pulse energy.

As explained above, the OPG data can be used to estimate the gain $G_s = \exp(2gL)$ without any knowledge of the input/output coefficients. This is because this gain depends only on the rate of growth of the OPG power, and not on its absolute value. We also know that the expected number of photons generated during OPG is given by $\langle n \rangle = \sinh^2(gL) \approx 0.25 \exp(2gL) = 0.25G_s$. Thus, by estimating G_s, we are also estimating the average number of photons generated, from which the OPG power in the waveguide follows immediately: $P_{\text{OPG}} = \hbar\omega\langle n \rangle f_{rep}$. Comparing this

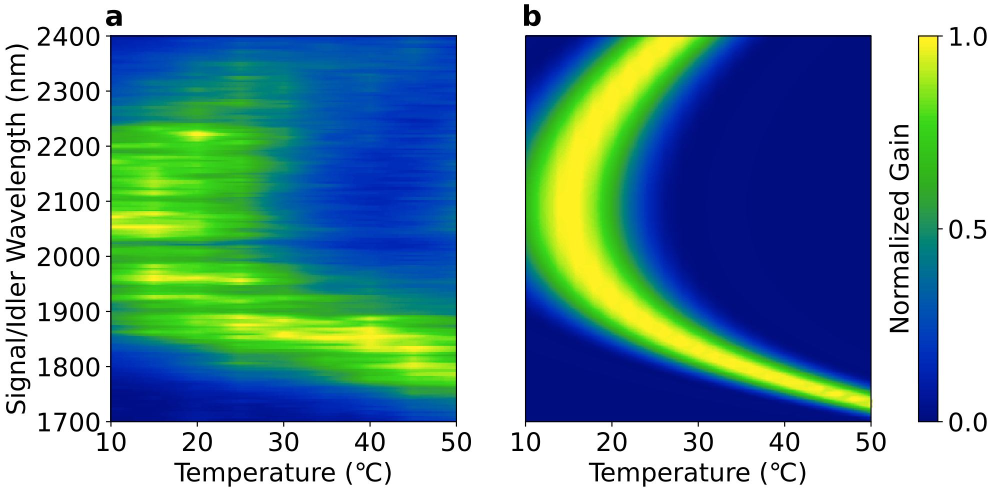

Figure 3.7: **Optical parametric generation spectra.** **a**, Measured normalized OPG spectra in linear units as a function of chip temperature. **b**, Simulated normalized gain in linear units as a function of signal/idler wavelength.

expected power with the measured power gives us a total output collection efficiency of 5.85 dB at 2 μm. This corresponds to 26 % output coupling efficiency, which compares well with output coupling losses in similar waveguides estimated by other methods [32].

Subtracting this output coupling loss from the total throughput loss gives us an input coupling loss at 2 μm of ~23 dB, which is considerably larger than the output coupling loss. This is expected since only the power coupled to the fundamental TE mode is considered at the input, while most of the radiated modes are expected to be collected by the objective at the output. At 1 μm, we assume that the output coupling loss is also 5.85 dB, since we use a low-dispersion metallic collective objective. The measured throughput loss at 1 μm is ~31 dB, so the input coupling loss was estimated to be ~25 dB. The input coupling loss at 1 μm is expected to be larger than that at 2 μm due to the corresponding mode sizes.

Figure 3.6a shows several measured output spectra for different pump pulse energies along with the average simulated spectra described above. The total measured gain bandwidth (at 10 dB below the peak) exceeds 600 nm. The output OPG pulse energy as a function of the pump pulse energy in the waveguide is displayed in Fig. 3.6b. The exponential growth of the signal as a function of pump pulse energy is used to accurately extract the parametric gain as described above.

The extracted gain is shown in Fig. 3.6c, exceeding 66 dB on the chip for the 6-mm-long waveguide (110 dB/cm) with less than 6 pJ of estimated pump pulse energy in the waveguide. The departure from the exponential trend at higher pump powers occurs before the 10% pump depletion level (see Fig. 3.5a) and it is likely the result of other nonlinear effects that become relevant at high gain regimes, including loss through parasitic green generation (visible in the image of Fig. 3.3). Further studies are necessary to identify and inhibit such processes, but it is important to note that these issues do not limit the use of the amplifier, since gain levels beyond 50 dB are reached before entering this region.

Figure 3.7a shows the measured OPG spectrum as a function of the chip temperature. This measurement is compared with the theoretical OPA gain as a function of poling period shown in Fig. 3.7b, confirming the transition from broadband degenerate to narrowband non-degenerate regime, which happens above 30 °C in the experiment. Achieving OPG in the non-degenerate regime confirms having a phase-insensitive parametric gain with similar magnitude (~100 dB/cm), which can be a useful on-chip resource for quantum and classical photonics [35], [36].

3.3 Conclusion

We have demonstrated an on-chip optical parametric amplifier, with gain levels exceeding 30 dB for weak input femtosecond pulses, and 60 dB for vacuum fluctuations, over more than 600 nm of bandwidth around 2 μm, using a waveguide that is only 6-mm-long. Furthermore, we have shown that we can operate the amplifier near degeneracy to obtain phase-sensitive amplification. Our results represent a paradigm shift for on-chip optical amplifiers, as shown in Fig. 3.8. The bandwidth and gain figures used to generate Fig. 3.8 are displayed in Table 3.3 along with the corresponding references. Previous works include only on-chip traveling-wave amplifiers. We have striven to include the best and most recent results, but not all publications report enough data to extract 3 dB bandwidth values and could not be added to the comparison. To estimate the bandwidth of the FWM cases we have added together the signal and idler bandwidths.

The magnitude of the OPA gain we obtain exceeds the reported gain by cubic nonlinearities and is comparable to what can be achieved with SOAs. The OPA bandwidth is significantly broader than other mechanisms. Currently, the maximum measured gain per unit length is limited by the maximum pump pulse energy that we can safely couple into the waveguide, since the input coupling loss is ~25 dB. Improving

Table 3.1: Comparison of on-chip amplifiers gain and bandwidth

Type	Length	Gain		Signal	3-dB Bandwidth (Signal + Idler)		Ref.
		Absolute	Normalized	Wavelength	Absolute	Relative	
$\chi^{(2)}$	**6 mm**	**62 dB**	**104 dB/cm**	**2090 nm**	**380 nm (26 THz)**	**18.2 %**	**[1]**
$\chi^{(2)}$	12 mm	100 dB	83 dB/cm	2700 nm	10 nm (1.64 THz)	0.4 %	[37]
SOA	1.2 mm	25.5 dB	213 dB/cm	1575 nm	34 nm (4.11 THz)	2.2 %	[38]
SOA	2 mm	13 dB	65 dB/cm	2010 nm	75 nm (5.6 THz)	3.7 %	[39]
SOA	2 mm	25 dB	125 dB/cm	1550 nm	69 nm (8.1 THz)	4.5 %	[11]
FWM $\chi^{(3)}$	4 mm	25.4 dB	63.5 dB/cm	2170 nm	50 nm (3.18 THz)	2.3 %	[6]
FWM $\chi^{(3)}$	2 cm	45 dB	22.5 dB/cm	2170 nm	150 nm (9.5 THz)	6.9 %	[40]
FWM $\chi^{(3)}$	1.7 cm	13.9 dB	8.2 dB/cm	1550 nm	40 nm (5 THz)	2.7 %	[41]
SBS	2.9 cm	5.2 dB	1.8 dB/cm	1550 nm	< 50 MHz	$\ll$ 0.1 %	[9]
SRS	4.6 cm	2.3dB dB	0.5 dB/cm	1545 nm	80 GHz	< 0.1 %	[42]
Er^+ doped	3.6 cm	18 dB	5 dB/cm	1530 nm	20 nm (2.56 THz)	1.3 %	[43]
$C\chi^{(2)}$	2 cm	38.3 dB	19.2 dB/cm	1550 nm	+14 THz	7.2 %	[44]

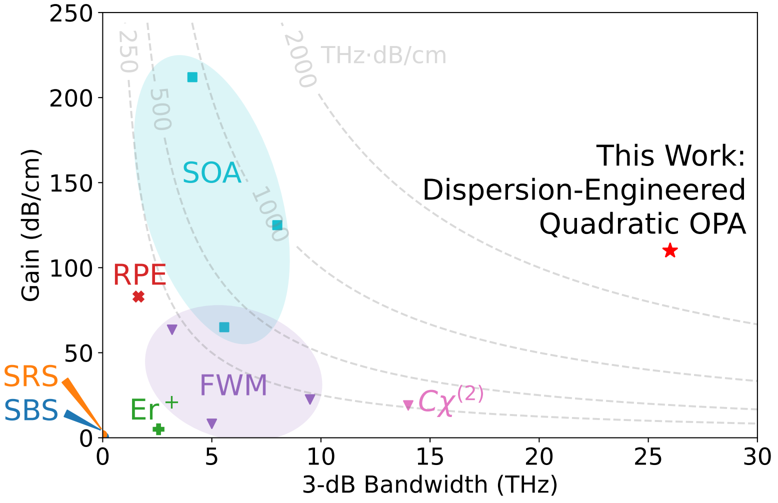

Figure 3.8: **Comparison of gain and bandwidth with other gain mechanisms in integrated photonics.** The assumptions made to generate this comparison are described in the text. RPE: reverse-proton-exchanged PPLN waveguide; SBS: stimulated Brillouin scattering; SRS: stimulated Raman scattering; Er^+: Erbium doped LN waveguide; FWM: four-wave mixing; SOA: semicondutor optical amplifier; $C\chi^{(2)}$: Cascaded three-wave mixing.

the coupling loss by more than 10 dB seems feasible by developing integrated spot converters [45]. Such an improvement can lead to a gain of more than 150 dB/cm putting the on-chip OPA in direct competition with the largest single-mode SOA gains reported. Further enhancement can be achieved by improving the poling duty cycle, depth, and fidelity [46]. Combined with other linear and nonlinear functionalities available on thin-film LN, the presented intense OPA can open unprecedented opportunities in integrated photonics, for instance for quantum information processing, mid-infrared sources, optical computing, femtosecond frequency combs and laser ranging.

References

[1] L. Ledezma, R. Sekine, Q. Guo, R. Nehra, S. Jahani, and A. Marandi, "Intense optical parametric amplification in dispersion-engineered nanophotonic lithium niobate waveguides," *Optica*, vol. 9, no. 3, pp. 303–308, Mar. 2022, ISSN: 2334-2536. DOI: `10.1364/OPTICA.442332`.

[2] B. J. Shastri, A. N. Tait, T. Ferreira de Lima, W. H. P. Pernice, H. Bhaskaran, C. D. Wright, and P. R. Prucnal, "Photonics for artificial intelligence and neuromorphic computing," *Nature Photonics*, vol. 15, no. 2, pp. 102–114, Feb. 2021, ISSN: 1749-4893. DOI: `10.1038/s41566-020-00754-y`.

[3] J. Riemensberger, A. Lukashchuk, M. Karpov, W. Weng, E. Lucas, J. Liu, and T. J. Kippenberg, "Massively parallel coherent laser ranging using a soliton microcomb," *Nature*, vol. 581, no. 7807, pp. 164–170, May 2020, ISSN: 1476-4687. DOI: `10.1038/s41586-020-2239-3`.

[4] Y. Shaked, Y. Michael, R. Z. Vered, L. Bello, M. Rosenbluh, and A. Pe'er, "Lifting the bandwidth limit of optical homodyne measurement with broadband parametric amplification," *Nature Communications*, vol. 9, no. 1, p. 609, Feb. 2018, ISSN: 2041-1723. DOI: `10.1038/s41467-018-03083-5`.

[5] Z. Tong, C. Lundström, P. A. Andrekson, C. J. McKinstrie, M. Karlsson, D. J. Blessing, E. Tipsuwannakul, B. J. Puttnam, H. Toda, and L. Grüner-Nielsen, "Towards ultrasensitive optical links enabled by low-noise phase-sensitive amplifiers," *Nature Photonics*, vol. 5, no. 7, pp. 430–436, Jul. 2011, ISSN: 1749-4885, 1749-4893. DOI: `10.1038/nphoton.2011.79`.

[6] X. Liu, R. M. Osgood, Y. A. Vlasov, and W. M. J. Green, "Mid-infrared optical parametric amplifier using silicon nanophotonic waveguides," *Nature Photonics*, vol. 4, no. 8, pp. 557–560, Aug. 2010, ISSN: 1749-4893. DOI: `10.1038/nphoton.2010.119`.

[7] K. J. A. Ooi, D. K. T. Ng, T. Wang, A. K. L. Chee, S. K. Ng, Q. Wang, L. K. Ang, A. M. Agarwal, L. C. Kimerling, and D. T. H. Tan, "Pushing the limits of CMOS optical parametric amplifiers with USRN:Si 7 N 3 above the two-photon absorption edge," *Nature Communications*, vol. 8, no. 1, p. 13 878, Jan. 2017, ISSN: 2041-1723. DOI: `10.1038/ncomms13878`.

[8] H. Rong, S. Xu, Y.-H. Kuo, V. Sih, O. Cohen, O. Raday, and M. Paniccia, "Low-threshold continuous-wave Raman silicon laser," *Nature*

Photonics, vol. 1, no. 4, pp. 232–237, Apr. 2007, ISSN: 1749-4893. DOI: `10.1038/nphoton.2007.29`.

[9] E. A. Kittlaus, H. Shin, and P. T. Rakich, "Large Brillouin amplification in silicon," *Nature Photonics*, vol. 10, no. 7, pp. 463–467, Jul. 2016, ISSN: 1749-4893. DOI: `10.1038/nphoton.2016.112`.

[10] B. Haq, S. Kumari, K. V. Gasse, J. Zhang, A. Gocalinska, E. Pelucchi, B. Corbett, and G. Roelkens, "Micro-Transfer-Printed III-V-on-Silicon C-Band Semiconductor Optical Amplifiers," *Laser & Photonics Reviews*, vol. 14, no. 7, p. 1 900 364, 2020, ISSN: 1863-8899. DOI: `https://doi.org/10.1002/lpor.201900364`.

[11] M. L. Davenport, S. Skendžić, N. Volet, J. C. Hulme, M. J. R. Heck, and J. E. Bowers, "Heterogeneous Silicon/III–V Semiconductor Optical Amplifiers," *IEEE Journal of Selected Topics in Quantum Electronics*, vol. 22, no. 6, pp. 78–88, Nov. 2016, ISSN: 1558-4542. DOI: `10.1109/JSTQE.2016.2593103`.

[12] Z. Yang, M. Jahanbozorgi, D. Jeong, S. Sun, O. Pfister, H. Lee, and X. Yi, "A squeezed quantum microcomb on a chip," *Nature Communications*, vol. 12, no. 1, p. 4781, Aug. 2021, ISSN: 2041-1723. DOI: `10.1038/s41467-021-25054-z`.

[13] R. Nehra, R. Sekine, L. Ledezma, Q. Guo, R. M. Gray, A. Roy, and A. Marandi, "Few-cycle vacuum squeezing in nanophotonics," *arXiv:2201.06768 [quant-ph]*, Jan. 2022. arXiv: `2201.06768 [quant-ph]`.

[14] M. H. Dunn and M. Ebrahimzadeh, "Parametric generation of tunable light from continuous-wave to femtosecond pulses," *Science*, vol. 286, no. 5444, pp. 1513–1517, Nov. 1999, ISSN: 0036-8075, 1095-9203. DOI: `10.1126/science.286.5444.1513`.

[15] Y.-C. Lin, Y. Nabekawa, and K. Midorikawa, "Optical parametric amplification of sub-cycle shortwave infrared pulses," *Nature Communications*, vol. 11, no. 1, p. 3413, Jul. 2020, ISSN: 2041-1723. DOI: `10.1038/s41467-020-17247-9`.

[16] G. Cerullo and S. De Silvestri, "Ultrafast optical parametric amplifiers," *Review of Scientific Instruments*, vol. 74, no. 1, pp. 1–18, Jan. 2003, ISSN: 0034-6748. DOI: `10.1063/1.1523642`.

[17] S.-W. Huang, G. Cirmi, J. Moses, K.-H. Hong, S. Bhardwaj, J. R. Birge, L.-J. Chen, E. Li, B. J. Eggleton, G. Cerullo, and F. X. Kärtner, "High-energy pulse synthesis with sub-cycle waveform control for strong-field physics," *Nature Photonics*, vol. 5, no. 8, pp. 475–479, Aug. 2011, ISSN: 1749-4893. DOI: `10.1038/nphoton.2011.140`.

[18] E. J. Stanton, J. Chiles, N. Nader, G. Moody, G. Moody, N. Volet, L. Chang, J. E. Bowers, S. W. Nam, and R. P. Mirin, "Efficient second harmonic generation in nanophotonic GaAs-on-insulator waveguides," *Optics Express*, vol. 28, no. 7, pp. 9521–9532, Mar. 2020, ISSN: 1094-4087. DOI: `10.1364/OE.389423`.

[19] D. M. Lukin, C. Dory, M. A. Guidry, K. Y. Yang, S. D. Mishra, R. Trivedi, M. Radulaski, S. Sun, D. Vercruysse, G. H. Ahn, and J. Vučković, "4H-silicon-carbide-on-insulator for integrated quantum and nonlinear photonics," *Nature Photonics*, vol. 14, no. 5, pp. 330–334, May 2020, ISSN: 1749-4893. DOI: `10.1038/s41566-019-0556-6`.

[20] D. J. Wilson, K. Schneider, S. Hönl, M. Anderson, Y. Baumgartner, L. Czornomaz, T. J. Kippenberg, and P. Seidler, "Integrated gallium phosphide nonlinear photonics," *Nature Photonics*, vol. 14, no. 1, pp. 57–62, Jan. 2020, ISSN: 1749-4893. DOI: `10.1038/s41566-019-0537-9`.

[21] A. W. Bruch, X. Liu, Z. Gong, J. B. Surya, M. Li, C.-L. Zou, and H. X. Tang, "Pockels soliton microcomb," *Nature Photonics*, vol. 15, no. 1, pp. 21–27, Jan. 2021, ISSN: 1749-4893. DOI: `10.1038/s41566-020-00704-8`.

[22] C. Wang, C. Langrock, A. Marandi, M. Jankowski, M. Zhang, B. Desiatov, M. M. Fejer, and M. Lončar, "Ultrahigh-efficiency wavelength conversion in nanophotonic periodically poled lithium niobate waveguides," *Optica*, vol. 5, no. 11, pp. 1438–1441, Nov. 2018, ISSN: 2334-2536. DOI: `10.1364/OPTICA.5.001438`.

[23] M. Jankowski, C. Langrock, B. Desiatov, A. Marandi, C. Wang, M. Zhang, C. R. Phillips, M. Lončar, and M. M. Fejer, "Ultrabroadband nonlinear optics in nanophotonic periodically poled lithium niobate waveguides," *Optica*, vol. 7, no. 1, pp. 40–46, Jan. 2020, ISSN: 2334-2536. DOI: `10.1364/OPTICA.7.000040`.

[24] M. Zhang, B. Buscaino, C. Wang, A. Shams-Ansari, C. Reimer, R. Zhu, J. M. Kahn, and M. Lončar, "Broadband electro-optic frequency comb generation in a lithium niobate microring resonator," *Nature*, vol. 568, no. 7752, pp. 373–377, Apr. 2019, ISSN: 1476-4687. DOI: `10.1038/s41586-019-1008-7`.

[25] C. Wang, M. Zhang, X. Chen, M. Bertrand, A. Shams-Ansari, S. Chandrasekhar, P. Winzer, and M. Lončar, "Integrated lithium niobate electro-optic modulators operating at CMOS-compatible voltages," *Nature*, vol. 562, no. 7725, p. 101, Oct. 2018, ISSN: 1476-4687. DOI: `10.1038/s41586-018-0551-y`.

[26] T. P. McKenna, H. S. Stokowski, V. Ansari, J. Mishra, M. Jankowski, C. J. Sarabalis, J. F. Herrmann, C. Langrock, M. M. Fejer, and A. H. Safavi-Naeini, "Ultra-low-power second-order nonlinear optics on a chip," *arXiv:2102.05617 [physics, physics:quant-ph]*, Feb. 2021.

[27] J. Lu, A. A. Sayem, Z. Gong, J. B. Surya, C.-L. Zou, and H. X. Tang, "Ultralow-threshold thin-film lithium niobate optical parametric oscillator," *Optica*, vol. 8, no. 4, pp. 539–544, Apr. 2021, ISSN: 2334-2536. DOI: `10.1364/OPTICA.418984`.

[28] J. Zhao, C. Ma, M. Rüsing, and S. Mookherjea, "High quality entangled photon pair generation in periodically poled thin-film lithium niobate waveguides," *Physical Review Letters*, vol. 124, no. 16, p. 163 603, Apr. 2020. DOI: `10.1103/PhysRevLett.124.163603`.

[29] R. Luo, Y. He, H. Liang, M. Li, and Q. Lin, "Highly tunable efficient second-harmonic generation in a lithium niobate nanophotonic waveguide," *Optica*, vol. 5, no. 8, pp. 1006–1011, Aug. 2018, ISSN: 2334-2536. DOI: `10.1364/OPTICA.5.001006`.

[30] A. Marandi, K. A. Ingold, M. Jankowski, and R. L. Byer, "Cascaded half-harmonic generation of femtosecond frequency combs in the mid-infrared," *Optica*, vol. 3, no. 3, pp. 324–327, Mar. 2016, ISSN: 2334-2536. DOI: `10.1364/OPTICA.3.000324`.

[31] W. H. Louisell, A. Yariv, and A. E. Siegman, "Quantum fluctuations and noise in parametric processes. I.," *Physical Review*, vol. 124, no. 6, pp. 1646–1654, Dec. 1961. DOI: `10.1103/PhysRev.124.1646`.

[32] M. Jankowski, M. Jankowski, M. Jankowski, N. Jornod, N. Jornod, C. Langrock, B. Desiatov, A. Marandi, M. Lončar, and M. M. Fejer, "Quasi-static optical parametric amplification," *Optica*, vol. 9, no. 3, pp. 273–279, Mar. 2022, ISSN: 2334-2536. DOI: `10.1364/OPTICA.442550`.

[33] D. A. Kleinman, "Theory of Optical Parametric Noise," *Physical Review*, vol. 174, no. 3, pp. 1027–1041, Oct. 1968. DOI: `10.1103/PhysRev.174.1027`.

[34] G. Arisholm, "Quantum noise initiation and macroscopic fluctuations in optical parametric oscillators," *Journal of the Optical Society of America B*, vol. 16, no. 1, p. 117, Jan. 1999, ISSN: 0740-3224, 1520-8540. DOI: `10.1364/JOSAB.16.000117`.

[35] Z. Y. Ou, S. F. Pereira, H. J. Kimble, and K. C. Peng, "Realization of the Einstein-Podolsky-Rosen paradox for continuous variables," *Physical Review Letters*, vol. 68, no. 25, pp. 3663–3666, Jun. 1992. DOI: `10.1103/PhysRevLett.68.3663`.

[36] J. Hansryd, P. A. Andrekson, M. Westlund, Jie Li, and P. Hedekvist, "Fiber-based optical parametric amplifiers and their applications," *IEEE Journal of Selected Topics in Quantum Electronics*, vol. 8, no. 3, pp. 506–520, May 2002, ISSN: 1558-4542. DOI: `10.1109/JSTQE.2002.1016354`.

[37] X. Xie, A. M. Schober, C. Langrock, R. V. Roussev, J. R. Kurz, and M. M. Fejer, “Picojoule threshold, picosecond optical parametric generation in reverse proton-exchanged lithium niobate waveguides,” *Journal of the Optical Society of America B*, vol. 21, no. 7, pp. 1397–1402, Jul. 2004, ISSN: 1520-8540. DOI: `10.1364/JOSAB.21.001397`.

[38] K. V. Gasse, R. Wang, and G. Roelkens, “27 dB gain III–V-on-silicon semiconductor optical amplifier with > 17 dBm output power,” *Optics Express*, vol. 27, no. 1, pp. 293–302, Jan. 2019, ISSN: 1094-4087. DOI: `10.1364/OE.27.000293`.

[39] N. Volet, A. Spott, E. J. Stanton, M. L. Davenport, L. Chang, J. D. Peters, T. C. Briles, I. Vurgaftman, J. R. Meyer, and J. E. Bowers, “Semiconductor optical amplifiers at 2.0-µm wavelength on silicon,” *Laser & Photonics Reviews*, vol. 11, no. 2, p. 1 600 165, 2017, ISSN: 1863-8899. DOI: `https://doi.org/10.1002/lpor.201600165`.

[40] B. Kuyken, X. Liu, G. Roelkens, R. Baets, J. Richard M. Osgood, and W. M. J. Green, “50 dB parametric on-chip gain in silicon photonic wires,” *Optics Letters*, vol. 36, no. 22, pp. 4401–4403, Nov. 2011, ISSN: 1539-4794. DOI: `10.1364/OL.36.004401`.

[41] M. A. Foster, A. C. Turner, J. E. Sharping, B. S. Schmidt, M. Lipson, and A. L. Gaeta, “Broad-band optical parametric gain on a silicon photonic chip,” *Nature*, vol. 441, no. 7096, pp. 960–963, Jun. 2006, ISSN: 1476-4687. DOI: `10.1038/nature04932`.

[42] V. Sih, S. Xu, Y.-H. Kuo, H. Rong, M. Paniccia, O. Cohen, and O. Raday, “Raman amplification of 40 Gb/s data in low-loss silicon waveguides,” *Optics Express*, vol. 15, no. 2, pp. 357–362, Jan. 2007, ISSN: 1094-4087. DOI: `10.1364/OE.15.000357`.

[43] J. Zhou, Y. Liang, Z. Liu, W. Chu, H. Zhang, D. Yin, Z. Fang, R. Wu, J. Zhang, W. Chen, Z. Wang, Y. Zhou, M. Wang, and Y. Cheng, “On-chip integrated waveguide amplifiers on Erbium-doped thin film lithium niobate on insulator,” *arXiv:2101.00783 [physics]*, Jan. 2021.

[44] Y. M. Sua, J.-Y. Chen, and Y.-P. Huang, “Ultra-wideband and high-gain parametric amplification in telecom wavelengths with an optimally mode-matched PPLN waveguide,” *Optics Letters*, vol. 43, no. 12, pp. 2965–2968, Jun. 2018, Publisher: Optical Society of America, ISSN: 1539-4794. DOI: `10.1364/OL.43.002965`.

[45] N. Yao, N. Yao, J. Zhou, J. Zhou, J. Zhou, R. Gao, R. Gao, J. Lin, J. Lin, J. Lin, M. Wang, M. Wang, Y. Cheng, Y. Cheng, Y. Cheng, Y. Cheng, Y. Cheng, Y. Cheng, Y. Cheng, Y. Cheng, Y. Cheng, W. Fang, W. Fang, and L. Tong, “Efficient light coupling between an ultra-low loss lithium niobate waveguide and an adiabatically tapered single mode optical fiber,” *Optics*

Express, vol. 28, no. 8, pp. 12 416–12 423, Apr. 2020, ISSN: 1094-4087. DOI: `10.1364/OE.391228`.

[46] M. Rüsing, J. Zhao, and S. Mookherjea, "Second harmonic microscopy of poled x-cut thin film lithium niobate: Understanding the contrast mechanism," *Journal of Applied Physics*, vol. 126, no. 11, p. 114 105, Sep. 2019, ISSN: 0021-8979. DOI: `10.1063/1.5113727`.

Chapter 4

DOUBLY-RESONANT OPOS IN NANOPHOTONIC LITHIUM NIOBATE

In this chapter I describe the design and features common to the doubly-resonant oscillators demonstrated in the next few chapters.

4.1 OPO description and conventions

We will use the standard naming convention of pump, signal, and idler for the three waves at frequencies $\{\omega_p,\ \omega_s,\ \omega_i = \omega_p - \omega_s\}$, and will use subscripts $\{p, s, i\}$ accordingly. We consider an OPO like that shown in Fig. 4.1 with a parametric gain section of length L_g and a total resonator length L. The waveguide losses per unit length are given by coefficients α_s and α_i at signal and idler wavelengths. The loss factors for the fields are $\exp\left(-\alpha_{s,i}L\right)$ while for the corresponding powers are $\exp\left(-2\alpha_{s,i}L\right)$. The input and output couplers have power coupling coefficients R_1 and R_2, and power transmission coefficients $T_1 = 1 - R_1$ and $T_2 = 1 - R_2$. We will use an additional subscript to refer to the signal/idler when necessary, e.g., the output coupling coefficient at the signal wavelength is $R_{2,s}$. We will often write the coupling coefficients in exponential notation in order to lump them with waveguide losses, $R_j = \exp\left[-2\delta_j L\right]$. The total resonator loss factor for the signal field is then

$$\sqrt{R_{1,s}R_{2,s}}e^{-\alpha_s L} = e^{-(\delta_{1,s}+\delta_{2,s}+\alpha_s)L} = e^{-\alpha_s' L}, \tag{4.1}$$

where $\alpha_s' \equiv \delta_{1,s} + \delta_{2,s} + \alpha_s$, is the total signal loss per round-trip length. A similar expression holds for the idler field.

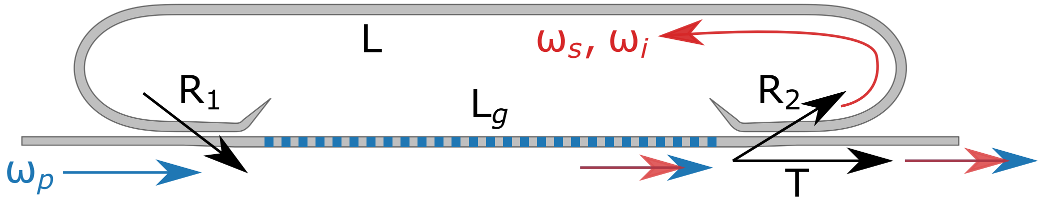

Figure 4.1: **Doubly-resonant OPO schematic.** The couplers are described by power coupling factors R and transmission factor T. The length of the poled waveguide providing the parametric gain is L_g, while the round-trip resonator length is L.

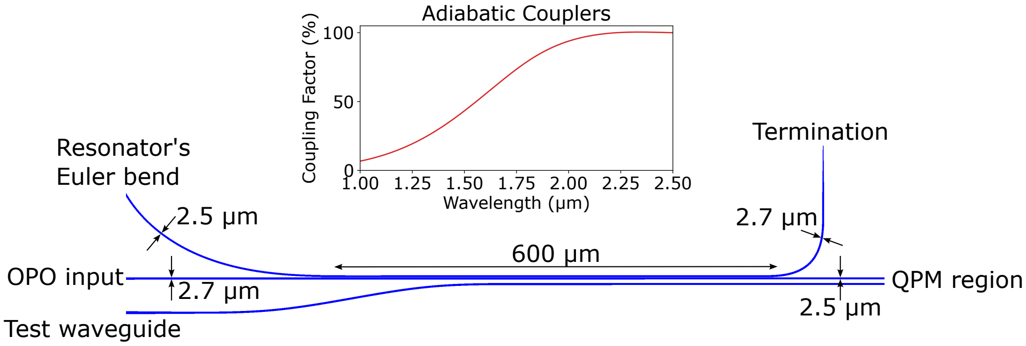

Figure 4.2: **Adiabatic coupler design.** The couplers are designed so that signal and idler coupled strongly to the OPO resonator while the ~1045 nm pump does not experience feedback. The dimensions corresponds to the OPOs demonstrated in the following chapters.

4.2 Adiabatic coupler design

We choose a doubly-tapered adiabatic evanescent coupler design in which one waveguide is linearly tapered from a width of w_1 to w_2, while the adjacent waveguide is linearly tapered from w_2 to w_1. The gap between waveguides is kept constant and along with the length L it determines the coupling coefficient, which can be estimated from [1]

$$R_{1,2} = 1 - \exp\left[-\pi g^2 \beta L/\Delta n\right], \tag{4.2}$$

where β is the propagation constant for an isolated waveguide of width $(w_1 + w_2)/2$, Δn is the refractive index different between isolated waveguides of width w_1 and w_2, and g is the coupling strength that equals half of the refractive index difference between the even and odd modes of the combined system of waveguides with width $(w_1 + w_2)/2$. This design produces a coupling coefficient that increases monotonically with wavelength, as shown in Fig. 4.2.

4.3 Threshold

The set of three coupled-wave equations for the mode amplitudes are

$$\frac{\partial A_s}{\partial z} = -i\kappa_s A_i^* A_p e^{-i\Delta\beta z}, \quad \frac{\partial A_i}{\partial z} = -i\kappa_i A_s^* A_p e^{-i\Delta\beta z}, \quad \frac{\partial A_p}{\partial z} = -i\kappa_p A_s A_i e^{i\Delta\beta z},$$

where $\Delta\beta = \beta_p - \beta_s - \beta_i - k_g$ is the phase mismatch, and $k_g = 2\pi/\Lambda_{\text{QPM}}$ is the momentum contribution from a quasi-phase matching grating with period Λ_{QPM}. Assuming there is no pump depletion, the signal and idler equations can be integrated yielding [2]:

$$\begin{bmatrix} A_s(L_g) \\ A_i^*(L_g) \end{bmatrix} = \begin{bmatrix} g_{ss} & g_{si} \\ g_{is} & g_{ii} \end{bmatrix} \begin{bmatrix} A_s(0) \\ A_i^*(0) \end{bmatrix}, \tag{4.3}$$

where $g_{ss} = g_{ii} = \cosh(\Gamma L_g)$, $g_{si} = i\sqrt{\kappa_s/\kappa_i}\sinh(\Gamma L_g)$, $g_{is} = -i\sqrt{\kappa_i/\kappa_s}\sinh(\Gamma L_g)$, and $\Gamma^2 = \kappa_s\kappa_i|A_p|^2 = \kappa_s\kappa_i P_p$. In steady state, the signal and idler fields must replicate themselves after each round-trip. So, the total transfer matrix

$$M = \begin{bmatrix} g_{ss} & g_{si} \\ g_{is} & g_{ss} \end{bmatrix} \begin{bmatrix} e^{-\alpha_s' L} & 0 \\ 0 & e^{-\alpha_i' L} \end{bmatrix} = \begin{bmatrix} g_{ss}e^{-\alpha_s' L} & g_{si}e^{-\alpha_i' L} \\ g_{is}e^{-\alpha_s' L} & g_{ss}e^{-\alpha_i' L} \end{bmatrix} \tag{4.4}$$

must have a unit eigenvalue [3]. This condition leads to the characteristic equation

$$\left(g_{ss}e^{-\alpha_s' L} - 1\right)\left(g_{ss}e^{-\alpha_i' L} - 1\right) - g_{si}g_{is}e^{-(\alpha_i'+\alpha_s')L} = 0, \tag{4.5}$$

that can be simplified noticing that $g_{ss}^2 - g_{si}g_{is} = 1$, yielding the threshold condition

$$g_{ss} = \cosh(\Gamma L_g) = \frac{1 + e^{-(\alpha_i'+\alpha_s')L}}{e^{-\alpha_s' L} + e^{-\alpha_i' L}} = \frac{\cosh\left[(\alpha_s' + \alpha_i')L/2\right]}{\cosh\left[(\alpha_s' - \alpha_i')L/2\right]}. \tag{4.6}$$

When signal and idler total losses are similar ($\alpha_s' \approx \alpha_i'$), this reduces to $\Gamma L_g = \alpha_s' L$, indicating that the parametric gain must match the total round-trip loss, as expected. Figure 4.3 shows example calculations of the normalized nonlinear efficiency ($\kappa_i\kappa_s = \Gamma^2/P_p$), total resonator loss factors, and threshold pump power for our OPO.

4.4 Escape efficiency

The efficiency of an OPO (η) can be written as the product of two efficiencies, $\eta = \eta_0\eta_{\text{escape}}$. The internal efficiency (η_0) measures how effectively pump photons are converted into signal and idler photons, while the escape efficiency (η_{escape}) measures the fraction of the generated signal and idler photons available at the output of the OPO.

The difference between the pump power at the beginning and end of the gain section is $\Delta P_p = P_p(0) - P_p(L_g)$. If we assume that this pump loss is due only to parametric down-conversion to signal and idler waves, then the signal and idler power increase by ΔP_s and ΔP_i, such that $\Delta P_p = \Delta P_s + \Delta P_i$. Additionally, the Manley-Rowe relations gives us

$$\frac{\Delta P_p}{\omega_p} = \frac{\Delta P_s}{\omega_s} = \frac{\Delta P_i}{\omega_i}, \tag{4.7}$$

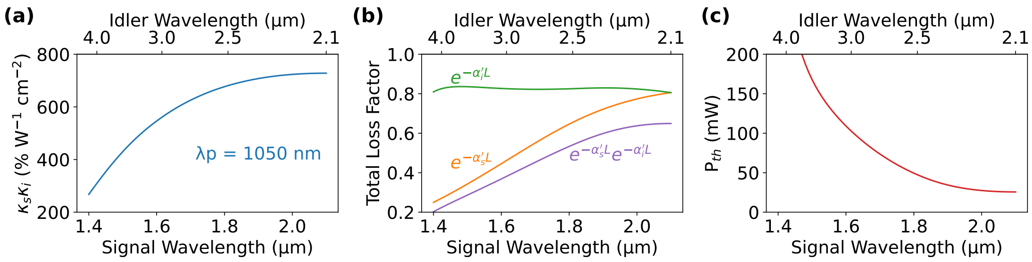

Figure 4.3: **Threshold of doubly-resonant OPOs.** **a,** Simulated normalized nonlinear efficiency ($\kappa_s\kappa_i$) for our OPOs. The reduction in efficiency far from degeneracy is mostly due to a decreasing overlap integral (Θ) and a correspondingly large effective interaction area (A_{eff}). **b,** Calculated total loss factors of the OPO resonator, assuming a flat propagation loss of 1.4 dB per round-trip. Most of the loss far from degeneracy comes from the low coupling at signal wavelengths below ~1.7 μm. **c,** Calculated OPO threshold as a function of signal and idler wavelengths. High threshold far from degeneracy is a consequence of gain and loss factors depicted in **a** and **b**.

where the lack of negative signs follows from our definition of ΔP_p as a power loss, and ΔP_s and ΔP_i as power gains. The internal efficiency is $\eta_0 = \Delta P_p / P_p(0)$.

Let us focus now on the signal power. At the beginning the parametric gain section the signal power is $P_s(0)$ and at the end it is $P_s(L_g) = P_s(0) + \Delta P_s = G_s P_s(0)$, where G_s is the parametric gain experienced by the signal. So, we can express the signal at the output of the parametric gain section as $P_s(L_g) = \Delta P_s G_s/(G_s - 1)$. The signal power at the output of the OPO is the fraction of $P_s(L_g)$ transmitted by the output coupler with transmittance T_s, this is, $P_s^{\text{out}} = T_s P_s(L_g) = \Delta P_s T_s G_s/(G_s - 1)$. Including a similar expression for the idler and adding them together we get

$$
\begin{aligned}
P_{\text{total}}^{\text{out}} = P_s^{\text{out}} + P_i^{\text{out}} &= \frac{T_s G_s}{G_s - 1}\Delta P_s + \frac{T_i G_i}{G_i - 1}\Delta P_i && (4.8)\\
&= \Delta P_p \left(\frac{\omega_s}{\omega_p} \frac{T_s G_s}{G_s - 1} + \frac{\omega_i}{\omega_p} \frac{T_i G_i}{G_i - 1} \right), && (4.9)
\end{aligned}
$$

where we have used (4.7). The total efficiency is then

$$
\eta = \frac{P_{\text{total}}^{\text{out}}}{P_p(0)} = \eta_0 \left(\frac{\omega_s}{\omega_p} \frac{T_s G_s}{G_s - 1} + \frac{\omega_i}{\omega_p} \frac{T_i G_i}{G_i - 1} \right), \tag{4.10}
$$

so the term in parenthesis is the escape efficiency

$$
\eta_{\text{escape}} = \frac{\omega_s}{\omega_p} \frac{T_s G_s}{G_s - 1} + \frac{\omega_i}{\omega_p} \frac{T_i G_i}{G_i - 1} = \frac{\omega_s}{\omega_p} \frac{T_s}{1 - G_s^{-1}} + \frac{\omega_i}{\omega_p} \frac{T_i}{1 - G_i^{-1}}. \tag{4.11}
$$

It is useful to connect this expression with the losses in the resonator. In steady state, the gain experienced by the signal exactly balances the round-trip loss, so $G_s^{-1} = \exp\left(-2\alpha'_s L\right)$. Substituting in (4.11) and including a similar expression for the idler term, we get:

$$\eta_{\text{escape}} = \frac{\omega_s}{\omega_p}\frac{T_s}{1 - e^{-2\alpha'_s L}} + \frac{\omega_i}{\omega_p}\frac{T_i}{1 - e^{-2\alpha'_i L}}. \tag{4.12}$$

Note that when all the losses and coupling coefficients are similar at signal and idler wavelengths, e.g. near degeneracy, then we can remove the signal/idler subscripts and, since $\omega_s + \omega_i = \omega_p$, this expression simplifies to:

$$\eta_{\text{escape}}\Big|_{\omega_s \approx \omega_i} = \frac{T_2}{1 - e^{-2\alpha' L}} = \frac{1 - R_2}{1 - R_1 R_2 e^{-2\alpha L}}, \tag{4.13}$$

where we can see that the escape efficiency tends to unity when $R_2 \ll R_1 e^{-2\alpha L}$, i.e., when the output coupling dominates the total resonator losses.

4.5 Conversion efficiency

We will now find an expression for the OPO output power under low-loss conditions. In this case, the gain per round-trip in steady state is small, so we will assume that the signal and idler modes do not vary significantly over the parametric gain section. This is, we will assume that $\Delta P_s / P_s(0)$ is small, and similarly for the idler. Note that we are not assuming anything about the size of $P_s(0)$, so the intracavity power can be large and lead to large pump depletion and high efficiency.

We start by integrating the pump field along the parametric gain section assuming perfect phase matching, constant signal and idler fields, and a phase-relationship between the fields that maximizes parametric gain, to obtain

$$A_p(L_g) = A_p(0) - \kappa_3 A_s A_i L_g. \tag{4.14}$$

Squaring this expression, and recalling that $\Delta P_p \equiv P_p(0) - P_p(L_g)$, we get

$$\kappa_3^2 P_s P_i L_g^2 = 2\kappa_3 L_g A_p(0) A_s A_i - \Delta P_p. \tag{4.15}$$

Now we can use (4.7) to introduce ΔP_s; also recall that ΔP_s is proportional to P_s, i.e., $\Delta P_s = a_s P_s$, where $a_s = 1 - 1/Gs = 1 - e^{-2\alpha'_s L} \approx 2\alpha'_s L$ (where α'_s represents the total resonator losses, including couplers). Substituting in (4.15) we get,

$$\kappa_3^2 P_s P_i L_g^2, = 2\kappa_3 L_g A_p(0) A_s A_i - \frac{\omega_p}{\omega_s} a_s P_s \tag{4.16}$$

and dividing by $P_s = A_s^2$,

$$\kappa_3^2 P_i L_g^2 = 2\kappa_3 L_g A_p(0)\frac{A_i}{A_s} - \frac{\omega_p}{\omega_s}a_s. \tag{4.17}$$

Now, we can use (4.7) yet again to relate signal and idler. We have $\Delta P_i = (\omega_i/\omega_s)\Delta P_s$, but just like we did for the signal, the idler increment is proportional to its power, $\Delta P_i = a_i P_i$, so combining these we get $P_i = (\omega_i a_s/\omega_s a_i)P_s$, and for the amplitudes $A_i/A_s = \sqrt{\omega_i a_s/\omega_s a_i}$. Substituting these in (4.17) we get

$$\kappa_3^2\frac{\omega_i a_s}{\omega_s a_i}P_s L_g^2 = 2L_g\kappa_3\sqrt{\frac{\omega_i a_s}{\omega_s a_i}}A_p(0) - \frac{\omega_p}{\omega_s}a_s. \tag{4.18}$$

So the signal power inside the resonator becomes

$$P_s = \frac{2}{\kappa_3 L_g}\sqrt{\frac{\omega_s a_i}{\omega_i a_s}}\left[A_p(0) - \frac{\omega_p}{2\kappa_3 L_g}\sqrt{\frac{a_i a_s}{\omega_i\omega_s}}\right]. \tag{4.19}$$

We can simplify this expression by using the relationship between the nonlinear coupling coefficients and the frequencies, for instance, $\kappa_3^2\omega_i\omega_s/\omega_p^2 = \kappa_1\kappa_2$, so

$$P_s = \frac{4\omega_s}{\omega_p a_s}\sqrt{\frac{a_s a_i}{4L_g^2\kappa_1\kappa_2}}\left[A_p(0) - \sqrt{\frac{a_i a_s}{4L_g^2\kappa_1\kappa_2}}\right]. \tag{4.20}$$

Finally, we note that for a non-zero signal power the pump amplitude must exceed the second term inside the bracket, so this must be the threshold amplitude:

$$A_{\text{th}} = \sqrt{\frac{a_i a_s}{4L_g^2\kappa_1\kappa_2}} \longrightarrow P_{\text{th}} = \frac{a_i a_s}{4L_g^2\kappa_1\kappa_2}, \tag{4.21}$$

which under the low-loss approximations for $a_s \approx 2\alpha_s' L$, and $a_i \approx 2\alpha_i' L$ becomes

$$P_{\text{th}} = \frac{\alpha_s'\alpha_i' L^2}{\kappa_1\kappa_2 L_g^2}. \tag{4.22}$$

This expression matches our previous threshold condition (4.6) under the appropriate low-loss approximation:

$$\cosh\left(\sqrt{\kappa_1\kappa_2 P_{\text{th}}}L_g\right) = \frac{1 + e^{-\alpha_s' L}e^{-\alpha_i' L}}{e^{-\alpha_s' L} + e^{-\alpha_i' L}} \longrightarrow \frac{\kappa_1\kappa_2 P_{\text{th}} L_g^2}{2} \approx \frac{\alpha_s'\alpha_i' L^2}{2 + \alpha_s' L + \alpha_i' L}. \tag{4.23}$$

Going back to the signal intracavity power calculation, let us substitute (4.21) into (4.20)

$$a_s P_s = 4\frac{\omega_s}{\omega_p}\sqrt{P_{\text{th}}}\left(\sqrt{P_p} - \sqrt{P_{\text{th}}}\right) \longrightarrow \frac{\Delta P_s}{P_p} = \frac{\omega_s}{\omega_p}\frac{4}{N}\left(\sqrt{N} - 1\right), \tag{4.24}$$

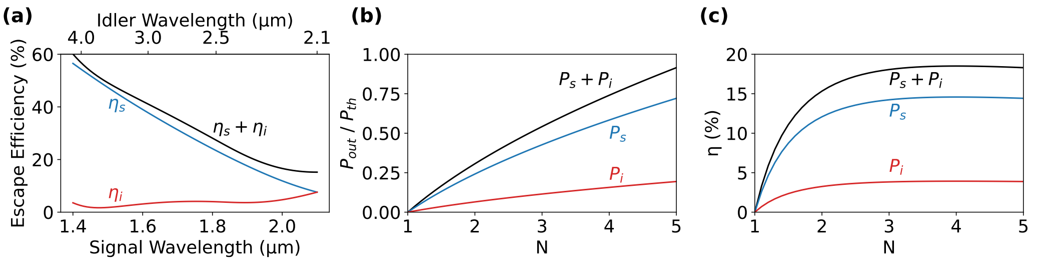

Figure 4.4: **Efficiency and output power of doubly-resonant OPOs. a,** Calculated escape efficiency for signal, idler, and total. The idler escape efficiency is poor due to the adiabatic design of our couplers. **b,** Calculated output power relative to threshold as a function of number of times above threshold (N). **c,** Calculated output efficiency as a function of number of times above threshold (N). In both, **b** and **c**, a signal wavelength of 1950 nm was assumed.

where N is the number of times above threshold ($N \equiv P_p/P_{\text{th}}$).

Finally, combining (4.24) and a similar expression for the idler, the internal efficiency becomes

$$\eta_0 = \frac{\Delta P_p}{P_p} = \frac{\Delta P_s + \Delta P_i}{P_p} = \left(\frac{\omega_s}{\omega_p} + \frac{\omega_i}{\omega_p}\right)\frac{4}{N}\left(\sqrt{N} - 1\right) = \frac{4}{N}\left(\sqrt{N} - 1\right). \tag{4.25}$$

4.6 Total efficiency and output power

Combining the results from the previous two sections we get:

$$\eta = \frac{P_s^{\text{out}} + P_i^{\text{out}}}{P_p} = \frac{4}{N}\left(\sqrt{N} - 1\right)\eta_{\text{escape}} \tag{4.26}$$

$$= \frac{4}{N}\left(\sqrt{N} - 1\right)\left[\frac{\omega_s}{\omega_p}\frac{T_s}{1 - e^{-2\alpha_s' L}} + \frac{\omega_i}{\omega_p}\frac{T_i}{1 - e^{-2\alpha_i' L}}\right]. \tag{4.27}$$

And corresponding signal and output powers given by

$$P_s^{\text{out}} = 4P_{\text{th}}\left(\sqrt{N} - 1\right)\left[\frac{\omega_s}{\omega_p}\frac{T_s}{1 - e^{-2\alpha_s' L}}\right], \tag{4.28}$$

$$P_i^{\text{out}} = 4P_{\text{th}}\left(\sqrt{N} - 1\right)\left[\frac{\omega_i}{\omega_p}\frac{T_i}{1 - e^{-2\alpha_i' L}}\right]. \tag{4.29}$$

Examples of internal efficiency, output power, and output efficiency calculated for our OPO are shown in Fig. 4.4.

4.7 OPO tuning curves and dispersion engineering

The conditions of energy conservation ($\omega_s + \omega_i = \omega_p$) and momentum conservation ($\Delta\beta = 0$) describe a curve in $\{\omega_p,\ \omega_{s,i}\}$ space, known as the OPO tuning curve.

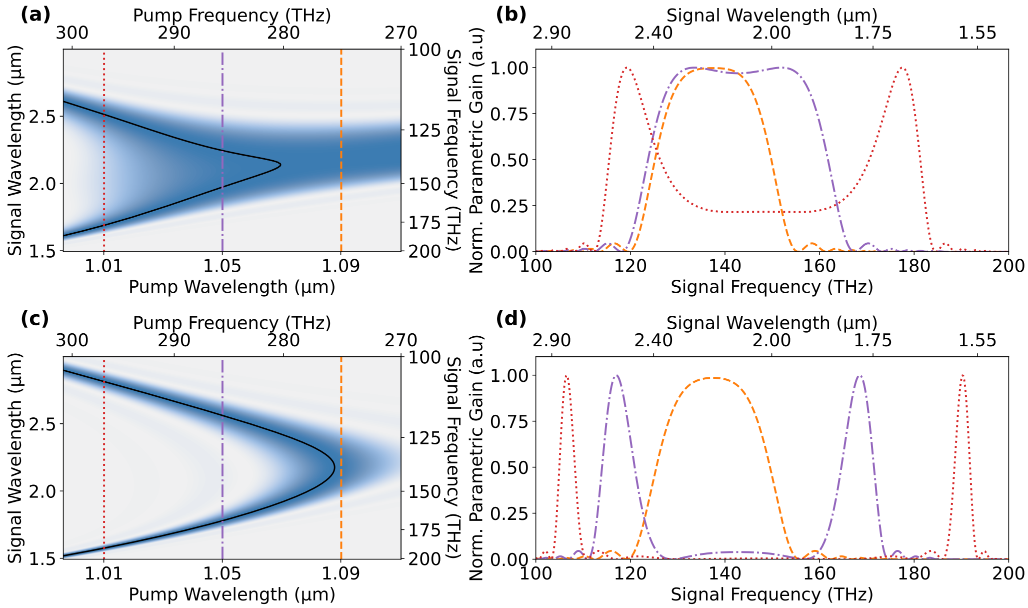

Figure 4.5: **Tuning curves of doubly-resonant OPOs.** Two examples of OPOs with different geometries, showing the effect of dispersion engineering on the tuning curves. **(a),(b)** correspond to an OPO that could be pumped with femtosecond pulses for frequency comb generation in the mid-infrared. **(c),(d)** correspond to the OPOs described in the main text, exhibiting simple tuning characteristics. **(b),(d)** depict parametric gain as a function of signal (and idler) frequency for fixed pump wavelengths indicated by the vertical lines in **(a),(c)**.

This curve can be modified by changing the waveguide dispersion, since

$$\Delta\beta = \beta_p - \beta_s - \beta_i - k_g = \frac{\omega_p n_p}{c} - \frac{\omega_s n_s}{c} - \frac{\omega_i n_i}{c} - k_g, \tag{4.30}$$

and the effective indexes are functions of the waveguide geometry. The tuning slope for the signal can be then calculated as

$$\frac{\partial\omega_s}{\partial\omega_p} = \frac{1/v_i - 1/v_p}{1/v_i - 1/v_p} = \frac{\mathrm{GVM}_{i,p}}{\mathrm{GVM}_{i,s}} = 1 - \frac{\partial\omega_i}{\partial\omega_p}, \tag{4.31}$$

where v_p, v_s, and v_i are the group velocities of the pump, signal, and idler.

Figure 4.5 shows two drastically different examples of tuning curves for two waveguide geometries. The first example shows a design that can support wideband pump pulses near 1 μm. This is the kind of dispersion that we used for the ultrafast parametric amplifier of Chapter 3. The second example shows the tuning curve for the waveguides used in the OPOs of the next few chapters. A smaller gain-bandwidth at degeneracy produces a smoother tuning curve and can potentially enable single-mode tuning.

References

[1] X. Guo, C.-l. Zou, C. Schuck, H. Jung, R. Cheng, and H. X. Tang, "Parametric down-conversion photon-pair source on a nanophotonic chip," *Light: Science & Applications*, vol. 6, no. 5, e16249–e16249, May 2017, ISSN: 2047-7538. DOI: `10.1038/lsa.2016.249`.

[2] R. L. Byer, *Quantum Electronics. 1,B: Nonlinear Optics: Pt. B*. New York: Acad. Press, 1975, ISBN: 978-0-12-574041-8.

[3] A. Yariv, *Quantum Electronics*, 3rd ed. New York: Wiley, 1989, ISBN: 978-0-471-60997-1.

Chapter 5

WIDELY TUNABLE QUASI-CW OPTICAL PARAMETRIC OSCILLATORS

Widely-tunable coherent sources are vital for applications ranging from multi-channel optical communications [2] to lidar [3]. Wide tunability in the mid-infrared spectral range is especially desirable due to the rich molecular responses at wavelengths longer than 2 μm [4]. While it is possible to generate light at these wavelengths with semiconductor lasers [5], the tuning ranges are typically narrow due to limited bandwidth of semiconductor gain [6]–[9]. Alternatively, optical parametric oscillators (OPOs) based on quadratic nonlinearity have been a prominent example of sources with flexible and broad tuning ranges which have commonly been realized using nonlinear crystals in bulky table-top setups [10].

Previous efforts towards OPO miniaturization include using lithium niobate diffused waveguides with fiber feedback loops [11], semiconductor waveguides with Bragg mirrors deposited on the chip end-facets [12], and lithium niobate whispering-gallery microresonators [13]. However, implementation of OPOs in nanophotonics with sub-wavelength modal confinement and low propagation losses is highly desirable because of opportunities for dense integration with other on-chip components, strong nonlinear interactions, and dispersion engineering [14].

Over the past decade, nanophotonic OPO were demonstrated in the near-infrared and visible ranges using materials with cubic ($\chi^{(3)}$) and quadratic ($\chi^{(2)}$) nonlinearities [15]–[20]. However, the main advantages of table-top OPOs, namely wide tunability and mid-infrared coverage, have not yet accessed in nanophotonics. A noteworthy roadblock for this is the typical use of simple pump-resonant configurations in which all the interacting optical fields resonate simultaneously in a single resonator. This leads to ultra-low OPO thresholds at the expense of an over-constrained wavelength tunability. In contrast, OPOs with singly- or doubly-resonant configurations (i.e. with non-resonant pump) offer wide tunability and frequency stability [10].

This chapter is adapted from L. Ledezma, A. Roy, L. Costa, *et al.*, "Widely-tunable optical parametric oscillator in lithium niobate nanophotonics," *arXiv:2203.11482 [physics]*, Mar. 2022. arXiv: `2203.11482 [physics]`.

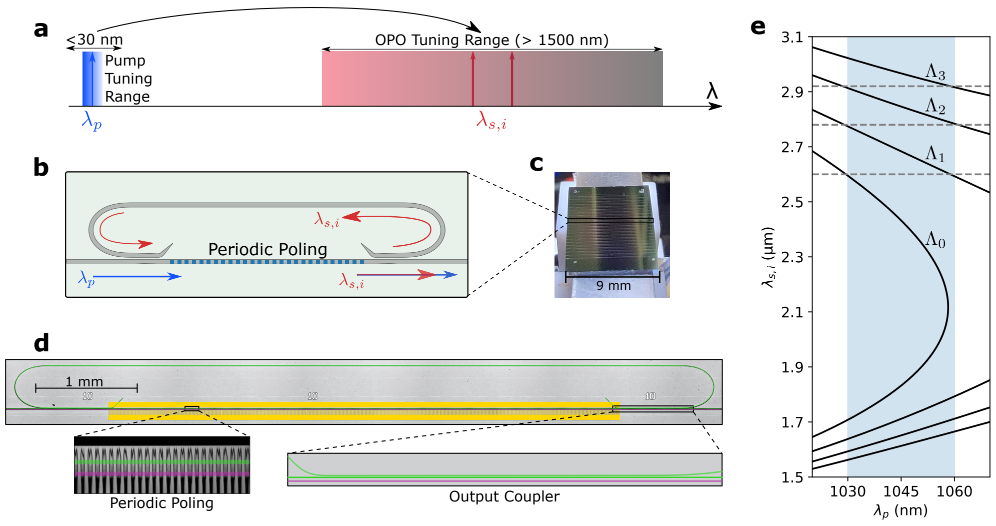

Figure 5.1: **Ultra-widely tunable optical parametric oscillators in nanophotonics. a**, A narrowly tunable (<30 nm) pump around 1 um leads to an OPO signal and idler tuning range exceeding 1500 nm. **b**, Schematic of the doubly-resonant parametric oscillator with a frequency-selective resonator that provides feedback only to the signal and idler while enabling continuous tuning of the pump. **c**, Image of the chip highlighting the area occupied by a single OPO. **d**, False-color optical microscope image of the OPO (green) and a straight waveguide (purple; used for calibration and phase-matching verification). Insets show a two-photon microscope image of the periodic poling and a close-up of the adiabatic output coupler. **e**, Example of OPO tuning curves for four different poling periods $\Lambda_0 - \Lambda_3$. The dashed vertical lines and the blue stripe are to guide the eyes on how continuous tuning over an octave can be achieved with four poling periods and only 30 nm of pump tuning.

Here, we design and demonstrate ultra-widely tunable doubly-resonant OPOs in lithium niobate nanophotonics. This is achieved by combining dispersion engineering, precise design of the spectral response of the cavity, and quasi-phase matching. With a pump tunable over 30 nm at around 1 um, we achieve wavelengths tunable from 1.53 μm to 3.25 μm from five OPOs on a single nanophotonic chip.

5.1 Results

The tuning concept of the OPOs is illustrated in Fig. 5.1a, where more than 1500 nm of tuning around 2 μm for the signal and idler is obtained by tuning the pump wavelength around 1 μm by less than 30 nm. It is worth noting that such a tuning range for the pump is already available from integrated distributed Bragg reflector (DBR) semiconductor lasers [21]. Such magnification in tuning range from the pump towards the signal and idler (a factor of ~12 in frequency units) is obtained through a dispersion-engineered quasi-phase matched OPO design with a spectrally-selective cavity as depicted in Fig. 5.1b. We use wavelength-selective couplers that allow the signal and idler wavelengths to resonate in the OPO cavity with a ~10-GHz free spectral range (FSR), while letting the pump go only through the poled waveguide section [22]. This differs sharply from previously demonstrated fully resonant on-chip OPO designs in which the pump also needs to satisfy a resonant condition limiting their flexibility and tunability. A chip containing 16 OPOs is fabricated, as shown in Fig. 5.1c, where we have highlighted a single OPO, which is also displayed in the false-color optical microscope image of Fig. 5.1d.

The simulated tuning behavior of four OPOs with different poling periods are shown in Figure 5.1e (solid black lines). These are obtained from conservation of energy ($\omega_p = \omega_s + \omega_i$) and momentum ($k_p = k_s + k_i + 2\pi/\Lambda_{QPM}$), so they can be tailored by engineering the waveguide dispersion [23]. In particular, as shown in Chapter 4, the signal tuning slope ($\partial\omega_s/\partial\omega_p$) is given by the ratio of group velocity differences $(1/v_i - 1/v_p)/(1/v_i - 1/v_s)$, while the gain-bandwidth is inversely proportional to $1/v_i - 1/v_s$. We have engineered the dispersion of the poled waveguide to balance these effects. As a result, a small change in the pump wavelength produces large changes in the output wavelengths while maintaining a predictable tuning curve without substantial mode competition (see Fig. 4.5).

To study the transient and steady-state behaviors of the nanophotonic OPOs we use pulses that are much longer than the cavity lifetime of the OPOs. This arrangement also allows us to use low average powers incident on the chip while maintaining high peak powers. The experimental setup is shown in Fig. 5.2a, which is described in detail in Section 5.3.

The measured OPO on-chip signal power at ~1950 nm is shown in Fig. 5.2b as a function of on-chip pump power (at 1050 nm). Only the signal (red squares) is measured, as the photodetector is not sensitive to the idler wave near 2275 nm. The idler power (purple circles) is estimated from the output coupler response (see Section 5.3). The solid black line is a fit based on a theoretical expression with an oscillation threshold of ~32 mW. Figure 5.2c shows the on-chip conversion efficiency, which has a maximum value of ~9 % for the signal, and up to ~15% when including the idler. This efficiency is limited by the escape efficiency of the OPO (see Section 5.3) which is currently low for the idler, and can be enhanced significantly with different coupler designs. Pump depletion characterizes the efficiency with which pump photons are converted into signal and idler photons inside the OPO (see

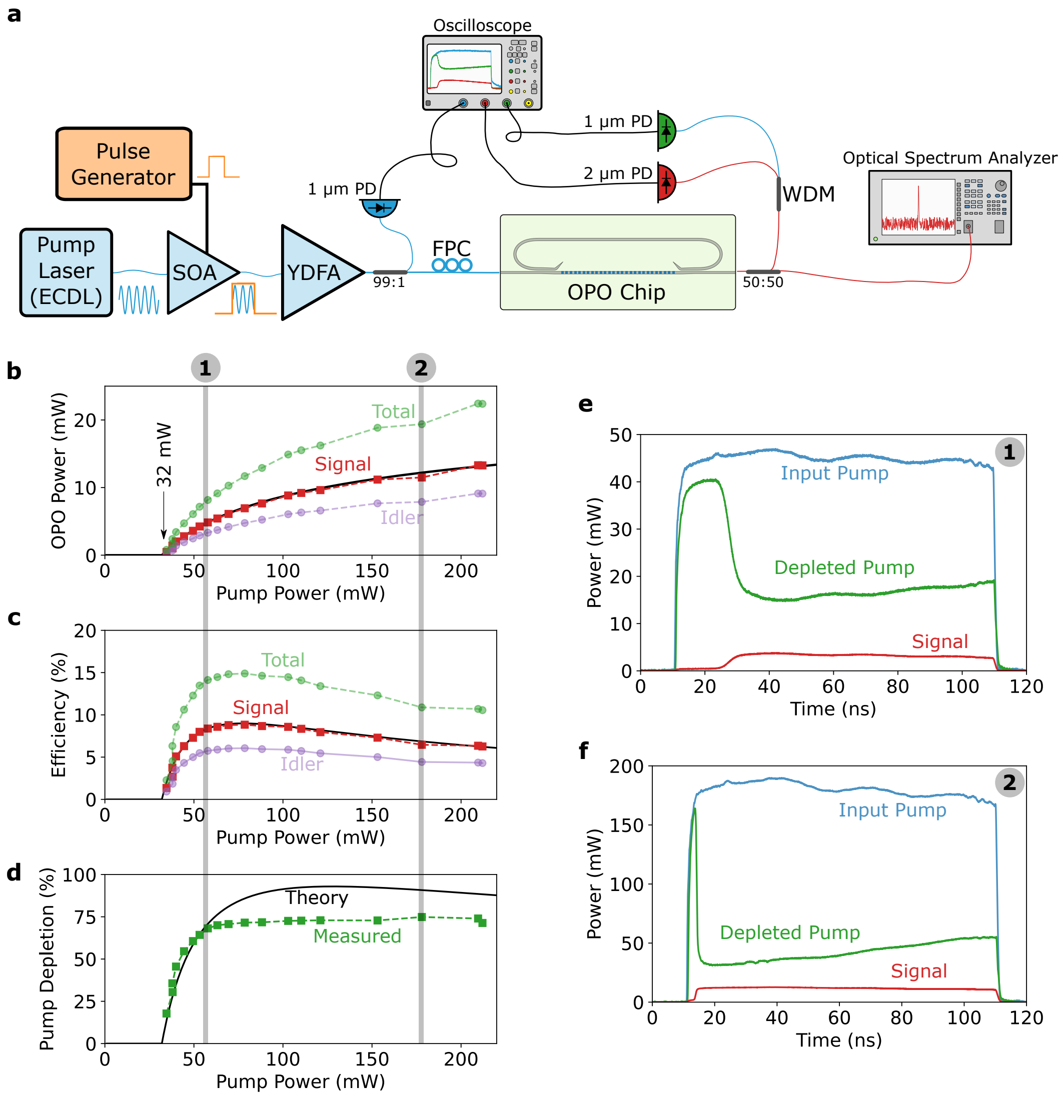

Figure 5.2: **Transient and steady-state measurements of on-chip doubly-resonant OPOs.** **a**, Measurement setup. We use 100-ns pulses with a 10-kHz repetition rate to decrease the average power while keeping the peak power above the OPO threshold. ECDL, external cavity diode laser; SOA, semiconductor optical amplifier; YDFA, ytterbium doped fiber amplifier; FPC, fiber polarization controller; OPO, optical parametric oscillator; PD, photodetector; WDM, wavelength division multiplexer. **b**, On-chip output power versus pump power for a signal wavelength of 1950 nm and a pump wavelength of 1050 nm, the idler and total power are estimated from the signal (see Section 5.3). **c**, Different measured on-chip efficiencies. **d**, Measured and expected pump depletion levels representing the conversion efficiency within the OPO. **e, f**, Measured pump and signal traces at two different power levels as indicated by the shaded gray regions in **b,c,d**.

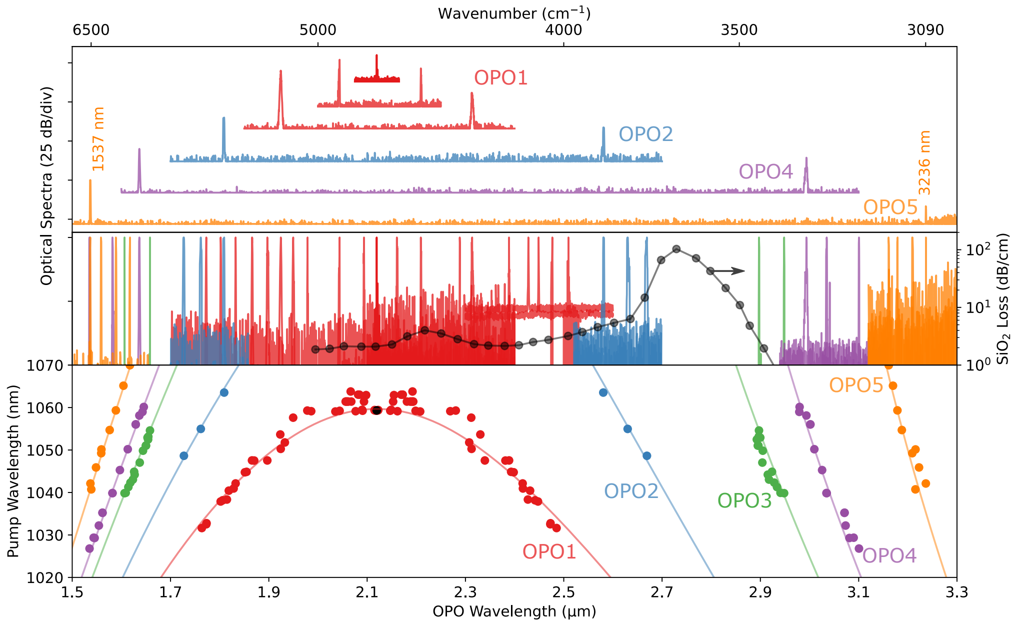

Figure 5.3: **Wavelength tuning of nanophotonic OPOs.** Top panel shows examples of output spectra for a few OPOs on the same chip exhibiting an octave-wide tuning range. Each color represents a different OPO. Middle panel shows many more output spectra from the same OPOs. Bottom panel includes all measured data (colored dots) with the corresponding pump wavelength on the vertical axes along with the theoretical tuning curves (solid lines).

Section 5.3). As shown in Fig. 5.2d, ~75% is observed, highlighting the potential of nanophotonic OPOs as extremely efficient wavelength conversion devices. These large pump depletion levels are also readily apparent from the oscilloscope traces shown in Fig. 5.2e,f.

Figure 5.3 shows the spectral tuning range of five OPOs fabricated on the same chip. The top panel of Fig. 5.3 shows few spectra of the signal and idler emission of the OPOs. This includes an OPO (OPO1 - red traces) that can operate at degeneracy (top trace), and an OPO (OPO5 - orange traces) that can achieve signal and idler wavelengths separated by more than an octave, and with an idler wavelength well into the mid-infrared.

More spectra from the same OPOs are shown in the middle panel of Fig. 5.3, demonstrating dense coverage over the entire spectral range, except for a band around ~2.8 μm where the SiO$_2$ buffer layer exhibits an absorption peak [24]. The tuning parameter in all these cases was the pump wavelength as illustrated in the vertical axis of the bottom panel. Note that OPO1 can be tuned between 1.76 μm and 2.51 μm (over 750 nm) by varying the pump wavelength by only 30 nm,

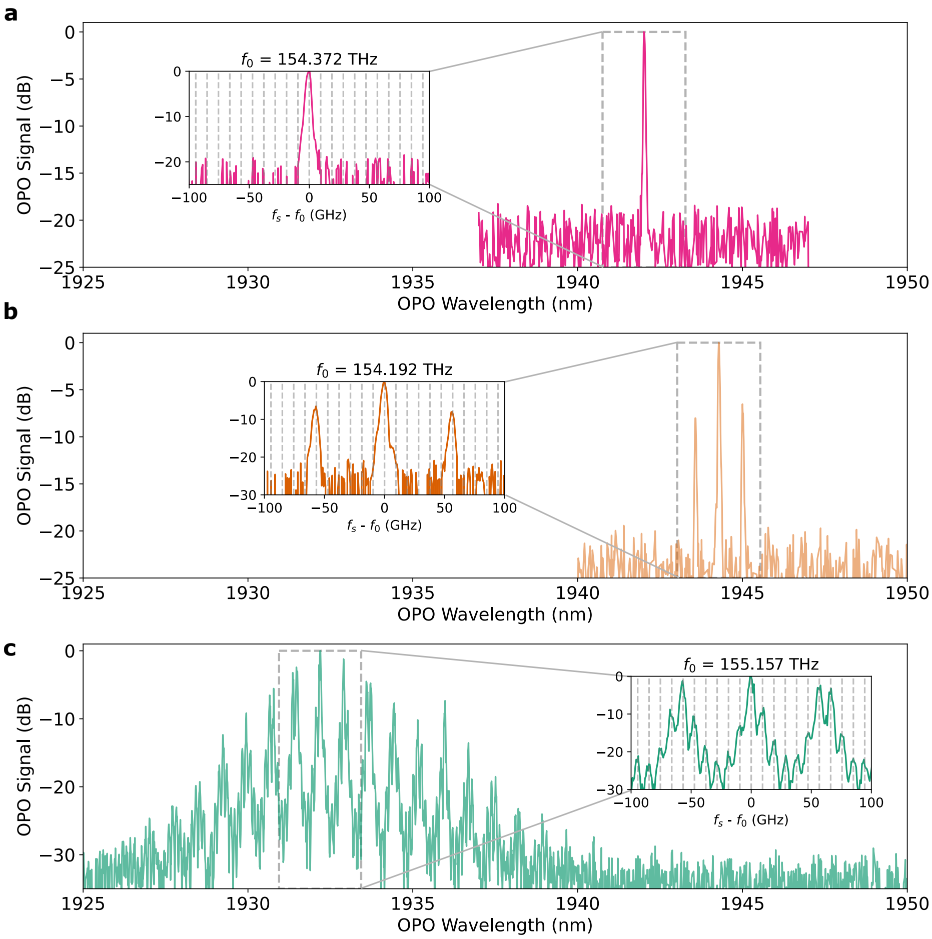

Figure 5.4: **Spectral structures of free-running OPOs.** The generated spectrum of our OPOs can vary from (**a**) single mode emission, to (**b**) emission in a few modes separated by several FSRs, to (**c**) emission in several mode clusters. Insets show close up of spectra with dashed vertical lines separated by the resonator's FSR which is approximately equal to the 10-GHz OSA resolution bandwidth.

corresponding to a tuning magnification factor of ~12 in frequency units. OPO1 can also operate at degeneracy by using a 1060-nm pump as shown in the topmost trace of the top panel, corresponding to the black dot in the bottom panel.

By tuning the pump power level, the OPOs can operate with a single mode, few modes, or multiple mode clusters, with examples shown in Fig. 5.4. Closer to threshold the OPOs can oscillate in a single spectral mode as shown in Fig. 5.4a. As the pump power is increased, oscillation in a few modes can occur as shown in Fig. 5.4b. Multiple mode clusters appear several times above threshold as shown in Fig. 5.4c. The multimode behavior is due to the parametric gain-bandwidth being larger than 1 THz, so a large number of modes (~10 GHz FSR) experience gain. At the

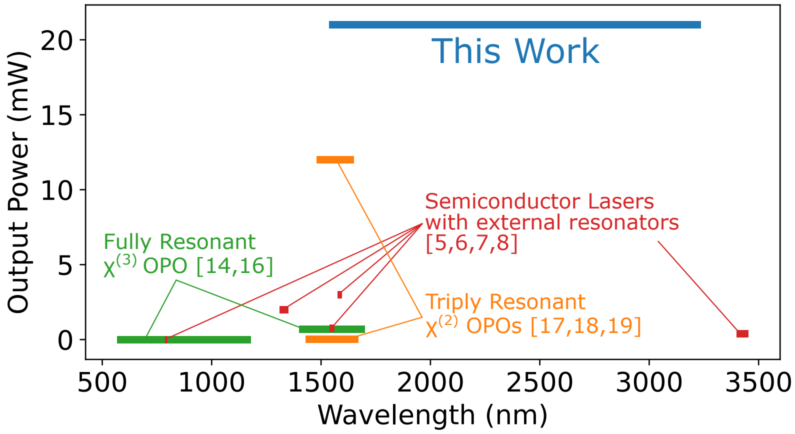

Figure 5.5: **Comparison of the on-chip output power and wavelength coverage of our on-chip OPOs with other integrated tunable sources.** The power level is the sum of signal and idler for all OPOs.

same time, waveguide dispersion causes a difference in FSR between signal and idler wavelengths which produces cluster effects in doubly-resonant OPOs well above the threshold [25]. Further dispersion and cavity engineering can be employed for either suppressing the multimode effects or tailoring it towards generation of frequency combs [26].

Figure 5.5 shows the tuning range and power level of our OPO chip alongside previously reported tunable sources in nanophotonics. Such significant performance is enabled by the novel non-resonant-pump OPO design combined with dispersion-engineered, quasi-phase matched, directly-etched waveguides (see Section 5.3).

5.2 Discussion

Our results show that ultra-widely tunable infrared sources can be implemented on the thin-film lithium niobate platform, adding to the increasingly large set of functionalities available in this platform [27], and complementing the recent demonstration of tunable near-infrared DBR lasers [21].

The threshold and required pump tuning range of our OPOs are within the reach of low-cost near-infrared laser diodes. Additional engineering of the cavity design, waveguide dispersion, and quasi-phase matching can be utilized for tailoring the operation towards a multitude of applications. For instance, the threshold of the OPOs can be substantially reduced by utilizing a separate resonator for the pump without sacrificing the conversion efficiency and tunability (unlike a triply-resonant design).

The maximum conversion efficiency of a doubly-resonant OPO is dominated by its escape efficiency, which is related to the ratio of output coupler transmittance to total resonator losses (see Section 5.3). For our device, this ratio is ~9% at 1950 nm, indicating that the output coupling is small compared to the total losses in the resonator. This could be caused in part by the little transmission of the output coupler, particularly at mid-infrared wavelengths, and in part by intrinsic resonator losses and losses at the input coupler. Fine tuning of the coupler designs and reducing the cavity loss can lead to substantial improvement of efficiency. We used adiabatic couplers in this work since they provide a simple means to approximately achieve our requirements of high signal and idler coupling together with low pump coupling. However, the input coupler should, ideally, have 100% coupling at signal and idler frequencies since any transmission in this coupler behaves as additional resonator loss, leading to higher thresholds and lower efficiencies. Simultaneously, the input coupler should provide very low coupling at the pump wavelength, since any coupling just leaks pump power into the unused port, and also provides an undesired feedback path for the pump. These characteristics may be achievable through more advanced coupler designs, for instance, those obtained by inverse design methods [28].

The tuning range of a single OPO can be further enhanced by implementing multiple poling periods on the same OPO. Moreover, since the wavelength coverage of the OPO appears to be limited by the loss of the SiO_2 buffer layer, a similar design with a different buffer layer material can allow operation towards the entire lithium niobate transparency window [29]. The OPO design we demonstrate here can also be readily applied to other emerging nonlinear photonic platforms with transparency windows deeper into the mid-infrared [30].

The measurements presented in Fig. 5.3 only exploit the dependence of the output wavelength on pump wavelength. Two additional degrees of freedom are the temperature and the resonator's free spectral range (which could be varied, for instance, by electro-optic modulation of the resonator's feedback arm). These three variables combined can facilitate precise and fast tuning of the output wavelengths over a much broader spectral range [25], especially when an integrated pump laser is used.

Singly-resonant OPOs offer even smoother tunability and stability characteristics at the expense of higher threshold powers. While pure singly resonant behavior can be

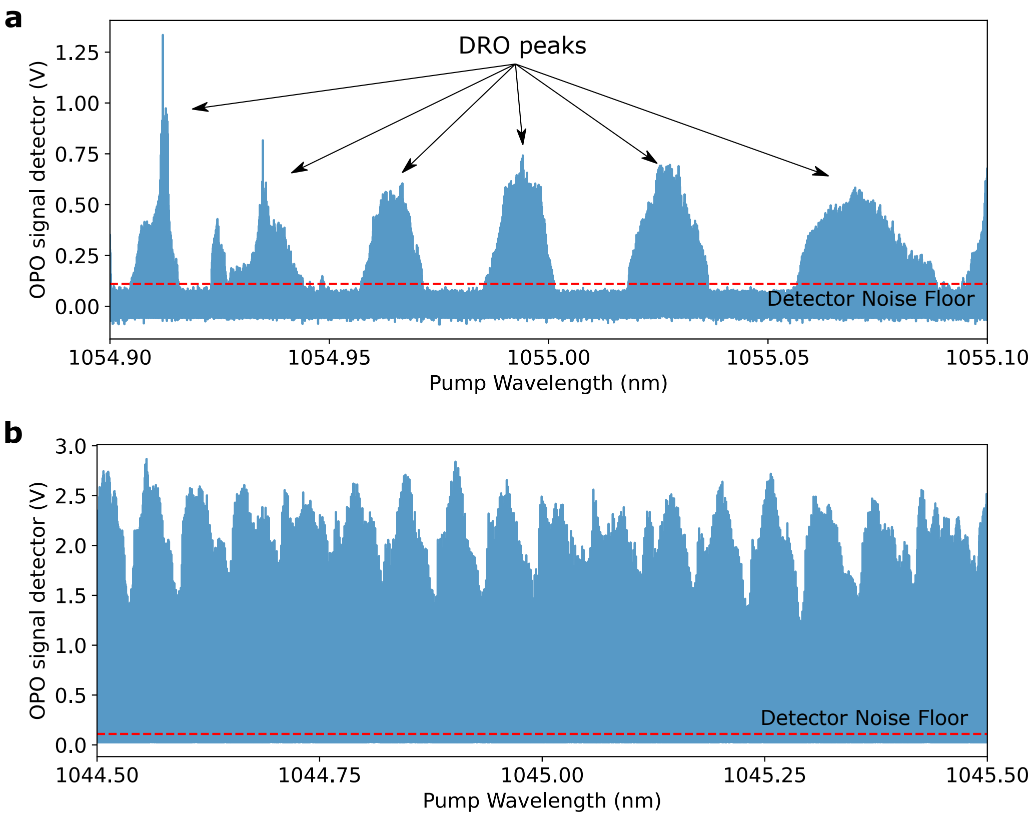

Figure 5.6: **Doubly-resonant and singly resonant regimes.** **a**, Detected OPO signal for low pump power showing isolated oscillation peaks. This phenomenon, known as cluster effects in doubly-resonant OPOs (DROs), is due to the difference between the free spectral range at signal and idler wavelengths produced by waveguide dispersion. **b**, At larger pump powers the OPO oscillates for any pump wavelength. This is because away from a doubly-resonant cluster, the OPO operates closer to the singly resonant regime, with a strongly resonant idler and a weakly resonant signal that is free to adjust itself to a frequency $\omega_s = \omega_p - \omega_i$. In both, **a** and **b**, signal power variations are due to a combination of threshold variations and wavelength dependent pump laser power.

obtained by changing the coupler response so that only the signal or idler resonates, we note that the transition between doubly- and singly-resonant designs is smooth [31] and we have evidence that our OPOs can operate in this regime (see Fig. 5.6). This could enable fast and ultrabroad wavelength synthesis on-chip with potential mode-hop free operation.

In summary, we have demonstrated on-chip doubly-resonant OPOs that can be tuned over an octave up to 3.25 μm. Our OPOs are based on a novel on-chip doubly-resonant design that avoids many of the challenges present in triply-resonant configurations and linear cavity oscillators, and can be easily extended to singly-resonant configurations. Further dispersion engineering may lead to femtosecond synchronously-pumped OPOs in nanophotonics and the numerous applications they unlock [32].

5.3 Materials and methods

Device design

We use adiabatic couplers to create the wavelength selective cavity as described in Chapter 4 and shown in Fig. 4.2. The input and output couplers are identical and are designed so that signal and idler wavelengths ($\lambda > 1.8$ μm) have large coupling factors ($> 80\%$) while pump wavelengths near 1 μm are only slightly coupled ($< 10\%$). The residual coupling of the pump leads to round-trip feedback factors of less than 1% that produce negligible modulations of the pump intensity as a function of frequency, allowing continuous tuning of the pump wavelength.

When designing a tunable OPO, it is desirable to have a large tuning slope so a small change in pump wavelength produces large changes in the output wavelengths. At the same time, a small gain-bandwidth is preferable to limit the number of resonator modes experiencing gain. To achieve a balance between these two behaviors, we engineer the dispersion of the waveguide using its geometry, resulting in 2.5-μm-wide waveguides on a 700-nm-thick lithium niobate layer and 250 nm of etching depth.

Device fabrication

We fabricate our devices using a commercial wafer (NANOLN) with an x-cut, 700-nm-thick MgO-doped lithium niobate layer and a SiO_2 buffer layer. We provide quasi-phase matching in a 5-mm-long region through periodic poling (inset of Fig. 5.1b shows a second-harmonic microscope image of a typical poled section). The waveguides are patterned by e-beam lithography and dry etched with Ar^+ plasma to a depth of 250 nm. All the OPOs have the same waveguide geometry obtained from dispersion engineering, with 2.3-μm-wide input and output waveguides that taper (through the adiabatic couplers) to 2.5-μm-wide waveguides inside the resonator. To maximize the spectral range covered on a single chip, we fabricated OPOs with poling periods ranging from 5.55 μm to 5.7 μm in 10-nm steps. We include a straight waveguide next to each OPO for calibration and quasi-phase matching verification (colored purple in Fig. 5.1b).

Device characterization

We characterize our OPOs using the experimental setup shown in Fig. 5.2a, that consists of a tunable CW 1-μm laser amplified by a semiconductor optical amplifier (SOA) which is modulated to generate 100-ns-long (full-width-half-maximum) pulses with 10-kHz repetition rate. These pulses are further amplified by an ytterbium doped fiber amplifier (YDFA) and coupled into the chip using a single-mode 1-μm lensed fiber (~10 dB coupling loss). The OPO output is collected either by a 2-μm lensed fiber, or a cleaved $\mathrm{InF_3}$ fiber, and sent to an optical spectrum analyzer (OSA) or to an InAsSb detector connected to an oscilloscope. A wavelength division multiplexer (WDM) allows us to monitor the depleted pump and signal output simultaneously.

To estimate propagation losses in our waveguides, we fabricated chips with arrays of critically coupled resonators and extracted quality factors ~6×10^5, which translate to losses below 0.3 dB/cm for waveguides without poling. Detailed inspection of the periodically poled waveguide inside the resonator reveals periodic roughness of the waveguide sidewalls, likely from the polarization-dependent etch rate of lithium niobate. More studies are needed to improve the resonator quality factor.

To estimate input and output coupling losses, we use single mode lensed fibers to coupled into and out of the chip and then divide the total throughput loss equally between both interfaces. We do this on several unpoled straight waveguides and obtain a coupling coefficient varying from 10 dB to 13 dB, with 10 dB giving the most conservative estimate for on-chip input power. When using an asymmetric setup (lensed fiber at input, cleaved fiber at ouput), we assume the input coupling remains at 10 dB and calculate the output coupling from the throughput loss. Comparing transmission of straight waveguides to that of OPOs allows to estimate a total loss factor of 0.929 per coupler at the pump wavelength, reasonably close to the simulated value of 0.95 (Fig. 4.2). The plots of Fig.2b-d are obtained from oscilloscope traces like those in Fig.2e,f by first converting voltage to power, integrating them to find the energy, and then dividing by the 100-ns pulse width to obtain the average peak power.

Efficiency and idler power estimation

The efficiency of an OPO (η) can be written as the product of two efficiencies, $\eta = \eta_0 \eta_{\text{escape}}$. The internal efficiency (η_0) measures how efficiently pump photons are converted into signal and idler photons, while the escape efficiency (η_{escape})

measures the fraction of the generated signal and idler photons available at the output of the OPO. The difference between the pump power at the beginning and end of the gain section is $\Delta P_p = P_p(0) - P_p(L_g)$. The internal efficiency is just the pump depletion $\eta_0 = \Delta P_p / P_p(0)$ shown in Fig 2d.

The escape efficiency was derived in Chapter 4 as is given by

$$\eta_e(\omega) = \frac{\omega}{\omega_p} \frac{T(\omega)}{1 - L(\omega)},$$

where $T(\omega)$ is the power transmission coefficient of the output coupler, while $L(\omega)$ is the roundtrip power loss factor of the resonator. Since the output power can be calculated from the efficiency as $P_{\text{out}}(\omega) = \eta_0 \eta_e(\omega) P_p(0)$, the idler power can be calculated from the signal power as:

$$P_{\text{out}}(\omega_i) \approx \frac{\eta_e(\omega_i)}{\eta_e(\omega_s)} P_{\text{out}}(\omega_s).$$

References

[1] L. Ledezma, A. Roy, L. Costa, R. Sekine, R. Gray, Q. Guo, R. M. Briggs, and A. Marandi, "Widely-tunable optical parametric oscillator in lithium niobate nanophotonics," *arXiv:2203.11482 [physics]*, Mar. 2022. arXiv: `2203.11482 [physics]`.

[2] A. E. Willner, Ed., *Optical Fiber Telecommunications VII*. London ; San Diego, CA: Academic Press is an imprint of Elsevier, 2020, ISBN: 978-0-12-816502-7.

[3] Y. Jiang, S. Karpf, and B. Jalali, "Time-stretch LiDAR as a spectrally scanned time-of-flight ranging camera," *Nature Photonics*, vol. 14, no. 1, pp. 14–18, Jan. 2020, ISSN: 1749-4893. DOI: `10.1038/s41566-019-0548-6`.

[4] Gordon et al., "The HITRAN2020 molecular spectroscopic database," *Journal of Quantitative Spectroscopy and Radiative Transfer*, vol. 277, p. 107 949, Jan. 2022, ISSN: 0022-4073. DOI: `10.1016/j.jqsrt.2021.107949`.

[5] Y. Yao, A. J. Hoffman, and C. F. Gmachl, "Mid-infrared quantum cascade lasers," *Nature Photonics*, vol. 6, no. 7, pp. 432–439, Jul. 2012, ISSN: 1749-4893. DOI: `10.1038/nphoton.2012.143`.

[6] E. Shim, A. Gil-Molina, O. Westreich, Y. Dikmelik, K. Lascola, A. L. Gaeta, and M. Lipson, "Tunable single-mode chip-scale mid-infrared laser," *Communications Physics*, vol. 4, no. 1, pp. 1–7, Dec. 2021, ISSN: 2399-3650. DOI: `10.1038/s42005-021-00770-6`.

[7] Y. Han, Y. Han, X. Zhang, X. Zhang, R. Ma, M. Xu, H. Tan, J. Liu, R. Wang, S. Yu, and X. Cai, “Widely tunable O-band lithium niobite/III-V transmitter,” *Optics Express*, vol. 30, no. 20, pp. 35 478–35 485, Sep. 2022, ISSN: 1094-4087. DOI: `10.1364/OE.471402`.

[8] M. Li, L. Chang, L. Wu, J. Staffa, J. Ling, U. A. Javid, S. Xue, Y. He, R. Lopez-rios, T. J. Morin, H. Wang, B. Shen, S. Zeng, L. Zhu, K. J. Vahala, J. E. Bowers, and Q. Lin, “Integrated Pockels laser,” *Nature Communications*, vol. 13, no. 1, p. 5344, Sep. 2022, ISSN: 2041-1723. DOI: `10.1038/s41467-022-33101-6`.

[9] C. O. de Beeck, F. M. Mayor, S. Cuyvers, S. Poelman, J. F. Herrmann, O. Atalar, T. P. McKenna, B. Haq, W. Jiang, J. D. Witmer, G. Roelkens, A. H. Safavi-Naeini, R. V. Laer, and B. Kuyken, “III/V-on-lithium niobate amplifiers and lasers,” *Optica*, vol. 8, no. 10, pp. 1288–1289, Oct. 2021, ISSN: 2334-2536. DOI: `10.1364/OPTICA.438620`.

[10] M. H. Dunn and M. Ebrahimzadeh, “Parametric generation of tunable light from continuous-wave to femtosecond pulses,” *Science*, vol. 286, no. 5444, pp. 1513–1517, Nov. 1999, ISSN: 0036-8075, 1095-9203. DOI: `10.1126/science.286.5444.1513`.

[11] C. Langrock and M. M. Fejer, “Fiber-feedback continuous-wave and synchronously-pumped singly-resonant ring optical parametric oscillators using reverse-proton-exchanged periodically-poled lithium niobate waveguides,” *Optics Letters*, vol. 32, no. 15, pp. 2263–2265, Aug. 2007, ISSN: 1539-4794. DOI: `10.1364/OL.32.002263`.

[12] M. Savanier, C. Ozanam, L. Lanco, X. Lafosse, A. Andronico, I. Favero, S. Ducci, and G. Leo, “Near-infrared optical parametric oscillator in a III-V semiconductor waveguide,” *Applied Physics Letters*, vol. 103, no. 26, p. 261 105, Dec. 2013, ISSN: 0003-6951. DOI: `10.1063/1.4853595`.

[13] N. Amiune, D. N. Puzyrev, V. V. Pankratov, D. V. Skryabin, K. Buse, and I. Breunig, “Optical-parametric-oscillation-based $\chi(2)$ frequency comb in a lithium niobate microresonator,” *Optics Express*, vol. 29, no. 25, pp. 41 378–41 387, Dec. 2021. DOI: `10.1364/OE.440206`. [Online]. Available: `https://opg.optica.org/oe/abstract.cfm?URI=oe-29-25-41378`.

[14] C. Wang, C. Langrock, A. Marandi, M. Jankowski, M. Zhang, B. Desiatov, M. M. Fejer, and M. Lončar, “Ultrahigh-efficiency wavelength conversion in nanophotonic periodically poled lithium niobate waveguides,” *Optica*, vol. 5, no. 11, pp. 1438–1441, Nov. 2018, ISSN: 2334-2536. DOI: `10.1364/OPTICA.5.001438`.

[15] L. Razzari, D. Duchesne, M. Ferrera, R. Morandotti, S. Chu, B. E. Little, and D. J. Moss, “CMOS-compatible integrated optical hyper-parametric oscillator,” *Nature Photonics*, vol. 4, no. 1, pp. 41–45, Jan. 2010, ISSN: 1749-4893. DOI: `10.1038/nphoton.2009.236`.

[16] X. Lu, G. Moille, A. Singh, Q. Li, D. A. Westly, A. Rao, S.-P. Yu, T. C. Briles, S. B. Papp, and K. Srinivasan, "Milliwatt-threshold visible–telecom optical parametric oscillation using silicon nanophotonics," *Optica*, vol. 6, no. 12, pp. 1535–1541, Dec. 2019, ISSN: 2334-2536. DOI: `10.1364/OPTICA.6.001535`.

[17] X. Lu, G. Moille, A. Rao, D. A. Westly, and K. Srinivasan, "On-chip optical parametric oscillation into the visible: Generating red, orange, yellow, and green from a near-infrared pump," *Optica*, vol. 7, no. 10, pp. 1417–1425, Oct. 2020, ISSN: 2334-2536. DOI: `10.1364/OPTICA.393810`.

[18] A. W. Bruch, X. Liu, J. B. Surya, C.-L. Zou, and H. X. Tang, "On-chip $\chi^{(2)}$ microring optical parametric oscillator," *Optica*, vol. 6, no. 10, pp. 1361–1366, Oct. 2019, ISSN: 2334-2536. DOI: `10.1364/OPTICA.6.001361`.

[19] J. Lu, A. A. Sayem, Z. Gong, J. B. Surya, C.-L. Zou, and H. X. Tang, "Ultralow-threshold thin-film lithium niobate optical parametric oscillator," *Optica*, vol. 8, no. 4, pp. 539–544, Apr. 2021, ISSN: 2334-2536. DOI: `10.1364/OPTICA.418984`.

[20] T. P. McKenna, H. S. Stokowski, V. Ansari, J. Mishra, M. Jankowski, C. J. Sarabalis, J. F. Herrmann, C. Langrock, M. M. Fejer, and A. H. Safavi-Naeini, "Ultra-low-power second-order nonlinear optics on a chip," *Nature Communications*, vol. 13, no. 1, p. 4532, Aug. 2022, ISSN: 2041-1723. DOI: `10.1038/s41467-022-31134-5`.

[21] P. A. Verrinder, L. Wang, J. Fridlander, F. Sang, V. Rosborough, M. Nickerson, G. Yang, M. Stephen, L. Coldren, and J. Klamkin, "Gallium Arsenide Photonic Integrated Circuit Platform for Tunable Laser Applications," *IEEE Journal of Selected Topics in Quantum Electronics*, vol. 28, no. 1: Semiconductor Lasers, pp. 1–9, Jan. 2022, ISSN: 1558-4542. DOI: `10.1109/JSTQE.2021.3086074`.

[22] A. Marandi, L. Ledezma, Y. Xu, and R. M. Briggs, "Thin-film optical parametric oscillators," U.S. Patent 11,226,538.

[23] L. Ledezma, R. Sekine, Q. Guo, R. Nehra, S. Jahani, and A. Marandi, "Intense optical parametric amplification in dispersion-engineered nanophotonic lithium niobate waveguides," *Optica*, vol. 9, no. 3, pp. 303–308, Mar. 2022, ISSN: 2334-2536. DOI: `10.1364/OPTICA.442332`.

[24] R. A. Soref, S. J. Emelett, and W. R. Buchwald, "Silicon waveguided components for the long-wave infrared region," *Journal of Optics A: Pure and Applied Optics*, vol. 8, no. 10, pp. 840–848, Aug. 2006, ISSN: 1464-4258. DOI: `10.1088/1464-4258/8/10/004`.

[25] R. C. Eckardt, C. D. Nabors, W. J. Kozlovsky, and R. L. Byer, "Optical parametric oscillator frequency tuning and control," *Journal of the Optical Society of America B*, vol. 8, no. 3, p. 646, Mar. 1991, ISSN: 0740-3224, 1520-8540. DOI: `10.1364/JOSAB.8.000646`.

[26] S. Mosca, M. Parisi, I. Ricciardi, F. Leo, T. Hansson, M. Erkintalo, P. Maddaloni, P. De Natale, S. Wabnitz, and M. De Rosa, "Modulation instability induced frequency comb generation in a continuously pumped optical parametric oscillator," *Physical Review Letters*, vol. 121, p. 093 903, 9 Aug. 2018. DOI: `10.1103/PhysRevLett.121.093903`. [Online]. Available: `https://link.aps.org/doi/10.1103/PhysRevLett.121.093903`.

[27] D. Zhu, L. Shao, M. Yu, R. Cheng, B. Desiatov, C. J. Xin, Y. Hu, J. Holzgrafe, S. Ghosh, A. Shams-Ansari, E. Puma, N. Sinclair, C. Reimer, M. Zhang, and M. Lončar, "Integrated photonics on thin-film lithium niobate," *Advances in Optics and Photonics*, vol. 13, no. 2, pp. 242–352, Jun. 2021, ISSN: 1943-8206. DOI: `10.1364/AOP.411024`.

[28] S. Molesky, Z. Lin, A. Y. Piggott, W. Jin, J. Vucković, and A. W. Rodriguez, "Inverse design in nanophotonics," *Nature Photonics*, vol. 12, no. 11, pp. 659–670, Nov. 2018, ISSN: 1749-4893. DOI: `10.1038/s41566-018-0246-9`.

[29] J. Mishra, T. P. McKenna, E. Ng, H. S. Stokowski, M. Jankowski, C. Langrock, D. Heydari, H. Mabuchi, M. M. Fejer, and A. H. Safavi-Naeini, "Mid-infrared nonlinear optics in thin-film lithium niobate on sapphire," *Optica*, vol. 8, no. 6, pp. 921–924, Jun. 2021, ISSN: 2334-2536. DOI: `10.1364/OPTICA.427428`.

[30] R. Becheker, M. Bailly, S. Idlahcen, T. Godin, B. Gerard, H. Delahaye, G. Granger, S. Fèvrier, A. Grisard, E. Lallier, and A. Hideur, "Optical parametric generation in OP-GaAs waveguides pumped by a femtosecond fluoride fiber laser," *Optics Letters*, vol. 47, no. 4, pp. 886–889, Feb. 2022, ISSN: 1539-4794. DOI: `10.1364/OL.443896`.

[31] S. T. Yang, R. C. Eckardt, and R. L. Byer, "Power and spectral characteristics of continuous-wave parametric oscillators: The doubly to singly resonant transition," *Journal of the Optical Society of America B*, vol. 10, no. 9, pp. 1684–1695, Sep. 1993, ISSN: 1520-8540. DOI: `10.1364/JOSAB.10.001684`.

[32] Y. Kobayashi, K. Torizuka, A. Marandi, R. L. Byer, R. A. McCracken, Z. Zhang, and D. T. Reid, "Femtosecond optical parametric oscillator frequency combs," *Journal of Optics*, vol. 17, no. 9, p. 094 010, Sep. 2015, ISSN: 2040-8986. DOI: `10.1088/2040-8978/17/9/094010`.

Chapter 6

TUNABLE FREQUENCY COMBS FROM SYNCHRONOUSLY PUMPED OPTICAL PARAMETRIC OSCILLATORS

Optical frequency combs consisting of several spectral lines with accurate frequencies are at the core of a plethora of modern-day applications [2], [3], including spectroscopy [4], optical communication [5], optical computing [6], atomic clocks [7], ranging [8], [9], and imaging [10]. Many of these applications demand optical frequency combs in the technologically important mid-infrared [11], [12] and visible [13], [14] spectral regimes. Accessing optical frequency comb sources in integrated photonic platforms is of paramount importance for the translation of many of these technologies to real-world applications and devices [15]. Despite outstanding progress in that direction in the near-infrared, there is a dearth of widely tunable frequency comb sources, especially in the highly desired mid-infrared and visible spectral regimes.

Notable efforts on miniaturized mid-IR comb sources typically rely on supercontinuum generation, and/or intra-pulse difference frequency generation [16], [17]. Not only do these nonlinear processes usually require a femtosecond pump as an input (which has its own challenges for efficient on-chip manifestation), but their power is also distributed over a wide frequency range including undesired spectral bands. Engineered semiconductor devices like quantum cascade lasers have successfully been demonstrated as mid-infrared frequency comb sources [18], however, they are not tunable over a broad wavelength range and are still difficult to operate in the ultrashort pulse regime [19], [20]. The situation is exacerbated by the lack of a suitable laser gain medium that is amenable to room temperature operation in the mid-IR. Kerr nonlinearity can lead to tunable broadband radiation [21]–[23] but is contingent on satisfying demanding resonator quality factor requirements and typically relies on a mid-IR pump to begin with for subsequent mid-infrared frequency comb generation. Similar challenges exist for Raman-based mid-IR frequency comb generation [24].

This chapter is adapted from A. Roy, L. Ledezma, L. Costa, *et al.*, "Visible-to-mid-IR tunable frequency comb in nanophotonics," *arXiv*, Dec. 2022. DOI: `10.48550/arXiv.2212.08723`.

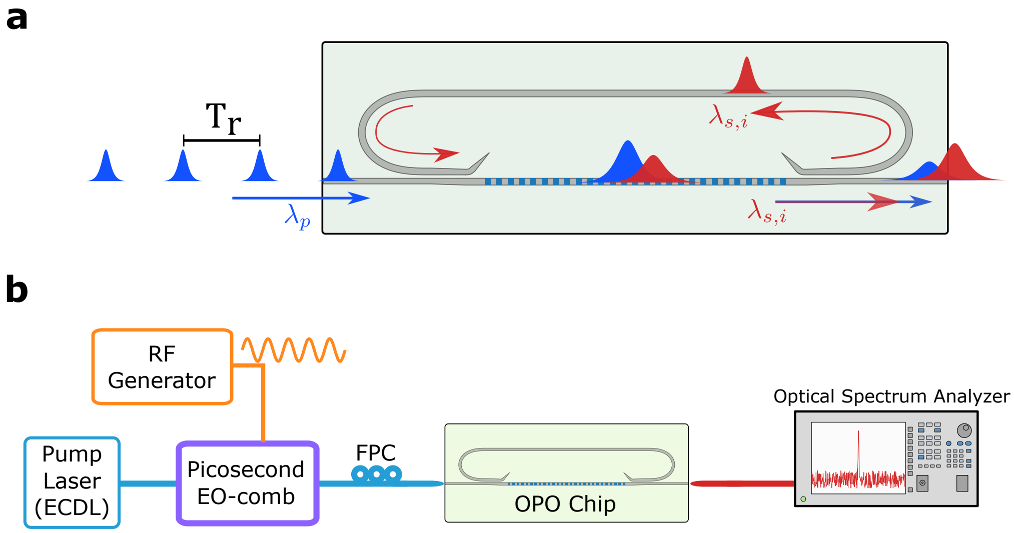

Figure 6.1: **Synchronously pumped optical parametric oscillators.** **a**, A train of pulses centered at λ_p drives an optical parametric oscillator generating signal and idler pulses centered at λ_s and λ_i. The repetition rate T_r of the pump pulses is close to the round-trip time of the signal and/or idler pulses. **b**, Characterization setup used to synchronously pump and measure the on-chip parametric oscillator. The setup includes the generation of a picosecond electro-optic frequency comb.

On the other hand, optical parametric oscillators (OPOs) based on quadratic nonlinearity have been the predominant way of accessing tunable coherent radiation in the mid-IR spectral region enjoying broadband tunability through appropriate phase matching of the three-wave mixing [11]. However, their impressive generation of tunable frequency combs in the mid-infrared have been limited to bulky free-space configurations pumped by femtosecond lasers [25], [26]. Recently, integrated quadratic OPOs are realized in the near-IR, using high-Q resonators with pump-resonant designs [27]–[29], which have not been able to access the broad tunability of phase matching and mid-IR frequency comb generation.

We demonstrate ultra-widely tunable frequency comb generation from on-chip OPOs in lithium niobate nanophotonics. Leveraging the ability to control the phase-matching via periodic poling combined with dispersion engineering, we show an on-chip tuning range that exceeds an octave. We pump the OPOs with picosecond pulses from an electro-optic frequency comb source in the near-IR, which is already demonstrated to be compatible with nanophotonic lithium niobate [30]–[32]. The demonstrated frequency combs cover the typical communication bands and extend into the mid-infrared spectral region beyond 3 μm with instantaneous bandwidths supporting sub-picosecond pulse duration. Additionally, the same chip produces tunable frequency combs in the visible resulting from up-conversion processes. Tunable visible frequency comb realization has been challenging owing to the absence of a suitable broadband gain medium and the typical large normal dispersion at these wavelengths in most integrated photonic platforms [16], [33].

6.1 Results

We achieve broadband and widely-tunable frequency combs using the doubly-resonant OPO design from previous chapters with a 5-mm-long poled waveguide. As shown in Fig. 6.1a, a train of pulses with a repetition rate T_r centered near $\lambda_p = 1045$ nm is used to pump the OPO. Synchronous pumping is obtained by matching the roundtrip time of the signal or idler to that of the repetition rate of the pump [34]–[36]. Having a non-resonant pump simplifies the synchronicity condition and also enables the tunability of the pump comb center frequency for wide tuning of the OPO outputs.

The characterization setup is shown in Fig. 6.1b. The OPO is synchronously pumped by an electro-optic frequency comb whose repetition rate is either matched to the fundamental repetition rate of the resonator (~9.5 GHz) or its second harmonic (~19 GHz). This harmonic harmonic repetition rate operation leads to wider instantaneous bandwidth and shorter electro-optic pump pulses. The pump pulse width is approximately 1 ps long. Based on our available electronics, the repetition rate can be tuned from 5 GHz to 20 GHz (the upper limit is dictated by the bandwidth of the RF amplifiers). The electro-optic frequency comb generation scheme closely follows the approach demonstrated in [37], [38]. The center frequency can be tuned from 1040 nm to 1065 nm, limited by the operating range of the waveshaper and fiber amplifier.

A more detailed schematic of the pump preparation setup is shown in Fig. 6.2a. The output of a tunable CW laser is modulated by a series of modulators. The modulators are driven by an RF signal generator followed by an RF amplifier. The intensity modulator (IM) bias is chosen such that pulses can be carved out from the continuous wave. At this stage, the time domain output resembles the simulated waveform shown in Fig. 6.2b. Next, a cascade of three phase modulators (PM) enables the addition of spectral sidebands which are separated by the repetition rate. The phase modulators are driven in synchrony by adjusting the electronic delay lines. At this stage, the spectrum will be similar to the one shown in Fig. 6.2c. The resultant signal is amplified with the help of a semiconductor optical amplifier

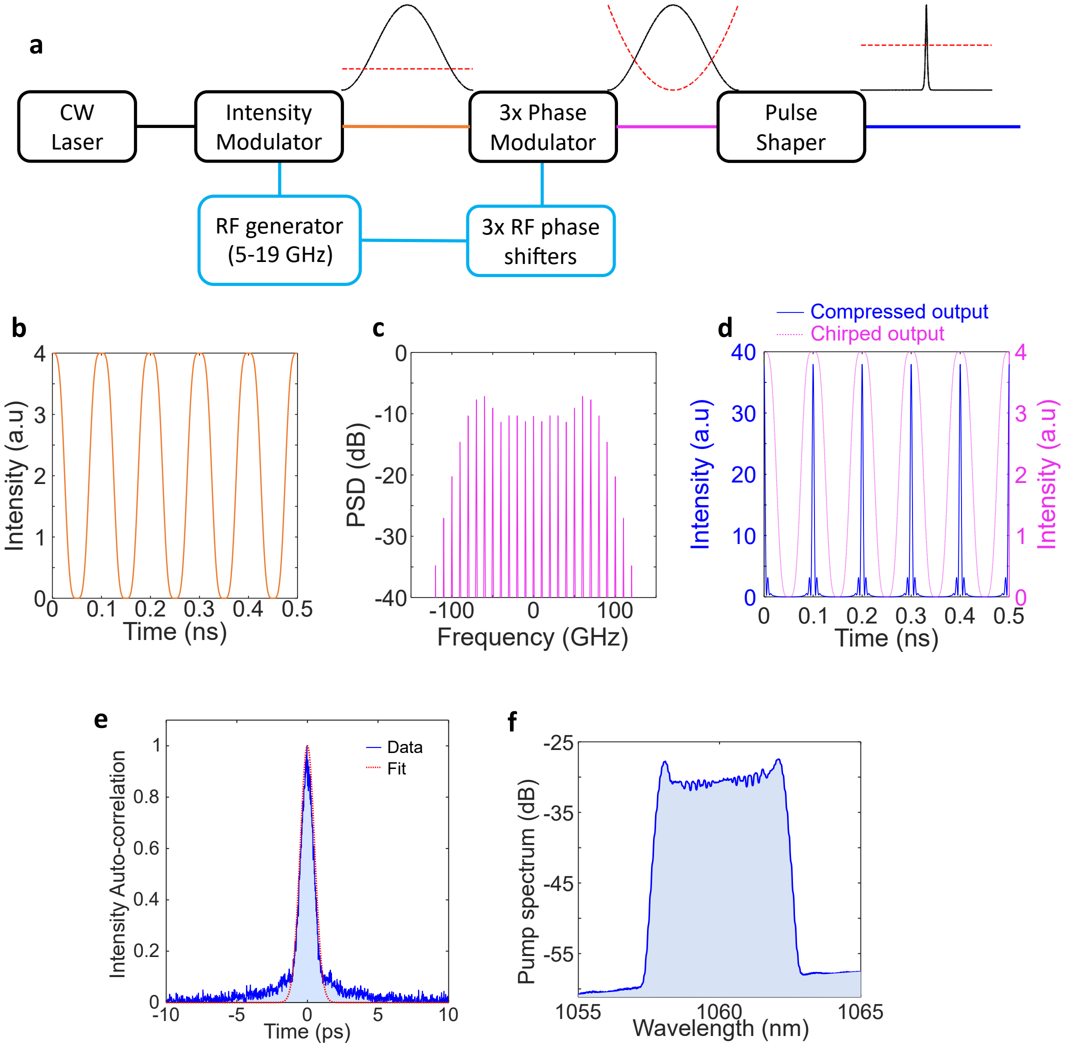

Figure 6.2: **Pump preparation with electro-optic frequency comb.** **a**, A CW external-cavity diode laser is modulated in amplitude and phase to generate a highly chirped sinusoidal pulse. A pulse shaper then compresses this pulse to its transform limited form. **b**, Simulated pulse intensity after the intensity modulator for an RF frequency of 10 GHz. **c**, Simulated spectra after the phase modulators. **d**, Simulated intensity before and after the pulse shaper. **e**, Measured final intensity auto-correlation trace along with a fit corresponding to a Gaussian pulse with a 1-ps width. **f**, Measured final pump spectrum.

(SOA) and then sent to a waveshaper. The programmable waveshaper allows the compression of the pulses by de-chirping the input temporal waveform through the application of suitable dispersion. At this point, the time domain waveform will look like the one shown in Fig. 6.2d, where both the compressed pulses as well as the pre-compressed chirped pulses are shown. Finally, the electro-optic frequency

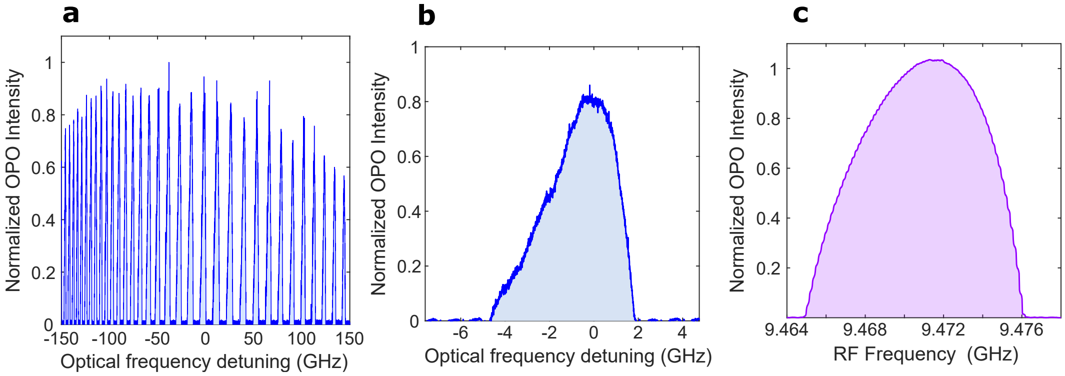

Figure 6.3: **Resonance peaks of on-chip synchronously pumped OPOs.** **a**, Resonance peak structure obtained by sweeping the pump central wavelength which is typical of doubly-resonant OPO operation. **b**, A zoomed-in view of a single peak from **a**. **c** Range of existence of the synchronously pumped OPO for a fixed pump power as the pump repetition rate is varied.

comb is characterized in the time domain using an intensity auto-correlator (Fig. 6.2e), and in the frequency domain using an optical spectrum analyzer (Fig. 6.2f).

The doubly-resonant operation of the OPO is confirmed by the appearance of the resonance peak structure with the variation of the pump central wavelength as shown in Fig. 6.3a,b. As shown in Fig. 6.3c, the on-chip OPO is fairly tolerant to synchronous pumping repetition rate mismatch with respect to the optimum OPO operating point. However, estimating the free spectral range of the cavity (FSR) to within this accuracy is a challenging but central task since the sync pump (EO comb) cannot be tuned continuously to search for the right FSR. Each setting of the EO comb requires a specific combination of the electronic phase delay line parameters and the waveshaper dispersion parameter, adjusting which is an arduous task. The design of our OPO precludes the use of a tunable CW source around 1 μm to scan through multiple cavity resonances. The situation is exacerbated in the absence of a high-power tunable CW source of around 2 μm at our disposal.

To solve this issue, we use a simplified version of the eo-comb in which we remove the phase modulators and just keep the intensity modulator that we use to apply a variable modulation on top of the CW laser. The frequency of modulation is varied using an arbitrary waveform generator. The output of the OPO will be maximized in the vicinity of the correct cavity FSR. The pump center wavelength and modulation frequency can be continuously tuned in this setup, unlike the case of the complete electro-optic comb.

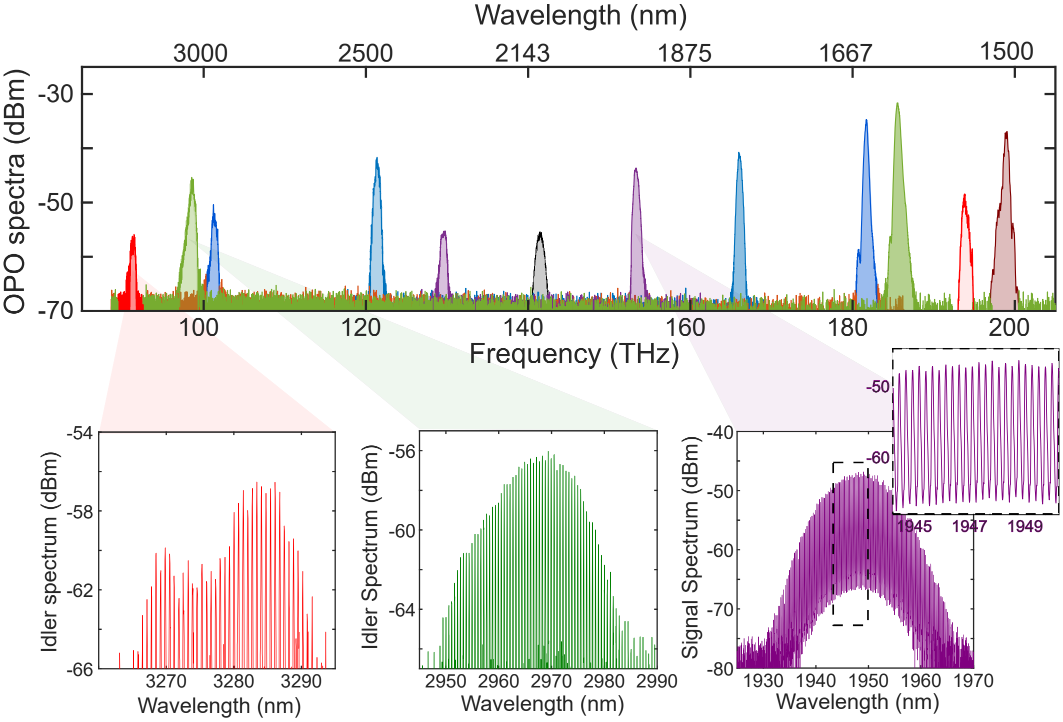

Figure 6.4: **Coarse tuning of mid-infrared frequency combs.** Broadband infrared spectral coverage of the OPO chip showing the signal and the idler spectrum as its operation is tuned from degeneracy to far non-degeneracy. Different colors represent outputs from different OPO devices on the same chip with distinct poling periods. Zoomed-in versions display the comb line structure.

The chip consists of multiple OPOs with different fixed poling periods (Λ_i), similar to the one described in Chapter 5. We use the different OPOs for coarse tuning and vary the pump wavelength over ~25 nm for fine-tuning. It is worth noting that this tuning range for the pump is compatible with the existing semiconductor lasers [39]. Moreover, the coarse switching of the poling period can be achieved without mechanical movements, for instance by means of electro-optic routing. In addition, temperature tuning of the poled region can provide another substantial tuning mechanism. The emission from the OPO chip covers important wavelengths corresponding to atomic transitions in the visible as well as molecular absorption lines in the mid-infrared.

Figure 6.4 shows the broad spectral coverage of the OPO output extending up to 3.3 μm in the mid-infrared obtained from a single chip. The comb lines can be resolved by the optical spectrum analyzer (OSA) and can be seen in the inset, where the separation of the peaks corresponds to the pump repetition rate. The on-chip threshold amounts to approximately 1 mW of average power (~50 mW of peak

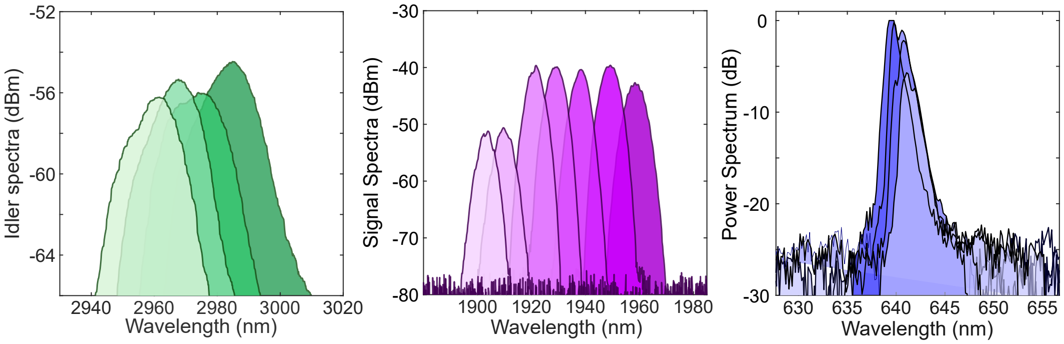

Figure 6.5: **Fine tuning of frequency combs.** Shown in the mid-IR, near-IR, and visible ranges. The tuning shown here is enabled by varying the pump central wavelength.

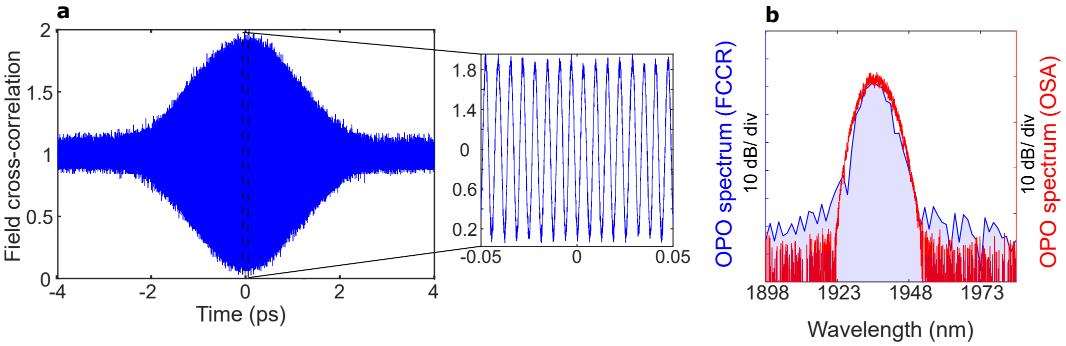

Figure 6.6: **Coherence measurements of on-chip frequency combs. a**, Verification of the coherence of the OPO output as evident from the existence of interference fringes (see inset) in the electric-field cross-correlation trace (FCCR). **b**, The close agreement between the spectra obtained from an optical spectrum analyzer measurement and that obtained by Fourier transforming the field cross-correlation corroborates the coherence of the OPO output.

power, and ~100 femtojoules of pulse energy) for the near-degenerate OPOs. The signal conversion efficiency approaches ~5% for the near-degenerate OPOs, while the mid-infrared (3.3 μm) idler conversion efficiency exceeds 1% for the far non-degenerate OPOs. This corresponds to an estimated ~25 mW of peak power and ~5 μW of power per comb line in the mid-infrared.

The fine tunability of the OPO output spectra, including in the mid-IR, near-IR, and visible ranges, as offered by tuning the pump wavelength, is depicted in Fig. 6.5. The combination of fine tunability and course tunability potentially enables continuous spectral coverage across the accessible spectral region.

We further evaluate the coherence of the output frequency comb by performing a linear field cross-correlation of the output signal light as shown in Fig. 6.6a, where each OPO pulse is interfered with another pulse delayed by 10 round-trips. This can be thought of being a modified FTIR measurement, where instead of performing auto-correlation we are executing cross-correlation. The delay line corresponds to a delay of 10 OPO pulses, and thus the coherence property evaluation is limited by the applied delay duration. The scanning stage nonlinearity is corrected using a reference HeNe laser beam.

The presence of the interference fringes (explicitly apparent in the inset of Fig. 6.6a), combined with the consistency of the Fourier transform of the cross-correlation trace and the signal spectrum obtained using an OSA, serve as evidence for the coherence of the output frequency comb over the entire spectrum (see Fig. 6.6b). Finally, we also detect a sharp RF beat-frequency corresponding to the applied repetition rate of the sync-pumped OPO. The signal is obtained by measuring the OPO output pulses using a fast photo-detector. The pump is rejected using a wavelength de-multiplexer.

The occurrence of other quadratic nonlinear processes, namely second harmonic generation (SHG) and sum-frequency generation (SFG), leads to frequency comb formation in the visible spectral region. The complete emission spectrum of an OPO consisting of the second harmonic of the pump and the signal waves, the sum frequency components between the pump and the signal/idler waves along with the usual signal/idler is shown in Fig. 6.7a. These were recorded using a combination of a near-infrared optical spectrum analyzer (OSA) (Yokogawa AQ6374), mid-infrared OSAs (Yokogawa AQ6375B, AQ6376E), and a CCD spectrometer (Thorlabs CCS200). The scattered visible light emanating from the chip is captured by the optical microscope image (see Fig. 6.7b) showing the emission of the pump second harmonic (green) and the sum frequency components (red). Note that in the poling region, green dominates at the input side, which progressively is overpowered by the sum-frequency red component. The SFG between the pump and the signal waves leads to tunable visible frequency comb generation between 600 nm and 700 nm as shown in Fig. 6.7c. Tuning the OPO farther from degeneracy leads to idler emission further into the mid-IR as well as the SFG component that lies to the bluer side of the visible spectrum.

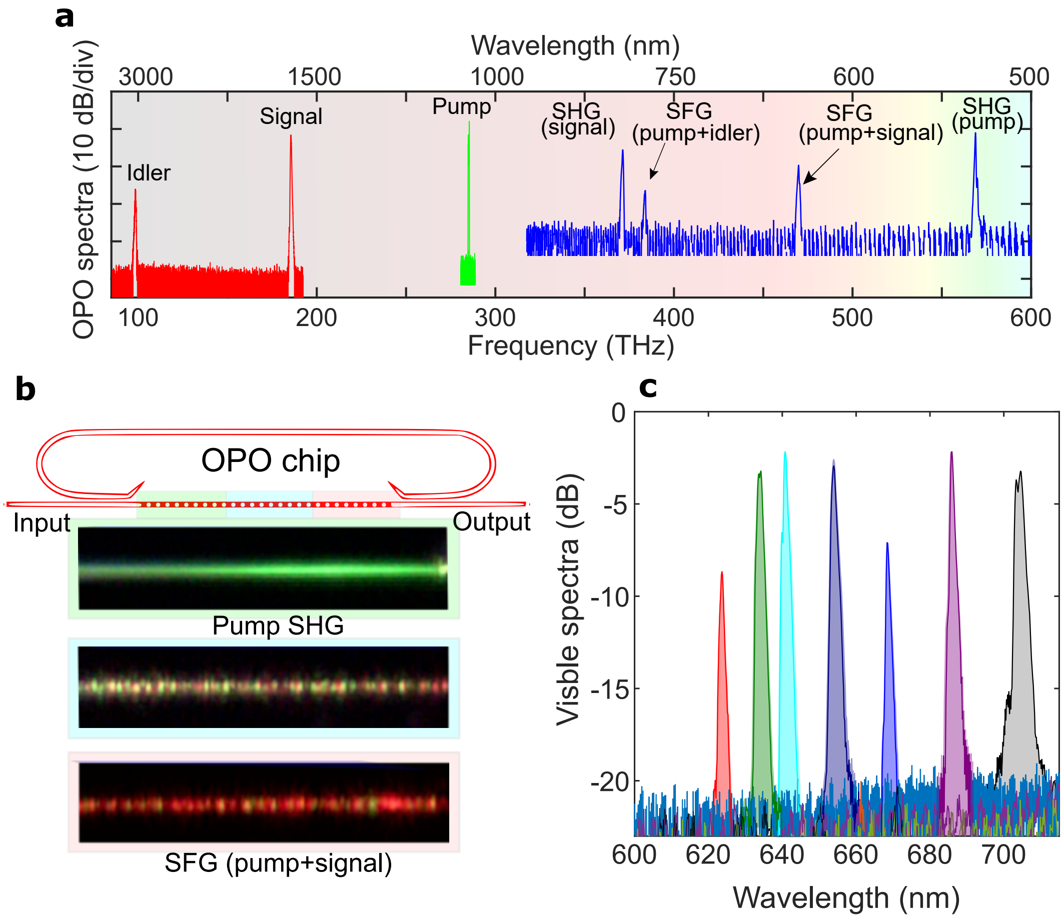

Figure 6.7: **Visible frequency comb generation from integrated optical parametric oscillators. a**, Example of the complete emission spectrum of an OPO by stitching together spectra obtained from different optical spectrum analyzers and spectrometers. Apart from the emission of the signal and the idler waves, the OPO also produces output in the visible spectra owing to the auxiliary nonlinear processes namely the second- harmonic generation (SHG) and the sum-frequency generation (SFG). **b**, Optical microscope image capturing the visible light emission from various regions of the periodically poled section of the OPO device **c**, Tunable visible frequency comb generation from the integrated OPO chip, where different colors indicate spectra obtained from OPOs with distinct poling periods.

6.2 Discussion

The pump, which is a near-IR electro-optic comb, can be incorporated into the lithium niobate chip in the future [40], [41]. With proper dispersion engineering, our OPO design can additionally achieve large instantaneous bandwidth accompanied by significant pulse compression [42], enabling the generation of femtosecond mid-infrared frequency combs in nanophotonics. Efficient supercontinuum generation requiring only a couple of picojoules of pulse energy can then be performed using periodically-poled lithium niobate waveguides on these femtosecond pulses for subsequent f-2f self-referencing/comb stabilization [43]. Future work will involve the integration of electro-optic modulators for active locking of the OPO frequency comb. The on-chip OPO threshold can be reduced further by improving waveguide losses and enhancing the effective nonlinear co-efficient by separately optimizing the modal overlap between the pump and the signal/idler fields for each OPO device catering to dedicated spectral bands. We estimate that an on-chip threshold for operation near degeneracy with an average power less than 500 μW (for 10 GHz repetition rate operation) is feasible. The low power requirement combined with the need for a relatively narrow pump tunability range opens the door for pumping the OPO chip with butt-coupled near-infrared diode lasers, similar to what we show in the next chapter. This paves the way for a fully integrated solution for mid-IR frequency comb generation based on lithium niobate nanophotonics [30], [31], [44], [45].

We envision a complete integrated solution for frequency comb generation based on lithium niobate nanophotonics in conjunction with a laser chip. With several design enhancements, it is possible to lower the threshold for frequency comb generation substantially which can allow the pumping with commercially available DFB laser chips. Alternatively, an integrated external cavity along with a semiconductor gain chip can also be deployed for this purpose [46]. The other crucial building blocks are: a) near-IR picosecond pump pulse generation [30], [31], b) Mach Zehnder interferometer mesh for routing the pump light to the desired OPO [47], c) an array of OPOs, and d) periodically poled lithium niobate waveguides supporting ultralow power supercontinuum generation for f-2f based frequency comb stabilization [48]. Our present work focuses on part c, while the rest has already been demonstrated in lithium-niobate nanophotonics.

Similar observations to those made on Chapter 5 regarding the coupler design are valid here as well. In particular, optimizing the coupler design can enable OPO operation with lower thresholds and higher mid-infrared comb conversion efficiency. Advanced coupler designs like the ones inspired by inverse design [49] can satisfy the simultaneous requirements of low coupling for the pump, high coupling for the signal, and optimum coupling for the idler waves, leading to conversion efficiencies even exceeding 30 %. Realizing OPO devices in lithium niobate on sapphire will give access to a wider transparency window, leading to frequency comb generation deeper into the mid-infrared [50]. Thanks to the strong parametric nonlinear interaction, it is possible to realize frequency combs with lower repetition rates (~1 GHz) using spiral waveguides [51] in the feedback arm of the OPO resonator which will be useful for on-chip dual-comb spectroscopy applications. The emission in the mid-infrared overlaps with important molecular rovibrational absorption lines and paves the way for novel integrated spectroscopic solutions.

References

[1] A. Roy, L. Ledezma, L. Costa, R. Gray, R. Sekine, Q. Guo, M. Liu, R. M. Briggs, and A. Marandi, "Visible-to-mid-IR tunable frequency comb in nanophotonics," *arXiv*, Dec. 2022. DOI: `10.48550/arXiv.2212.08723`.

[2] S. A. Diddams, K. Vahala, and T. Udem, "Optical frequency combs: Coherently uniting the electromagnetic spectrum," *Science*, vol. 369, no. 6501, eaay3676, 2020.

[3] T. J. Kippenberg, A. L. Gaeta, M. Lipson, and M. L. Gorodetsky, "Dissipative kerr solitons in optical microresonators," *Science*, vol. 361, no. 6402, eaan8083, 2018.

[4] I. Coddington, N. Newbury, and W. Swann, "Dual-comb spectroscopy," *Optica*, vol. 3, no. 4, pp. 414–426, 2016.

[5] P. Marin-Palomo, J. N. Kemal, M. Karpov, A. Kordts, J. Pfeifle, M. H. Pfeiffer, P. Trocha, S. Wolf, V. Brasch, M. H. Anderson, *et al.*, "Microresonator-based solitons for massively parallel coherent optical communications," *Nature*, vol. 546, no. 7657, pp. 274–279, 2017.

[6] X. Xu, M. Tan, B. Corcoran, J. Wu, A. Boes, T. G. Nguyen, S. T. Chu, B. E. Little, D. G. Hicks, R. Morandotti, *et al.*, "11 tops photonic convolutional accelerator for optical neural networks," *Nature*, vol. 589, no. 7840, pp. 44–51, 2021.

[7] L. Stern, J. R. Stone, S. Kang, D. C. Cole, M.-G. Suh, C. Fredrick, Z. Newman, K. Vahala, J. Kitching, S. A. Diddams, *et al.*, "Direct kerr frequency comb atomic spectroscopy and stabilization," *Science Advances*, vol. 6, no. 9, eaax6230, 2020.

[8] M.-G. Suh and K. J. Vahala, "Soliton microcomb range measurement," *Science*, vol. 359, no. 6378, pp. 884–887, 2018.

[9] P. Trocha, M. Karpov, D. Ganin, M. H. Pfeiffer, A. Kordts, S. Wolf, J. Krockenberger, P. Marin-Palomo, C. Weimann, S. Randel, *et al.*, "Ultrafast optical ranging using microresonator soliton frequency combs," *Science*, vol. 359, no. 6378, pp. 887–891, 2018.

[10] X. Ji, X. Yao, A. Klenner, Y. Gan, A. L. Gaeta, C. P. Hendon, and M. Lipson, "Chip-based frequency comb sources for optical coherence tomography," *Optics Express*, vol. 27, no. 14, pp. 19 896–19 905, 2019.

[11] M. Ebrahim-Zadeh and I. T. Sorokina, *Mid-infrared coherent sources and applications*. Springer Science & Business Media, 2007.

[12] A. Schliesser, N. Picqué, and T. W. Hänsch, "Mid-infrared frequency combs," *Nature Photonics*, vol. 6, no. 7, pp. 440–449, 2012.

[13] E. Obrzud, M. Rainer, A. Harutyunyan, M. H. Anderson, J. Liu, M. Geiselmann, B. Chazelas, S. Kundermann, S. Lecomte, M. Cecconi, *et al.*, "A microphotonic astrocomb," *Nature Photonics*, vol. 13, no. 1, pp. 31–35, 2019.

[14] M.-G. Suh, X. Yi, Y.-H. Lai, S. Leifer, I. S. Grudinin, G. Vasisht, E. C. Martin, M. P. Fitzgerald, G. Doppmann, J. Wang, *et al.*, "Searching for exoplanets using a microresonator astrocomb," *Nature Photonics*, vol. 13, no. 1, pp. 25–30, 2019.

[15] B. Stern, X. Ji, Y. Okawachi, A. L. Gaeta, and M. Lipson, "Battery-operated integrated frequency comb generator," *Nature*, vol. 562, no. 7727, pp. 401–405, 2018.

[16] H. Guo, C. Herkommer, A. Billat, D. Grassani, C. Zhang, M. H. Pfeiffer, W. Weng, C.-S. Bres, and T. J. Kippenberg, "Mid-infrared frequency comb via coherent dispersive wave generation in silicon nitride nanophotonic waveguides," *Nature Photonics*, vol. 12, no. 6, pp. 330–335, 2018.

[17] A. S. Kowligy, D. R. Carlson, D. D. Hickstein, H. Timmers, A. J. Lind, P. G. Schunemann, S. B. Papp, and S. A. Diddams, "Mid-infrared frequency combs at 10 ghz," *Optics Letters*, vol. 45, no. 13, pp. 3677–3680, 2020.

[18] A. Hugi, G. Villares, S. Blaser, H. Liu, and J. Faist, "Mid-infrared frequency comb based on a quantum cascade laser," *Nature*, vol. 492, no. 7428, pp. 229–233, 2012.

[19] C. Y. Wang, L. Kuznetsova, V. Gkortsas, L. Diehl, F. X. Kaertner, M. A. Belkin, A. Belyanin, X. Li, D. Ham, H. Schneider, *et al.*, "Mode-locked pulses from mid-infrared quantum cascade lasers," *Optics Express*, vol. 17, no. 15, pp. 12 929–12 943, 2009.

[20] Y. Yao, A. J. Hoffman, and C. F. Gmachl, "Mid-infrared quantum cascade lasers," *Nature Photonics*, vol. 6, no. 7, pp. 432–439, 2012.

[21] A. G. Griffith, R. K. Lau, J. Cardenas, Y. Okawachi, A. Mohanty, R. Fain, Y. H. D. Lee, M. Yu, C. T. Phare, C. B. Poitras, *et al.*, "Silicon-chip mid-infrared frequency comb generation," *Nature Communications*, vol. 6, no. 1, pp. 1–5, 2015.

[22] A. A. Savchenkov, V. S. Ilchenko, F. Di Teodoro, P. M. Belden, W. T. Lotshaw, A. B. Matsko, and L. Maleki, "Generation of kerr combs centered at 4.5 μm in crystalline microresonators pumped with quantum-cascade lasers," *Optics Letters*, vol. 40, no. 15, pp. 3468–3471, 2015.

[23] M. Yu, Y. Okawachi, A. G. Griffith, M. Lipson, and A. L. Gaeta, "Mode-locked mid-infrared frequency combs in a silicon microresonator," *Optica*, vol. 3, no. 8, pp. 854–860, 2016.

[24] Y. Tang, L. G. Wright, K. Charan, T. Wang, C. Xu, and F. W. Wise, "Generation of intense 100 fs solitons tunable from 2 to 4.3 μm in fluoride fiber," *Optica*, vol. 3, no. 9, pp. 948–951, 2016.

[25] F. Adler, K. C. Cossel, M. J. Thorpe, I. Hartl, M. E. Fermann, and J. Ye, "Phase-stabilized, 1.5 w frequency comb at 2.8–4.8 μm," *Optics Letters*, vol. 34, no. 9, pp. 1330–1332, 2009.

[26] L. Maidment, P. G. Schunemann, and D. T. Reid, "Molecular fingerprint-region spectroscopy from 5 to 12 μm using an orientation-patterned gallium phosphide optical parametric oscillator," *Optics Letters*, vol. 41, no. 18, pp. 4261–4264, 2016.

[27] A. W. Bruch, X. Liu, Z. Gong, J. B. Surya, M. Li, C.-L. Zou, and H. X. Tang, "Pockels soliton microcomb," *Nature Photonics*, vol. 15, no. 1, pp. 21–27, 2021.

[28] Y. He, Q.-F. Yang, J. Ling, R. Luo, H. Liang, M. Li, B. Shen, H. Wang, K. Vahala, and Q. Lin, "Self-starting bi-chromatic linbo 3 soliton microcomb," *Optica*, vol. 6, no. 9, pp. 1138–1144, 2019.

[29] J. Lu, A. A. Sayem, Z. Gong, J. B. Surya, C.-L. Zou, and H. X. Tang, "Ultralow-threshold thin-film lithium niobate optical parametric oscillator," *Optica*, vol. 8, no. 4, pp. 539–544, Apr. 2021, ISSN: 2334-2536. DOI: `10.1364/OPTICA.418984`.

[30] Y. Hu, M. Yu, B. Buscaino, N. Sinclair, D. Zhu, R. Cheng, A. Shams-Ansari, L. Shao, M. Zhang, J. M. Kahn, *et al.*, "High-efficiency and broadband on-chip electro-optic frequency comb generators," *Nature Photonics*, vol. 16, no. 10, pp. 679–685, 2022.

[31] M. Yu, C. Reimer, D. Barton, P. Kharel, R. Cheng, L. He, L. Shao, D. Zhu, Y. Hu, H. R. Grant, *et al.*, "Femtosecond pulse generation via an integrated electro-optic time lens," *arXiv preprint arXiv:2112.09204*, 2021.

[32] M. Zhang, B. Buscaino, C. Wang, A. Shams-Ansari, C. Reimer, R. Zhu, J. M. Kahn, and M. Lončar, "Broadband electro-optic frequency comb generation in a lithium niobate microring resonator," *Nature*, vol. 568, no. 7752, pp. 373–377, Apr. 2019, ISSN: 1476-4687. DOI: `10.1038/s41586-019-1008-7`.

[33] X. Lu, G. Moille, A. Rao, D. A. Westly, and K. Srinivasan, "On-chip optical parametric oscillation into the visible: Generating red, orange, yellow, and green from a near-infrared pump," *Optica*, vol. 7, no. 10, pp. 1417–1425, 2020.

[34] J. Li, C. Bao, Q.-X. Ji, H. Wang, L. Wu, S. Leifer, C. Beichman, and K. Vahala, "Efficiency of pulse pumped soliton microcombs," *Optica*, vol. 9, no. 2, pp. 231–239, 2022.

[35] E. Obrzud, S. Lecomte, and T. Herr, "Temporal solitons in microresonators driven by optical pulses," *Nature Photonics*, vol. 11, no. 9, pp. 600–607, 2017.

[36] A. Roy, S. Jahani, C. Langrock, M. Fejer, and A. Marandi, "Spectral phase transitions in optical parametric oscillators," *Nature Communications*, vol. 12, no. 1, pp. 1–9, 2021.

[37] A. J. Metcalf, A. J. Metcalf, A. J. Metcalf, C. D. Fredrick, C. D. Fredrick, R. C. Terrien, R. C. Terrien, S. B. Papp, S. B. Papp, S. A. Diddams, S. A. Diddams, and S. A. Diddams, "30 GHz electro-optic frequency comb spanning 300 THz in the near infrared and visible," *Optics Letters*, vol. 44, no. 11, pp. 2673–2676, Jun. 2019, ISSN: 1539-4794. DOI: `10.1364/OL.44.002673`.

[38] A. Parriaux, K. Hammani, and G. Millot, "Electro-optic frequency combs," *Advances in Optics and Photonics*, vol. 12, no. 1, pp. 223–287, 2020.

[39] P. A. Verrinder, L. Wang, J. Fridlander, F. Sang, V. Rosborough, M. Nickerson, G. Yang, M. Stephen, L. Coldren, and J. Klamkin, "Gallium arsenide photonic integrated circuit platform for tunable laser applications," *IEEE Journal of Selected Topics in Quantum Electronics*, vol. 28, no. 1, pp. 1–9, 2021.

[40] C. O. de Beeck, F. M. Mayor, S. Cuyvers, S. Poelman, J. F. Herrmann, O. Atalar, T. P. McKenna, B. Haq, W. Jiang, J. D. Witmer, G. Roelkens, A. H. Safavi-Naeini, R. V. Laer, and B. Kuyken, "III/V-on-lithium niobate amplifiers and lasers," *Optica*, vol. 8, no. 10, pp. 1288–1289, Oct. 2021, ISSN: 2334-2536. DOI: `10.1364/OPTICA.438620`.

[41] M. Zhang, B. Buscaino, C. Wang, A. Shams-Ansari, C. Reimer, R. Zhu, J. M. Kahn, and M. Lončar, "Broadband electro-optic frequency comb generation in a lithium niobate microring resonator," *Nature*, vol. 568, no. 7752, pp. 373–377, 2019.

[42] A. Roy, R. Nehra, S. Jahani, L. Ledezma, C. Langrock, M. Fejer, and A. Marandi, "Temporal walk-off induced dissipative quadratic solitons," *Nature Photonics*, vol. 16, no. 2, pp. 162–168, 2022.

[43] M. Jankowski, C. Langrock, B. Desiatov, A. Marandi, C. Wang, M. Zhang, C. R. Phillips, M. Lončar, and M. Fejer, "Ultrabroadband nonlinear optics in nanophotonic periodically poled lithium niobate waveguides," *Optica*, vol. 7, no. 1, pp. 40–46, 2020.

[44] Q. Guo, R. Sekine, L. Ledezma, R. Nehra, D. J. Dean, A. Roy, R. M. Gray, S. Jahani, and A. Marandi, "Femtojoule femtosecond all-optical switching in lithium niobate nanophotonics," *Nature Photonics*, vol. 16, no. 9, pp. 625–631, 2022.

[45] L. Ledezma, R. Sekine, Q. Guo, R. Nehra, S. Jahani, and A. Marandi, "Intense optical parametric amplification in dispersion-engineered nanophotonic lithium niobate waveguides," *Optica*, vol. 9, no. 3, pp. 303–308, 2022.

[46] M. Li, L. Chang, L. Wu, J. Staffa, J. Ling, U. A. Javid, S. Xue, Y. He, R. Lopez-rios, T. J. Morin, H. Wang, B. Shen, S. Zeng, L. Zhu, K. J. Vahala, J. E. Bowers, and Q. Lin, "Integrated Pockels laser," *Nature Communications*, vol. 13, no. 1, p. 5344, Sep. 2022, ISSN: 2041-1723. DOI: `10.1038/s41467-022-33101-6`.

[47] C. Wang, M. Zhang, X. Chen, M. Bertrand, A. Shams-Ansari, S. Chandrasekhar, P. Winzer, and M. Lončar, "Integrated lithium niobate electro-optic modulators operating at CMOS-compatible voltages," *Nature*, vol. 562, no. 7725, p. 101, Oct. 2018, ISSN: 1476-4687. DOI: `10.1038/s41586-018-0551-y`.

[48] M. Jankowski, C. Langrock, B. Desiatov, A. Marandi, C. Wang, M. Zhang, C. R. Phillips, M. Lončar, and M. M. Fejer, "Ultrabroadband nonlinear optics in nanophotonic periodically poled lithium niobate waveguides," *Optica*, vol. 7, no. 1, pp. 40–46, Jan. 2020, ISSN: 2334-2536. DOI: `10.1364/OPTICA.7.000040`.

[49] S. Molesky, Z. Lin, A. Y. Piggott, W. Jin, J. Vucković, and A. W. Rodriguez, "Inverse design in nanophotonics," *Nature Photonics*, vol. 12, no. 11, pp. 659–670, 2018.

[50] J. Mishra, T. P. McKenna, E. Ng, H. S. Stokowski, M. Jankowski, C. Langrock, D. Heydari, H. Mabuchi, M. Fejer, and A. H. Safavi-Naeini, "Mid-infrared nonlinear optics in thin-film lithium niobate on sapphire," *Optica*, vol. 8, no. 6, pp. 921–924, 2021.

[51] H. Lee, T. Chen, J. Li, O. Painter, and K. J. Vahala, "Ultra-low-loss optical delay line on a silicon chip," *Nature Communications*, vol. 3, no. 1, pp. 1–7, 2012.

Chapter 7

LASER DIODE PUMPED OPTICAL PARAMETRIC OSCILLATOR

The results from previous chapters showcase the remarkable performance of compact on-chip OPOs in terms of efficiency and tunability. However, those OPOs were still driven by large and expensive pulsed pumps based on tunable external cavity lasers. While we can argue that external cavity lasers and electro-optic frequency combs have been already demonstrated on thin film lithium niobate [1], [2], it still remains an important milestone to demonstrate experimentally that our on-chip OPOs can be driven by compact, inexpensive pump lasers. In this chapter, we reach this milestone and demonstrate an on-chip OPO that can be driven directly by a commercial laser diode (Photodigm Inc. [3]). Furthermore, this OPO operates in the CW regime, opening the door for applications requiring high temporal coherence. We also show that the OPO can oscillate for long periods of time, even in the absence of active locking mechanisms. This represents, to the best of my knowledge, the first $\chi^{(2)}$ OPO directly pumped by a commercial and compact semiconductor laser diode, without the use of additional components like amplifiers or isolators.

There are several challenges associated with driving our on-chip OPOs directly by small lasers. The most urgent one is the large coupling loss exhibited by our previous OPOs, which typically exceeded 10 dB when coupling from free-space to on-chip waveguides. As an example, our OPO from Chapter 5 had a peak power threshold of ~30 mW, which would translate to more than 300 mW of off-chip CW power if we kept the same coupling loss, and this is just enough to reach threshold! However, the situation is much better than it seems. As argued in Chapter 5, the large input coupling loss is a linear problem that can be solved by optimizing the mode overlap between the incoming pump beam and the nanophotonic waveguide. In this chapter, we perform such optimization for the case in which the pump is a compact semiconductor laser diode.

A second challenge is that laser diodes are susceptible to optical feedback [4]. Directly butt-coupling a laser diode to a nanophotonic chip would provide back-reflections at every interface, leading to potential instabilities. In the worst case scenario, a compact semiconductor laser diode may become useless when coupled

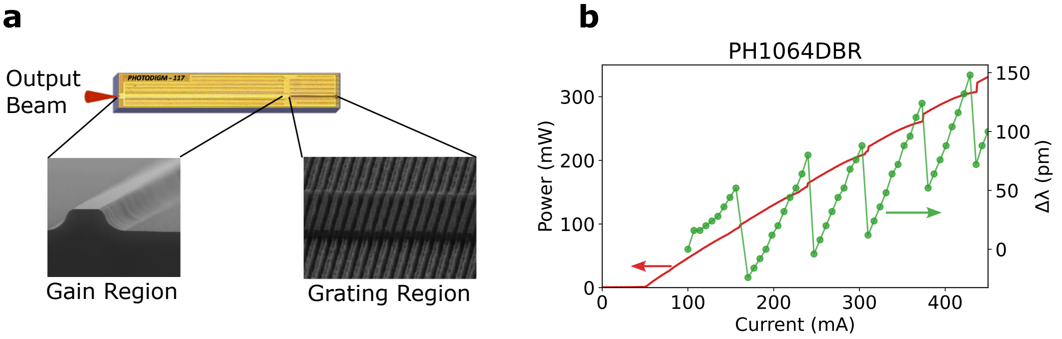

Figure 7.1: **Distributed Bragg reflector lasers.** **a**, A Bragg grating at the back of the device works as a wavelength selective mirror providing large feedback over a narrowband wavelength range. The cleaved output facet at the front of the device also functions as the other end of the laser cavity. A ridge waveguide, consisting of a layered structure with one or more high refractive index quantum wells, runs between the front cleaved facet and the Bragg mirror. Images by JESpencer - Own work, CC BY-SA 4.0, `https://commons.wikimedia.org/w/index.php?curid=34983533`. **b**, Power and wavelength variation ($\Delta\lambda = \lambda - \lambda_0$) as a function of injection current for the DBR used to pump our OPOs. As the injection current increases, the wavelength monotonically red-shifts in between blue-shift mode hops. Data courtesy of Photodigm, Inc.

to our chips. Indeed, previous efforts to pump table-top $\chi^{(2)}$ OPOs with laser diodes have required using bulky isolators [5], [6] that are not compatible with integrated photonics. We also tackle this issue in this chapter, and experimentally show that the main problem comes from reflections at the *output facet* of our chips, and that by decreasing those reflections, the stability of the diode laser can be improved enough to produce stable optical parametric oscillation for tens of minutes without any active locking system.

7.1 Distributed Bragg reflector lasers

A distributed Bragg reflector (DBR) laser consists of a single spatial mode waveguide with a gain region and a passive Bragg grating region (Fig. 7.1a). The gain region has multiple epitaxial layers forming one or more quantum wells that are electrically pumped through current injection. The Bragg grating region forms one end of the laser cavity providing a high reflection within a narrow spectral bandwidth. The other end of the laser cavity is provided by a cleaved facet that typically includes an anti-reflection coating and serves as the output of the laser. The output beam is usually nearly diffraction limited [3].

The output wavelength of a DBR laser changes with output power and injection current as shown in Fig. 7.1b for the commercial DBR we use to pump our OPOs (PH1064DBR - Photodigm Inc. [3]). As the injection current is increased, the temperature of the gain region raises causing thermal expansion and a corresponding red-shift of the output wavelength. The temperature of the Bragg region does not vary significantly with injection current into the gain region. Therefore, the DBR reflectivity bandwidth is mainly a function of the global device temperature and not the injection current. After the output mode has red-shifted a certain amount due to the temperature increase, another mode will be favored by the combination of gain and reflectivity and a blue-shift mode-hop will occur. This mode hop will be typically equal to a single free spectral range of the laser cavity. For instance, Fig. 7.1b shows blue shift mode hops of ~20 GHz, corresponding to a cavity length ~1.5 mm. In principle, this tuning behavior allows for a monotonic increase in the output power at a fixed wavelength by careful control of the device temperature.

7.2 Input coupling optimization

The commercial DBR laser provides a diffraction-limited beam with divergence angles, at full-width-half-maximum (FWHM) power, of $\Theta_x = 6°$ for the horizontal direction and $\Theta_y = 28°$ for the vertical direction. This corresponds to a cylindrical Gaussian beam, with horizontal and vertical waists of $w_x = \lambda\sqrt{2\ln 2}/\pi/\Theta_x = 3.81\ \mu\text{m}$, and $w_y = \lambda\sqrt{2\ln 2}/\pi/\Theta_y = 0.82\ \mu\text{m}$, at $\lambda = 1064$ nm. This estimated mode is illustrated in Fig. 7.2.

The power coupling coefficient between the laser and the TFLN waveguide can be written as $\gamma = \gamma_R\gamma_O$, where γ_R is the Fresnel power transmission coefficient and γ_O is a modal overlap integral. For simplicity, we are ignoring any potential air gap between the DBR facet and the TFLN chip facet. Assuming that the waveguide facets are orthogonal to the propagation direction, the Fresnel transmission coefficient due to effective index differences between both waveguides is simply

$$\gamma_R = 1 - \left|\frac{n_{\text{LN}} - n_{\text{DBR}}}{n_{\text{LN}} + n_{\text{DBR}}}\right|^2, \tag{7.1}$$

where n_{LN} and n_{DBR} are the effective indexes of the TFLN and DBR waveguides. We assume $n_{\text{DBR}} \approx 3.32$ for the AlGaAs DBR waveguide [7], leading to $\gamma_R \approx 95\%$.

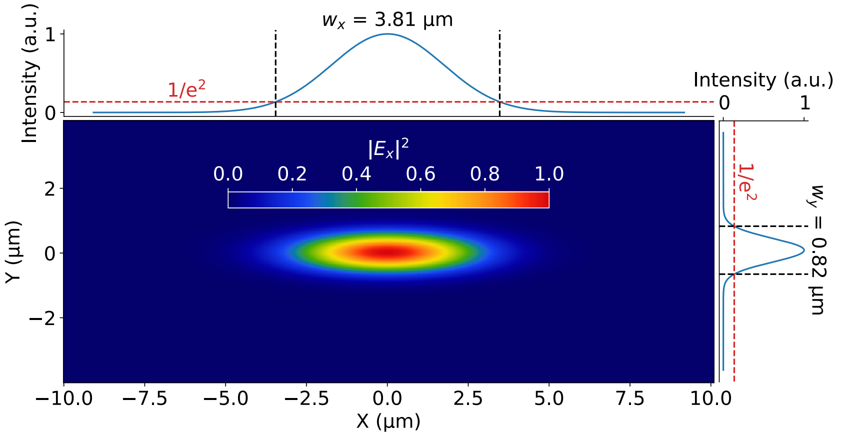

Figure 7.2: **Estimated mode shape at the output facet of commercially available DBR laser.** The manufacturer provided full-width-half-maximum divergence angles (6° for the horizontal and 28° for the vertical directions) were used to model the DBR output as a single mode elliptical beam with 3.81 μm and 0.82 μm waists.

The modal overlap γ_O is given by [8],

$$\gamma_O = \frac{\left(\int \mathbf{E}_{\mathrm{LN}} \times \mathbf{H}^*_{\mathrm{DBR}} \cdot \mathrm{d}\mathbf{S}\right)\left(\int \mathbf{E}_{\mathrm{DBR}} \times \mathbf{H}^*_{\mathrm{WG}} \cdot \mathrm{d}\mathbf{S}\right)}{\left(\int \mathbf{E}_{\mathrm{LN}} \times \mathbf{H}^*_{\mathrm{LN}} \cdot \mathrm{d}\mathbf{S}\right)\left(\int \mathbf{E}_{\mathrm{DBR}} \times \mathbf{H}^*_{\mathrm{DBR}} \cdot \mathrm{d}\mathbf{S}\right)}, \tag{7.2}$$

and it is real for lossless waveguides. The result of this overlap integral, as a function of the TFLN waveguide width, is shown in the dashed black trace of Fig. 7.3. Also shown is the total power coupling efficiency $\gamma = \gamma_R\gamma_O$ (continuous red trace). We choose our waveguides to be 10-μm wide at the facet, where this analysis shows a coupling efficiency close to 65%. A 100-μm-long adiabatic taper is used to transform the input 10-μm-wide waveguide into the 2.7-μm-wide waveguide at the input coupler of the OPO. The rest of the OPO design follows that described in Chapter 5.

7.3 Back-reflection minimization

All types of laser diodes are susceptible to external optical feedback [4], [9]. The effect can vary from unstable behavior and frequent mode hops, to line broadening or narrowing effects. In our case, the two major sources of optical feedback to the pump laser come from the two OPO chip facets (see Fig. 7.4). We can broadly understand the effect of each facet as follows. The input facet is in close proximity to the DBR laser facet, hence its main effect is to provide a reflection coefficient $R_i = |R_i|\exp(i\phi_i)$, while producing minimal changes on the free spectral range of the laser. The magnitude of the reflection $|R_i|$ can cause changes in the threshold

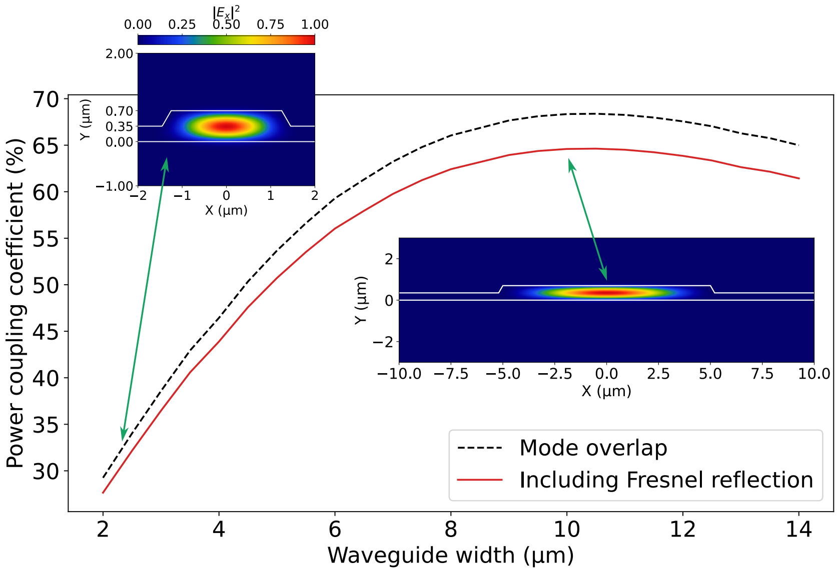

Figure 7.3: **Estimated power coupling efficiency from diode laser to TFLN chip.** Shown as a function of the TFLN waveguide width. The dashed black trace is the result of an overlap integral between the DBR mode from Fig. 7.2 and the mode of the TFLN waveguide. The continuous red trace also includes the effect of back reflections due to the difference in effective indexes between the waveguides (assuming $n_{\text{eff}} \approx 3.5$ for the DBR waveguide). Insets show TFLN mode profiles for 2.5 μm and 10 μm width.

and linewidth of the laser output, but will not change the number of spectral modes going above threshold. In contrast, the larger cavity formed with the output facet of the OPO chip can significantly reduce the free-spectral range of the laser allowing several modes to experience significant gain and go above threshold.

A more rigorous analysis can be made that includes the back-action of laser frequency on threshold gain and effective index [4]. This leads to a change in roundtrip phase (modulo 2π) of

$$\Delta\phi = (\omega - \omega_0)\tau_L + \kappa_e\sqrt{1+\alpha^2}\sin(\omega\tau_e + \arctan\alpha), \tag{7.3}$$

where ω_0 is the oscillation frequency without external feedback, κ_e is a constant that depends on the ratio of the external cavity reflection and the DBR laser reflection without external feedback, and α is the phase-amplitude coupling parameter from semiconductor laser theory [10]. A plot of $\Delta\phi$ is shown in Fig. 7.4 for the cases of no-feedback (dashed line), short external cavity feedback ($\tau_e << \tau_L$), and long external cavity feedback ($\tau_e >> \tau_L$). The zero crossings indicate modes that will satisfy the positive feedback roundtrip condition.

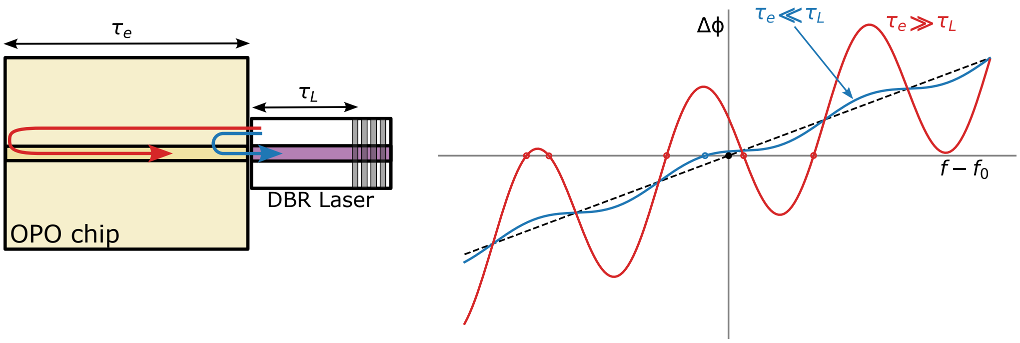

Figure 7.4: **Effect of optical feedback on semiconductor lasers.** Two major sources of feedback are the input and output facets of the OPO chip. The number of modes that can satisfy constructive interference ($\Delta\phi = 0$) depends on the relative size of the DBR laser cavity roundtrip delay (τ_L), compared to the roundtrip delay of the external cavity formed by the OPO chip (τ_e).

This theoretical analysis suggests that reflection from the output facet could play an important role on the stability of the DBR laser. In Fig. 7.5a we show the measured spectra of the DBR laser diode as the injection current is swept and after going through a test waveguide on the OPO chip. A discontinuous tuning with frequent mode hops is observed, including regions of multimode operation. Fig. 7.5b shows the same measurement repeated after polishing the output facet at a 7° angle in order to reduce the magnitude of the reflections. The tuning is now monotonic except for the expected ~20 GHz blue shift mode hops. Future chips will have an output waveguide that meets the facet at an angle of at least 7°.

7.4 Free-running OPO results

An image of the OPO chip in the test setup along with the DBR laser is shown in Fig. 7.6a. The OPO chip sits on a thermoelectric cooler (TEC) and we use a cleaved multimode fiber to collect the output. There are 17 OPOs on this single chip, and the red dashed line in Fig. 7.6a highlights a single ~7-mm-long and ~0.5-mm-wide OPO. Figures 7.6b,c show a close-up image of the DBR laser in close contact with the OPO input waveguide. When the laser is above threshold, scattered 1 μm light is detected by the camera.

The OPO goes above threshold at ~120 mA, which corresponds to ~50 mW according to the DBR laser datasheet (see Fig. 7.1b). As the current is increased, several oscillation peaks are observed on a 2 μm photodetector. The peaks are expected as the DBR laser wavelength is also changing when the current increases so different

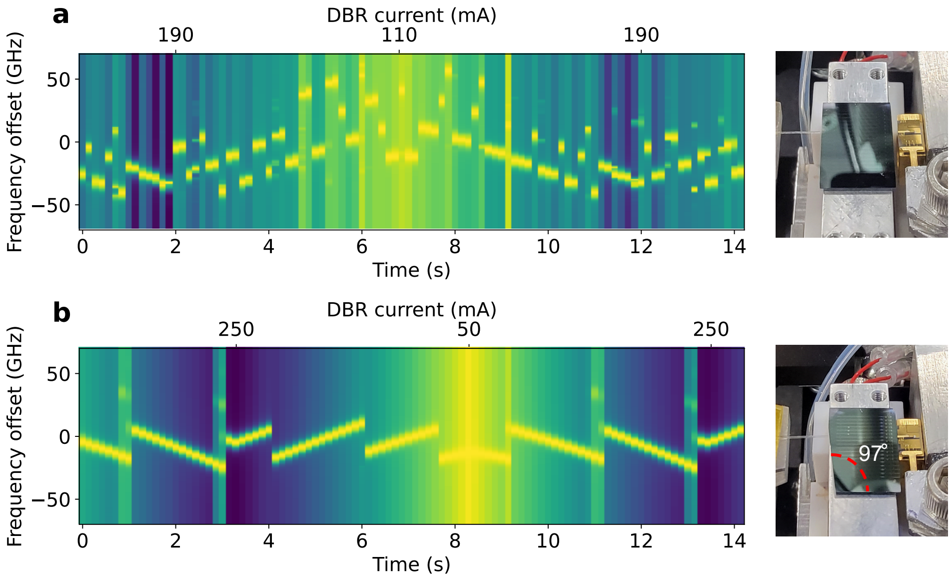

Figure 7.5: **DBR laser frequency as a function of injection current with optical feedback.** **a**, DBR laser frequency as the current is modulated by a triangular waveform from 110 mA to 190 mA. The output is unstable with multiple mode-hops in distinct directions as the current changes. **b**, After reducing the optical feedback by polishing the output facet at a 7° angle, the DBR laser frequency is stable, varying in a predictable way and with the expected blue-shifted mode hops.

signal/idler pairs go into and out of resonance. Figure 7.7a shows examples of three different spectra for operation at roughly three times above threshold. As was the case of the quasi-CW OPO of Chapter 5, this OPO can operate in a single mode signal/idler pair (middle panel in 7.7a), or in multimode regimes (top and bottom panels in 7.7a). The close-up shown in Fig. 7.7b has enough spectral resolution to reveal the resonator modes with ~9.5 GHz free spectral range. This on-chip OPO shows a remarkable advantage with respect to table-top implementations by oscillating continuously for more than 30 minutes, without mode hops, and without the use of any stabilization or locking techniques (Fig. 7.7c).

7.5 Discussion and outlook

The results shown in this chapter already show the feasibility of having a compact laser source capable of replacing several individual laser diodes, which was the main motivation outline in the introduction of this thesis. However, there are several remaining issues that must be addressed. The tuning range shown here, although sufficient for many applications, can be extended by using a diode pump that can be tuned over more than 10 nm. Indeed, there are already efforts underway to produce

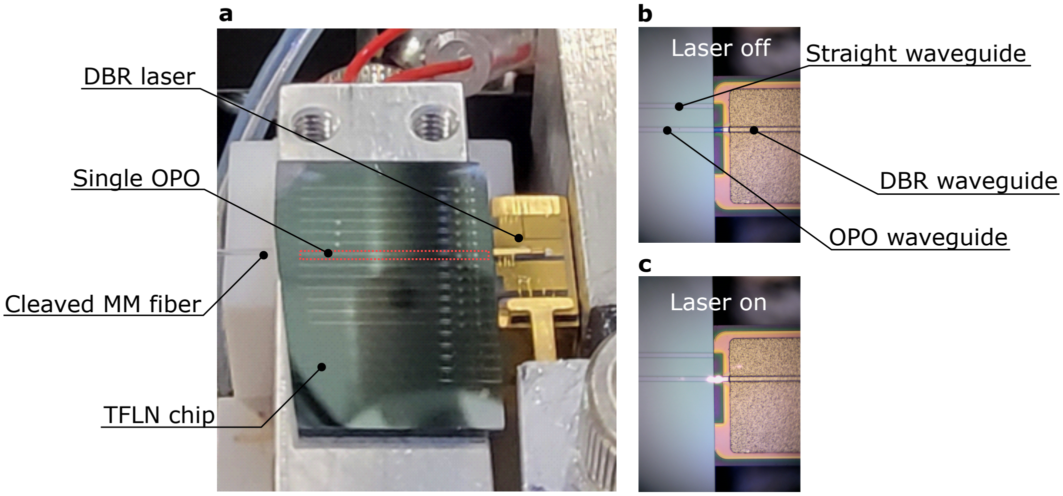

Figure 7.6: **OPO chip coupled to a DBR laser diode.** **a**, Image of OPO chip on test setup, with DBR laser and output cleaved multimode fiber also visible. The dashed rectangle delineates a single OPO on the chip. **b**, Close-up image of the DBR laser in close-contact with the TFLN chip. Two waveguides are visible on the TFLN chip, one is the input to the OPO and the other is a straight waveguide for testing purposes. **c**, Close-up image with the laser diode above threshold. The camera can detect the scattered near-IR light at the interface between the laser and the TFLN chip.

tunable semiconductor lasers based on sampled grating DBR (SGDBR) designs, which include a gain section, a phase section, and front and back SGDBR mirrors [11]. Preliminary results show tuning ranges of more than 30 nm around a 1030 nm wavelength [12].

Another promising alternative is to harness the optical feedback from the TFLN chip to produce a tunable pump starting from a semiconductor gain chip [1]. Such pump can be integrated on the same chip as the OPO, it might be tunable over the entire semiconductor gain bandwidth, and it also inherently solves any issues related to optical feedback instabilities.

Continuous tuning of the OPO outputs may require a complex algorithm in order to exploit the interplay between all the tuning variables in a doubly-resonant OPO. An alternative would be to start developing singly-resonant OPOs if all the trade-offs among threshold, tunability, and output power turn out to be benefitial. This may be the case for pulsed applications.

Applications requiring single spectral modes with high coherence would need modifying the OPO design. For instance, an additional resonator can be added in other

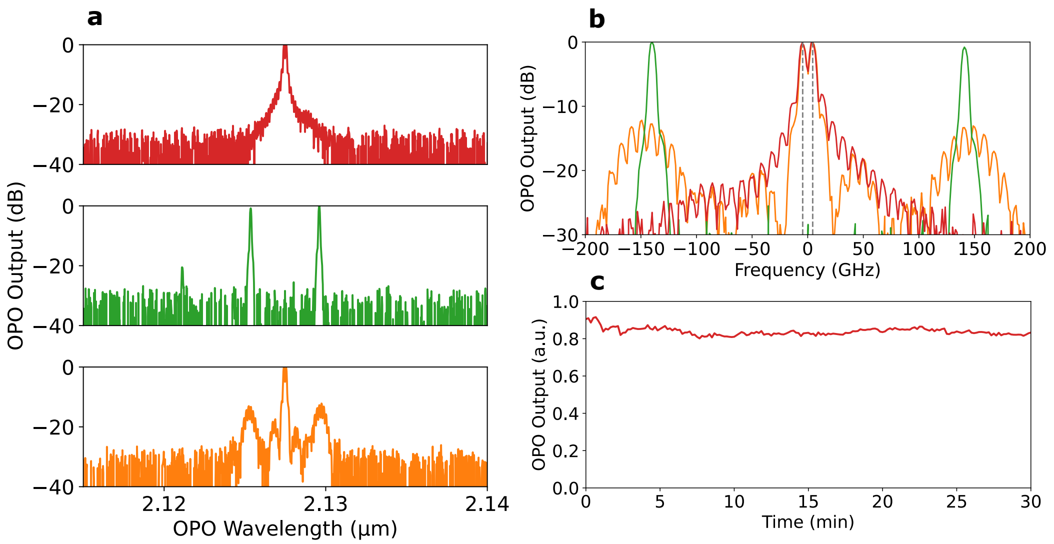

Figure 7.7: **Spectra of free-running CW OPO driven by DBR laser diode.** **a**, Example output spectra for slightly different pump wavelengths around ~1063.7 nm, at a DBR injection current of 241 mA corresponding to ~160 mW. **b**, Close-up of the three spectra a function of frequency. The resolution bandwidth of the optical spectrum analyzer was set to ~3.4 GHz, so different resonator modes are distinguishable. The mid-trace (green) corresponds to a signal/idler single mode pair, while the other two traces show multimode behavior. **c**, Example of stable operation on the near-degenerate mode corresponding to the top panel of **a**; the OPO remained stable for more than 30 minutes without the use of any locking technique or environmental isolation.

to increase the effective free spectral range and limit oscillation to a single mode. An electro-optic modulator on the additional resonator would enable hopping between adjacent longitudinal modes of the main resonator [13]. Continuous mode-hop-free tuning of such nested resonators can also be achieved by a coordinated shifts in both resonators [14].

OPOs offer a large number of options in terms of coherence and frequency stabilization due to the different frequencies involved and potential for additional $\chi^{(2)}$ processes like sum-frequency generation. The OPO outputs can be stabilized directly to a reference cavity achieving a few kilohertz of relative stability over hours [15]. They can also be absolutely locked to atomic transitions, for instance, in Ref. [16], the OPO signal at 852 nm was locked to a hyperfine transition of Cs over several minutes. Such method could be extended to the infrared, for instance, using the same Cs transition to lock a signal at 1704 nm trough frequency doubling.

In summary, we have shown that on-chip OPOs can be pumped directly by compact semiconductor lasers without the need for additional bulky components like high power amplifiers or isolators, thus paving the way for the development of fully integrated, widely tunable, optical sources.

References

[1] M. Li, L. Chang, L. Wu, J. Staffa, J. Ling, U. A. Javid, S. Xue, Y. He, R. Lopez-rios, T. J. Morin, H. Wang, B. Shen, S. Zeng, L. Zhu, K. J. Vahala, J. E. Bowers, and Q. Lin, "Integrated Pockels laser," *Nature Communications*, vol. 13, no. 1, p. 5344, Sep. 2022, ISSN: 2041-1723. DOI: `10.1038/s41467-022-33101-6`.

[2] M. Zhang, B. Buscaino, C. Wang, A. Shams-Ansari, C. Reimer, R. Zhu, J. M. Kahn, and M. Lončar, "Broadband electro-optic frequency comb generation in a lithium niobate microring resonator," *Nature*, vol. 568, no. 7752, pp. 373–377, Apr. 2019, ISSN: 1476-4687. DOI: `10.1038/s41586-019-1008-7`.

[3] Photodigm Inc., *PH1064DBR Series*, www.photodigm.com.

[4] K. Petermann, *Laser Diode Modulation and Noise*. Springer Science & Business Media, Apr. 1991, ISBN: 978-0-7923-1204-8.

[5] I. D. Lindsay, G. A. Turnbull, M. H. Dunn, and M. Ebrahimzadeh, "Doubly resonant continuous-wave optical parametric oscillator pumped by a single-mode diode laser," *Optics Letters*, vol. 23, no. 24, pp. 1889–1891, Dec. 1998, ISSN: 1539-4794. DOI: `10.1364/OL.23.001889`.

[6] A. J. Henderson, P. M. Roper, L. A. Borschowa, and R. D. Mead, "Stable, continuously tunable operation of a diode-pumped doubly resonant optical parametric oscillator," *Optics Letters*, vol. 25, no. 17, pp. 1264–1266, Sep. 2000, ISSN: 1539-4794. DOI: `10.1364/OL.25.001264`.

[7] M. Achtenhagen, N. V. Amarasinghe, L. Jiang, J. Threadgill, and P. Young, "Spectral properties of high-power distributed bragg reflector lasers," *Journal of Lightwave Technology*, vol. 27, no. 16, pp. 3433–3437, Aug. 2009, ISSN: 1558-2213. DOI: `10.1109/JLT.2008.2005848`.

[8] A. W. Snyder and J. D. Love, *Optical Waveguide Theory* (Science Paperbacks 190). London ; New York: Chapman and Hall, 1983, ISBN: 978-0-412-09950-2.

[9] J. Mork, B. Tromborg, and J. Mark, "Chaos in semiconductor lasers with optical feedback: Theory and experiment," *IEEE Journal of Quantum Electronics*, vol. 28, no. 1, pp. 93–108, Jan. 1992, ISSN: 1558-1713. DOI: `10.1109/3.119502`.

[10] C. Henry, “Theory of the linewidth of semiconductor lasers,” *IEEE Journal of Quantum Electronics*, vol. 18, no. 2, pp. 259–264, Feb. 1982, ISSN: 1558-1713. DOI: `10.1109/JQE.1982.1071522`.

[11] P. A. Verrinder, L. Wang, J. Fridlander, F. Sang, V. Rosborough, M. Nickerson, G. Yang, M. Stephen, L. Coldren, and J. Klamkin, “Gallium arsenide photonic integrated circuit platform for tunable laser applications,” *IEEE Journal of Selected Topics in Quantum Electronics*, vol. 28, no. 1, pp. 1–9, 2021.

[12] P. A. Verrinder, L. Wang, J. Fridlander, F. Sang, V. Rosborough, M. Nickerson, G. Yang, M. Stephen, L. Coldren, and J. Klamkin, “Gallium Arsenide Photonic Integrated Circuit Platform for Tunable Laser Applications,” *IEEE Journal of Selected Topics in Quantum Electronics*, vol. 28, no. 1: Semiconductor Lasers, pp. 1–9, Jan. 2022, ISSN: 1558-4542. DOI: `10.1109/JSTQE.2021.3086074`.

[13] D. J. M. Stothard, I. D. Lindsay, and M. H. Dunn, “Continuous-wave pump-enhanced optical parametric oscillator with ring resonator for wide and continuous tuning of single-frequency radiation,” *Optics Express*, vol. 12, no. 3, pp. 502–511, Feb. 2004, ISSN: 1094-4087. DOI: `10.1364/OPEX.12.000502`.

[14] P. Groß, I. D. Lindsay, C. J. Lee, M. Nittmann, T. Bauer, J. Bartschke, U. Warring, A. Fischer, A. Kellerbauer, and K.-J. Boller, “Frequency control of a 1163 nm singly resonant OPO based on MgO:PPLN,” *Optics Letters*, vol. 35, no. 6, pp. 820–822, Mar. 2010, ISSN: 1539-4794. DOI: `10.1364/OL.35.000820`.

[15] O. Mhibik, T.-H. My, D. Pabœuf, F. Bretenaker, and C. Drag, “Frequency stabilization at the kilohertz level of a continuous intracavity frequency-doubled singly resonant optical parametric oscillator,” *Optics Letters*, vol. 35, no. 14, pp. 2364–2366, Jul. 2010, ISSN: 1539-4794. DOI: `10.1364/OL.35.002364`.

[16] S. Zaske, D.-H. Lee, and C. Becher, “Green-pumped cw singly resonant optical parametric oscillator based on MgO:PPLN with frequency stabilization to an atomic resonance,” *Applied Physics B*, vol. 98, no. 4, pp. 729–735, Mar. 2010, ISSN: 1432-0649. DOI: `10.1007/s00340-009-3871-7`.

Chapter 8

SIMULATING QUANTUM FLUCTUATIONS IN THREE-WAVE MIXING

> *"...the effect of this vacuum noise can be viewed as rather small, or infinite, depending on one's point of view"*
>
> — C. Gardiner and P. Zoller, *Quantum Noise*

The goal of this chapter is to point out that there is a rigorous method for adding fluctuations to a classical propagation equation in order to accurately estimate quantum correlations. More precisely, it is possible to find a set of stochastic differential equations (SDEs) that resemble the classical coupled wave equations plus some additional noise terms. The machinery necessary is that of phase space methods that, although developed to analyze open-quantum systems, also reveal fluctuation dynamics in energy conserving systems.

As we develop the model, our toy system is going to be that of spontaneous parametric down-conversion (SPDC) that leads to parametric superfluorescence if the amplifier gain is large enough. With a CW pump, only a single signal/idler pair needs to be considered, and the Heisenberg equations of motion can be solved directly yielding a non-zero output that can be traced back to the non-commutative nature of the bosonic destruction and creation operators. It was noticed early on [1] that the same result can be recovered by using the classical equations of motion plus some initial noise. We will first review this result and point out some possible issues with this ad-hoc procedure.

We will then briefly review the phase space methods necessary to derive a set of SDEs that are exactly equivalent to the Heisenberg or Schrodinger equations of motion. The main advantage of this technique is that it can be extended to the case of a large number of interacting spectral modes. Indeed, the problem of performing quantum simulations for wideband systems have become increasingly important in the last few years due to the possibility to perform quantum information processing (QIP) with ultrashort pulses [2]–[4]. These systems, having a large number of spectral modes, cannot be simulated directly in Hilbert space. For instance, simulating just 100 spectral modes, each one described in a (rather small) 10-dimensional base, would require evolving a quantum state in 10^{100}-dimensional Hilbert space!

8.1 Problems with the ad-hoc semi-classical approach

Consider the Hamiltonian for three-wave mixing, with perfect phase matching, frequency matching ($\omega_p = \omega_s + \omega_i$), and on a rotating frame that removes the free-evolving dynamics,

$$H_{\text{SPDC}} = \hbar\kappa\Big(a_p a_s^\dagger a_i^\dagger + a_p^* a_s a_i\Big) \approx \hbar\kappa\Big(A_p a_s^\dagger a_i^\dagger + A_p^* a_s a_i\Big), \tag{8.1}$$

where we assumed that the coupling constant κ is real, and approximate the pump field as a classical field represented by its complex amplitude A_p. The Heisenberg equations of motion for the operators $a_s(t)$ and $a_i^\dagger(t)$ follow directly:

$$\frac{\mathrm{d}a_s}{\mathrm{d}t} = \frac{i}{\hbar}[H, a_s] = -i\kappa A_p a_i^\dagger, \quad \frac{\mathrm{d}a_i^\dagger}{\mathrm{d}t} = \frac{i}{\hbar}\Big[H, a_i^\dagger\Big] = i\kappa A_p^* a_s. \tag{8.2}$$

This is a linear system of differential equations with solutions

$$a_s(t) = \cosh(gt)a_s(0) + ie^{i\phi}\sinh(gt)a_i^\dagger(0), \tag{8.3}$$

$$a_i^\dagger(t) = \cosh(gt)a_i^\dagger(0) - ie^{-i\phi}\sinh(gt)a_s(0), \tag{8.4}$$

where $g = \kappa\big|A_p\big|$, and ϕ is the phase of the pump field A_p. We can now calculate all the correlations. For the case of SPDC, we assume the system started from vacuum at the signal and idler, $\langle 0|a_{s,i}|0\rangle = 0$. The expected number of photons at any time is

$$\begin{aligned}\langle 0|n_s(t)|0\rangle = \langle 0|a_s^\dagger(t)a_s(t)|0\rangle &= \cosh^2(gt)\,\langle 0|a_s^\dagger(0)a_s(0)|0\rangle \\ &+ \sinh^2(gt)\,\langle 0|a_i(0)a_i^\dagger(0)|0\rangle \\ &+ ie^{i\phi}\sinh(gt)\cosh(gt)\,\langle 0|a_s^\dagger(0)a_i^\dagger(0)|0\rangle \\ &- ie^{-i\phi}\sinh(gt)\cosh(gt)\,\langle 0|a_s(0)a_i(0)|0\rangle\,,\end{aligned}$$

where the only non-zero term is the second one (highlighted in blue), so we arrive at the well-known result $\langle 0|n_s(t)|0\rangle = \sinh^2(gt)$.

We now switch gears and solve the equivalent problem in the classical domain. Complex numbers A_s and A_i will play the role of the operators a_s and a_i, in the sense that $\langle a_s\rangle = A_s$, $\Big\langle a_s^\dagger\Big\rangle = A_s^*$, and so on. We normalize these complex amplitudes so that $|A|^2$ has units of number of photons. The classical coupled-wave equations have the same form as Eq. (8.2),

$$\frac{\mathrm{d}A_s}{\mathrm{d}t} = -i\kappa A_p A_i^*, \quad \frac{\mathrm{d}A_i^*}{\mathrm{d}t} = i\kappa A_p^* A_s,$$

and, therefore, similar solutions

$$\begin{aligned}
A_s(t) &= \cosh(gt)A_s(0) + ie^{i\phi}\sinh(gt)A_i^*(0),\\
A_i^*(t) &= \cosh(gt)A_i^*(0) - ie^{-i\phi}\sinh(gt)A_s(0).
\end{aligned}$$

However, for zero initial conditions, the above solutions give $A_s(t) = A_i(t) = 0$ for all time. Maxwell's equations alone do not predict SPDC. But some correct results can be obtained by assuming noisy initial conditions. Indeed, if we assume that $A_s(0)$ and $A_i(0)$ have independent and identically distributed real and imaginary parts, with zero mean and variance $\sigma^2/2$, we get the following for the average photon number

$$\begin{aligned}
\left\langle |A|^2 \right\rangle = &\cosh^2(gt)\left\langle |A_s(0)|^2\right\rangle + \sinh^2(gt)\left\langle |A_i(0)|^2\right\rangle\\
&+ ie^{i\phi}\sinh(gt)\cosh(gt)\left\langle A_s^*(0)A_i^*(0)\right\rangle\\
&- ie^{-i\phi}\sinh(gt)\cosh(gt)\left\langle A_s(0)A_i(0)\right\rangle. \qquad (8.5)
\end{aligned}$$

The last two terms are zero due to the assumption of independent random variables with zero mean. Furthermore, $\left\langle |A_s(0)|^2\right\rangle = \left\langle X_s^2 + Y_s^2\right\rangle = \sigma_s^2$. Similarly, $\left\langle |A_i(0)|^2\right\rangle = \sigma_i^2$. Substituting this into Eq. 8.5, we get

$$\left\langle |A|^2\right\rangle = \sigma_s^2\cosh^2(gt) + \sigma_i^2\sinh^2(gt). \qquad (8.6)$$

There are two ways to recover the quantum result, $\langle n_s(t)\rangle = \sinh^2(gt)$. The first is to assume that all the "noise" comes from the idler, i.e., set $\sigma_s^2 = 0$ and $\sigma_i^2 = 1$. This is an awkward argument, why would only the idler have noise? By symmetry, if we are interested in the idler, then we have to assume that all the noise comes from the signal.

The second way to force Eq. (8.6) to agree with the quantum result was proposed by Kleinman [5]. It consists on assuming the same noise variance in both signal and idler $\sigma_s^2 = \sigma_i^2 = 1/2$, and then also to subtract the initial noise present on the signal. This works quite nicely:

$$\begin{aligned}
\left\langle |A|^2\right\rangle &= \sigma_s^2\cosh^2(gt) + \sigma_i^2\sinh^2(gt) - \sigma_s^2\\
&= \frac{1}{2}\cosh^2(gt) + \frac{1}{2}\sinh^2(gt) - \frac{1}{2} = \sinh^2(gt). \qquad (8.7)
\end{aligned}$$

This symmetric fix is more elegant, but, without knowing where it comes from, it is not easy to generalize to other correlations. For instance, consider estimating the second moment $\left\langle n^2(t)\right\rangle$. Should we also subtract 1/2 from $\left\langle |A|^4\right\rangle$? That does not

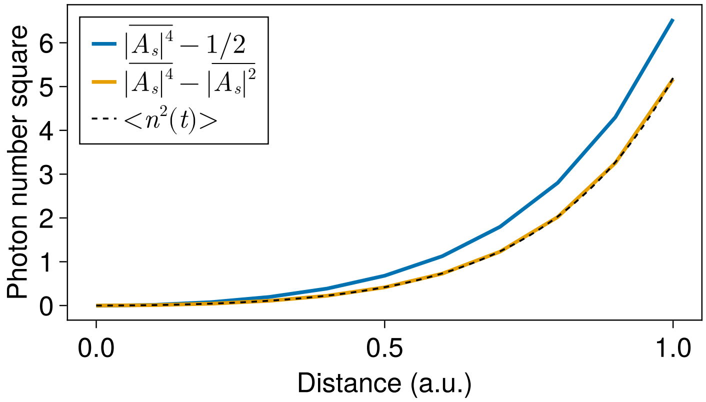

Figure 8.1: **Estimation of the photon number square.** The full quantum mechanical solution is shown as a dashed black line. Just subtracting 1/2 from the classical average $\langle |A|^4 \rangle$ does not recover the correct result (blue trace). Subtracting the variable $\langle |A|^2 \rangle$ is the correct choice in this case (orange trace). The notation $\overline{x}$ indicates a numerical estimation of $\langle x \rangle$.

work. It turns out that, for this observable, the correction term is not even a constant, but $\langle |A|^2 \rangle$. The results of the quantum mechanical solution along with these two guesses are shown in Fig. 8.1.

In case it is not clear yet that we should not continue blindly adding noise terms to the initial conditions and then trying to correct their undesired effects, let us consider another troubling problem: full three-wave mixing. Should we add noise to all waves? Or just to the lower frequency waves? Are the signal and idler waves going to interact with each other and produce SFG noise at the pump frequency? A trivial example that produces an absurd result is that in which all three waves are on their vacuum state. In this case, quantum mechanics predicts nothing will happen and all three waves will remain in the vacuum state. Figure 8.2 shows the result of the classical simulation with initial noise in all waves. The “vacuum” noise from the pump wave is getting down-converted to the signal and idler. This results in a negative net number of photons at the pump. But hey, at least energy is being conserved! This result proves that there is something fundamentally wrong with this method and that we need a rigorous way to add fluctuations to classical nonlinear models.

8.2 General observations about semi-classical approaches

It is probably wise to step back and ponder what it is that we are trying to do, because there is a fundamental loophole in my exposition so far: we are trying to replace

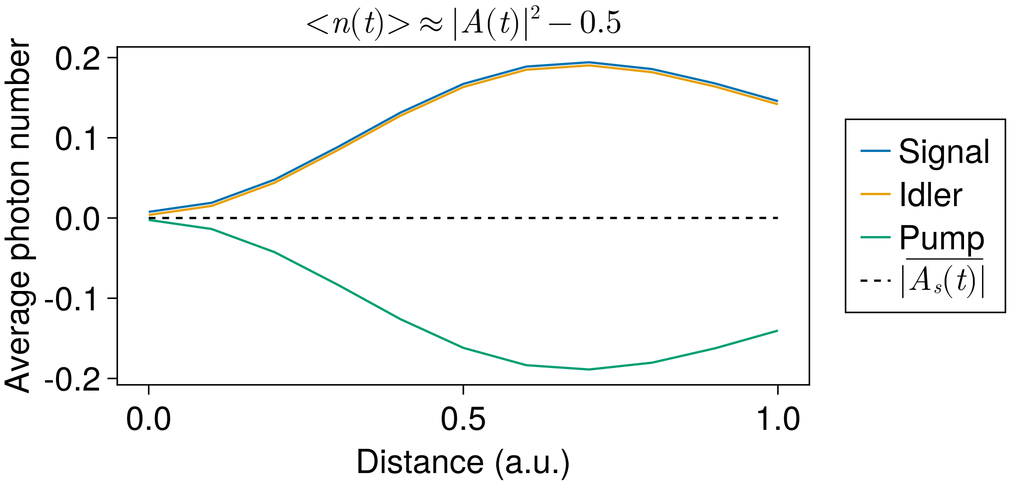

Figure 8.2: **Classical simulation of TWM with all waves starting from a hypothetical vacuum noise.** Nonsensical results include a negative number of photons appearing at the highest frequency. Black dashed line shows the average signal field, and it is included to confirm a low sampling bias.

operators with complex numbers. Is this even possible? One obvious problem is that operators do not always commute, but numbers do. This should be an eye opener, the *same operator* can be written in several different ways, for instance $a^\dagger a = aa^\dagger - 1 = (aa^\dagger + a^\dagger a - 1)/2$, but just replacing the operators by complex numbers lead to three different expressions, namely: $|A|^2 \neq |A|^2 - 1 \neq |A|^2 - 1/2$.

That very last expression matches Kleinman's suggestion of estimating $\langle a^\dagger a \rangle$ by $|A|^2 - 1/2$. Maybe the key is that before replacing the operators a and $a^\dagger$ by the complex numbers A and A^*, we need to rewrite our operator expression in a *symmetrically ordered* fashion, i.e. with complete symmetry in the appearances of a and $a^\dagger$. We will see that this is actually the case, since using the classical equations of motion with stochastic initial conditions can be formalized with the use of the *truncated* Wigner representation, where we can calculate expectation values of operators by first expressing them in symmetric order and then replacing them by complex numbers. This is not the only way to address the problem. Instead of using noisy initial conditions, it is possible to add stochastic terms to the differential equations directly. This in turn would lead to requiring different orderings for the operators.

Our goal is to find a set of *stochastic differential equations* (SDE) that are *equivalent* to the quantum evolution. These equations can be solved numerically to obtain *trajectories* in phase space. Expectation values, including two-time correlations, can be found by averaging over a large number of these trajectories.

The path to SDEs takes us through master equations, phase space representations, and Fokker-Planck equations. These techniques were mainly developed to study *open-quantum systems*, while our system is not open. We have no losses, no reservoirs, not tracing out of subsystems. It may seem then that this route is unnecessarily complicated. If the system is closed, there are other ways to tackle the problem, and using open-system techniques will not provide additional insight. This is both right and wrong. Right because the system can be evolved, in principle, using the Schrodinger or Heisenberg pictures. Wrong because the open-quantum techniques gives us a computational advantage by allowing us to simulate large systems that are impractical in the Heisenberg and Schrodinger pictures due to the exponentially large size of the Hilbert spaces involved.

Open-quantum system techniques also provide physical insight by exposing the raw uncertainties that characterize quantum systems. Note that the Heisenberg equations of motion contained no noise terms. There were no Langevin forces and no bath operators. In fact, since our system is closed, all commutators are automatically conserved during time evolution:

$$\begin{aligned}\frac{\mathrm{d}}{\mathrm{d}t}\left[a_s(t), a_s^\dagger(t)\right] &= \frac{i}{\hbar}\left[H, a_s(t)a_s^\dagger(t) - a_s^\dagger(t)a_s(t)\right] = 0,\\ \frac{\mathrm{d}}{\mathrm{d}t}\left[a_s(t), a_i^\dagger(t)\right] &= \frac{i}{\hbar}\left[H, a_s(t)a_i^\dagger(t) - a_i^\dagger(t)a_s(t)\right] = 0,\end{aligned}$$

and so on. But we will see that, even in this case, noise is necessary to accurately model the system dynamics. This is *true* quantum noise, coming from the field commutators, i.e. from the Heisenberg uncertainty principle. This is fundamentally different from loss, which is just an approximation to model our incapacity and unwillingness to track too many degrees of freedom.

8.3 Phase space representations

We specify the quantum state $|\Psi\rangle$ of a mode of the electromagnetic field using the density matrix $\rho = |\Psi\rangle\langle\Psi|$. In turn, there are several phase spaces that can be used to represent ρ using functions in the complex plane. There are two key advantages of using this approach: first, it is easier to visualize functions in the complex plane as opposed to operators in Hilbert space. Second, the optical equivalence theorem allows us to calculate expectation values as if these phase space functions where probability densities

$$\langle O\rangle = \int f_\rho(\alpha,\alpha^*) O_f(\alpha,\alpha^*)\mathrm{d}^2\alpha, \tag{8.8}$$

where α is a complex variable, $f_\rho(\alpha,\alpha^*)$ is the phase space representation of the density matrix, while $O_f(\alpha,\alpha^*)$ is a representation of the operator O. The explicit arguments (α,α^*) indicate that these functions need not be analytic in the complex α-plane. The operator representation $O_f(\alpha,\alpha^*)$ is, in general, related to a particular operator ordering, as we will see.

The P representation

The coherent states $|\alpha\rangle$ form an overcomplete basis, so they can be used to expand any quantum state in a diagonal representation known as the P representation,

$$\rho = \int P(\alpha)\,|\alpha\rangle\,\langle\alpha|\,\mathrm{d}^2\alpha. \tag{8.9}$$

Coherent states are represented as delta functions in the P representation. For instance, the coherent state $|\alpha_0\rangle$ with density matrix $|\alpha_0\rangle\langle\alpha_0|$ is represented by $P(\alpha) = \delta(\alpha-\alpha_0)$. Many interesting states, like squeezed states or number states, have P representation that are more singular than a delta function. This makes the P representation somewhat hard to work with and visualize. However, since coherent states are the closest states to classical laser light, the P representation may represent a natural choice for us. In fact, in the classical coupled-wave equations we are already representing our fields as coherent states with amplitude $\alpha = A$ (the complex amplitude A of our classical field corresponds to $\langle a\rangle$, which for a coherent state is just $\langle\alpha|a|\alpha\rangle = \alpha$).

Now that we know how to represent the density matrix, we need to discuss how to represent operators. The correct ordering for the P representation is the *normal-order*, in which all the creation operators are on the left of all the annihilation operators. The optical equivalence theorem (8.8) then looks like this

$$\left\langle a^{\dagger n}a^m\right\rangle = \int P(\alpha)\alpha^{*n}\alpha^m\mathrm{d}^2\alpha. \tag{8.10}$$

For example, suppose that we want to calculate $\left\langle n^2\right\rangle$, knowing that the system is in a state represented by $P(\alpha)$. We first put n^2 into normal order $n^2 = a^\dagger a a^\dagger a = a^\dagger a^\dagger a a + a^\dagger a$, and for the expected value:

$$\left\langle n^2\right\rangle = \int P(\alpha)(|\alpha|^4 + |\alpha|^2)\mathrm{d}^2\alpha. \tag{8.11}$$

The Wigner representation

The Wigner representation can be expressed in terms of the P representation,

$$W(\alpha) = \frac{2}{\pi} \int P(\beta) \exp\Big(-2|\alpha - \beta|^2\Big) \mathrm{d}^2\beta. \tag{8.12}$$

The Gaussian convolution is enough to make the Wigner representation always non-singular and real. However, it can still be negative as it is in the case of important states like number states and cat states. This prohibits direct sampling of the distribution for these states.

To use the optical equivalence theorem with the Wigner representation, operators need to be expressed in a symmetrically-ordered fashion. This ordering is convenient when working with the quadratures of the field $\hat{x} = (a + a^\dagger)/2$ and $\hat{y} = (a - a^\dagger)/2i$, since moments of these operators can be automatically expressed in symmetric order. On the other hand, moments of a require some extra work, for instance:

$$(a^\dagger a)^2 = \frac{aaa^\dagger a^\dagger + a^\dagger a^\dagger aa + aa^\dagger aa^\dagger + a^\dagger aa^\dagger a + aa^\dagger a^\dagger a + a^\dagger aaa^\dagger}{6} - \frac{aa^\dagger + a^\dagger a}{2}, \tag{8.13}$$

which in phase space reduces to

$$(a^\dagger a)^2 \to |\alpha|^4 - |\alpha|^2. \tag{8.14}$$

This is the origin of the correct expression for $\langle n^2 \rangle$ illustrated in Fig. 8.1.

The Q representation

This representation, defined by

$$Q(\alpha) = \frac{\langle \alpha | \rho | \alpha \rangle}{\pi}, \tag{8.15}$$

can also be written as a convolution of the P representation with a Gaussian:

$$Q(\alpha) = \frac{1}{\pi} \int P(\beta) \exp\Big(-|\alpha - \beta|^2\Big) \mathrm{d}^2\beta. \tag{8.16}$$

The Q representation is well behaved and always positive. Operators need to be anti-normally-ordered.

The positive P representation

To motivate the introduction of yet another epresentation, we need to look ahead. The three representations briefly reviewed above are the most known and used in quantum optics, but none of them will be satisfactory for our goal.

Our next step will be to find an equation of motion for whatever representation we choose. The step after that is more nuanced: we need to derive a stochastic differential equation that is equivalent to the equation of motion for our representation. This is relatively hard to do, so we will only be able to do it when the equation of motion for the representation is a Fokker–Planck equation with a semi-positive definite diffusion coefficient. It is this step that fails will all three previous representations. The P and Q representations often lead to negative diffusion coefficients, while the Wigner distribution has higher order derivatives than a Fokker-Planck equation.

The positive-P representation, introduced by Drummond and Gardiner [6], solves these issues. It is defined by

$$\rho = \int P_+(\alpha, \beta) \frac{|\alpha\rangle \langle\beta^*|}{\langle\beta^*|\alpha\rangle} \mathrm{d}^2\alpha \mathrm{d}^2\beta, \tag{8.17}$$

where α and β are two independent complex variables. By comparing with Eq. (8.9), we see that the P representation is a special case of the positive-P representation with $\beta = \alpha^*$. It can be proven that the positive P representation can be chosen to be positive for any density operator ρ (just like the Q representation). Furthermore, whenever there is a Fokker-Planck equation for the time evolution of the positive P representation, there is a corresponding equation for the positive-P representation with positive semi-definite diffusion coefficients. Thus, the positive-P representation can be used to generate stochastic differential equations for a large number of systems, at the expense of doubling the number of variables. Just like the P representation, the positive-P representation gives expected values of normally-ordered operators.

8.4 Time evolution of phase space distributions

Since the phase space functions are just representations of the density matrix ρ, we can use the von Neumann equation for the time evolution of the density matrix,

$$\frac{\partial \rho}{\partial t} = \frac{1}{i\hbar}[H, \rho], \tag{8.18}$$

to derive a time evolution equation for the phase space representations. The key result is a replacement of operator algebra by complex variable multiplications and differentiation [7]. The only approximation made to obtain this result is neglecting boundary terms during an integration by parts. This requires that the phase space distributions vanish sufficiently fast towards infinity; a condition that is typically satisfied by most distributions for a large class of quantum states [8].

This procedure leads to the following correspondences for the positive-P representation:

$$a\rho \rightarrow \alpha P_+(\alpha,\beta), \quad a^\dagger\rho \rightarrow \left(\beta - \frac{\partial}{\partial\alpha}\right)P_+(\alpha,\beta), \tag{8.19}$$

$$\rho a \rightarrow \left(\alpha - \frac{\partial}{\partial\beta}\right)P_+(\alpha,\beta), \quad \rho a^\dagger \rightarrow \beta P_+(\alpha,\beta), \tag{8.20}$$

and for the Wigner representation:

$$a\rho \rightarrow \left(\alpha + \frac{1}{2}\frac{\partial}{\partial\alpha^*}\right)W(\alpha), \quad a^\dagger\rho \rightarrow \left(\alpha^* - \frac{1}{2}\frac{\partial}{\partial\alpha}\right)W(\alpha), \tag{8.21}$$

$$\rho a \rightarrow \left(\alpha - \frac{1}{2}\frac{\partial}{\partial\alpha^*}\right)W(\alpha), \quad \rho a^\dagger \rightarrow \left(\alpha^* + \frac{1}{2}\frac{\partial}{\partial\alpha}\right)W(\alpha). \tag{8.22}$$

8.5 Fokker-Planck equations and stochastic differential equations

Once an equation of motion for the phase space distribution is found, the next step is to find the corresponding stochastic different equation. This is not a simple task and, for the most part, we are limited to the case in which the distribution satisfies a Fokker-Planck equation

$$\frac{\partial P(\boldsymbol{\alpha})}{\partial t} = \left(-\sum_i \frac{\partial A_i(\boldsymbol{\alpha})}{\partial\alpha_i} + \frac{1}{2}\sum_{i,j}\frac{\partial^2 D_{ij}(\boldsymbol{\alpha})}{\partial\alpha_i\partial\alpha_i}\right)P(\boldsymbol{\alpha}), \tag{8.23}$$

where $\boldsymbol{\alpha}$ is a vector of complex variables α_i, $\mathbf{A}$ is the drift vector with components A_i, and $\mathbf{D}$ is the diffusion matrix with elements D_{ij}. When the diffusion matrix is positive semi-definite, this equation is equivalent to the following Itô stochastic differential equation

$$\mathrm{d}\boldsymbol{\alpha} = \mathbf{A}(\boldsymbol{\alpha})\mathrm{d}t + \mathbf{B}(\boldsymbol{\alpha})\,\mathrm{d}\mathbf{W}\,, \tag{8.24}$$

where $\boldsymbol{\alpha}$ is a vector of complex *random* variables α_i, $\mathbf{A}$ is the same deterministic drift vector from the Fokker-Planck equation (8.23), the deterministic matrix $\mathbf{B}$ is related to the diffusion matrix by the factorization $\mathbf{D} = \mathbf{B}\mathbf{B}^{\mathbf{T}}$, and $\mathbf{W}$ is a vector of independent Wiener processes [7].

8.6 Three-wave mixing in the Wigner representation

Let us illustrate this formalism by considering the case of three modes at frequencies ω_1, ω_2 and $\omega_3 = \omega_1 + \omega_2$, with corresponding annihilation operators a_1, a_2, a_3, interacting under the following Hamiltonian

$$H = \hbar\kappa\left(a_1 a_2 a_3^\dagger + a_1^\dagger a_2^\dagger a_3\right). \tag{8.25}$$

The density operator evolves under Von Neumann equation (8.18),

$$\frac{\partial\rho}{\partial t} = -i\kappa\Big(a_1 a_2 a_3^\dagger\rho - \rho a_1 a_2 a_3^\dagger + a_1^\dagger a_2^\dagger a_3\rho - \rho a_1^\dagger a_2^\dagger a_3\Big). \tag{8.26}$$

We can then find an equation of motion for the Wigner distribution $W(\alpha_1,\alpha_2,\alpha_3)$ by directly using the recipes from Eqs. (8.21) and (8.22),

$$\begin{aligned}\frac{\partial W(\boldsymbol{\alpha})}{\partial t} = -i\kappa \Bigg[&\left(\alpha_1 + \frac{1}{2}\frac{\partial}{\partial\alpha_1^*}\right)\left(\alpha_2 + \frac{1}{2}\frac{\partial}{\partial\alpha_2^*}\right)\left(\alpha_3^* - \frac{1}{2}\frac{\partial}{\partial\alpha_3}\right)\\ &-\left(\alpha_1 - \frac{1}{2}\frac{\partial}{\partial\alpha_1^*}\right)\left(\alpha_2 - \frac{1}{2}\frac{\partial}{\partial\alpha_2^*}\right)\left(\alpha_3^* + \frac{1}{2}\frac{\partial}{\partial\alpha_3}\right)\\ &+\left(\alpha_1^* - \frac{1}{2}\frac{\partial}{\partial\alpha_1}\right)\left(\alpha_2^* - \frac{1}{2}\frac{\partial}{\partial\alpha_2}\right)\left(\alpha_3 + \frac{1}{2}\frac{\partial}{\partial\alpha_3^*}\right)\\ &-\left(\alpha_1^* + \frac{1}{2}\frac{\partial}{\partial\alpha_1}\right)\left(\alpha_2^* + \frac{1}{2}\frac{\partial}{\partial\alpha_2}\right)\left(\alpha_3 - \frac{1}{2}\frac{\partial}{\partial\alpha_3^*}\right)\Bigg] W(\boldsymbol{\alpha}),\end{aligned} \tag{8.27}$$

which after some algebra simplifies to:

$$\begin{aligned}\frac{\partial W(\boldsymbol{\alpha})}{\partial t} = -i\kappa \Bigg[&\alpha_1\alpha_3^*\frac{\partial}{\partial\alpha_2^*} + \alpha_2\alpha_3^*\frac{\partial}{\partial\alpha_1^*} - \alpha_1\alpha_2\frac{\partial}{\partial\alpha_3} - \frac{1}{4}\frac{\partial^3}{\partial\alpha_1^*\partial\alpha_2^*\partial\alpha_3}\\ &-\alpha_1^*\alpha_3\frac{\partial}{\partial\alpha_2} - \alpha_2^*\alpha_3\frac{\partial}{\partial\alpha_1} + \alpha_1^*\alpha_2^*\frac{\partial}{\partial\alpha_3^*} + \frac{1}{4}\frac{\partial^3}{\partial\alpha_1\partial\alpha_2\partial\alpha_3^*}\Bigg] W(\boldsymbol{\alpha}).\end{aligned} \tag{8.28}$$

This is not a Fokker-Planck equation due to the third order derivatives so we cannot find a stochastic differential equations by the equivalence from Eq. (8.24), although Drummond has made significant progress in this direction [9], [10]. The most common idea, however, is to discard the third order derivatives, leading to the *truncated* Wigner representation W_T satisfying

$$\begin{aligned}\frac{\partial W_T(\boldsymbol{\alpha})}{\partial t} = -i\kappa \Bigg[&\alpha_1\alpha_3^*\frac{\partial}{\partial\alpha_2^*} + \alpha_2\alpha_3^*\frac{\partial}{\partial\alpha_1^*} - \alpha_1\alpha_2\frac{\partial}{\partial\alpha_3}\\ &-\alpha_1^*\alpha_3\frac{\partial}{\partial\alpha_2} - \alpha_2^*\alpha_3\frac{\partial}{\partial\alpha_1} + \alpha_1^*\alpha_2^*\frac{\partial}{\partial\alpha_3^*}\Bigg] W_T(\boldsymbol{\alpha}).\end{aligned} \tag{8.29}$$

Because there are no second order derivatives, the diffusion matrix $\mathbf{D} = 0$ and the mapping from Eq. (8.24) leads to a system of deterministic differential equations

$$\frac{\mathrm{d}\alpha_1}{\mathrm{d}t} = -i\kappa\alpha_2^*\alpha_3, \quad \frac{\mathrm{d}\alpha_2}{\mathrm{d}t} = -i\kappa\alpha_1^*\alpha_3, \quad \frac{\mathrm{d}\alpha_3}{\mathrm{d}t} = -i\kappa\alpha_1\alpha_2, \tag{8.30}$$

and their conjugates. These are just the classical equations of motion. Therefore, by solving the classical equations of motion we are evolving the fields corresponding to the truncated Wigner representation. The evolution is deterministic but the initial conditions are not, since the Wigner function for the initial state plays the role of a probability distribution. For instance, if a field is in the coherent state $|\alpha_0\rangle$, then its Wigner representation is

$$W(\alpha) = \frac{2}{\pi}e^{-2|\alpha-\alpha_0|^2} = \left(\sqrt{\frac{2}{\pi}}e^{-2(x-x_0)^2}\right)\left(\sqrt{\frac{2}{\pi}}e^{-2(y-y_0)^2}\right), \tag{8.31}$$

where $\alpha = x + iy$. This corresponds to independent Gaussian distributions for the real and imaginary parts, each with variance $1/4$, which leads to a variance of $1/2$ for $|\alpha|^2$, as expected.

Thus, this answers most of the questions we had at the beginning. By simulating the classical wave equations and adding a complex Gaussian noise, we are implicitly using the truncated Wigner representation and assuming that our initial fields are in a coherent state (with vacuum as a particular case with α_0=0). In order to calculate the expectation values of moments, we must first write the operators in a totally symmetric order. This also makes clear the limitations of the approach. For instance, since we must sample the distribution of the initial state, it is not possible to directly start a field in a number state, or a superposition state, or any other state in which the Wigner distribution is negative.

A second drawback of this approach is that we have discarded the third order terms in Eq. (8.28), so even for cases where we can sample the initial fields, the solutions will not always be correct. This was exactly the problem that lead to negative photons in the example from Fig. 8.2. If all the fields start at vacuum, then the Wigner distribution is

$$W(\boldsymbol{\alpha}) = \left(\frac{2}{\pi}\right)^3 e^{-2|\alpha_1|^2}e^{-2|\alpha_2|^2}e^{-2|\alpha_3|^2}, \tag{8.32}$$

and by substitution in Eq. (8.28) leads to $\mathrm{d}W/\mathrm{d}t = 0$, confirming that the system will just stay in vacuum, as expected. However, substitution in the truncated version, Eq. (8.29), leads to $\mathrm{d}W/\mathrm{d}t \neq 0$, which is not correct, but it is what is being simulated assuming classical equations plus initial fluctuations.

8.7 Three-wave mixing in the positive-P representation

The positive-P representation can address both problems associated with the Wigner representation: any initial state can be sampled as the distribution is always positive, and there is no need to discard higher order derivatives.

To find an equation of motion for the positive-P representation, we start from Eq. (8.26) and apply the recipes from Eqs. (8.19) and (8.20),

$$\begin{aligned}\frac{\partial P(\boldsymbol{\alpha},\boldsymbol{\beta})}{\partial t} &= -i\kappa\left[\alpha_1\alpha_2\left(\beta_3-\frac{\partial}{\partial\alpha_3}\right)-\left(\alpha_1-\frac{\partial}{\partial\beta_1}\right)\left(\alpha_2-\frac{\partial}{\partial\beta_2}\right)\beta_3\right.\\ &\quad\left.+\left(\beta_1-\frac{\partial}{\partial\alpha_1}\right)\left(\beta_2-\frac{\partial}{\partial\alpha_2}\right)\alpha_3-\beta_1\beta_2\left(\alpha_3-\frac{\partial}{\partial\beta_3}\right)\right]P(\boldsymbol{\alpha},\boldsymbol{\beta}),\\ &= -i\kappa\left[-\alpha_1\alpha_2\frac{\partial}{\partial\alpha_3}-\beta_1\alpha_3\frac{\partial}{\partial\alpha_2}-\beta_2\alpha_3\frac{\partial}{\partial\alpha_1}\right.\\ &\quad+\beta_1\beta_2\frac{\partial}{\partial\beta_3}+\alpha_1\beta_3\frac{\partial}{\partial\beta_2}+\alpha_2\beta_3\frac{\partial}{\partial\beta_1}\\ &\quad\left.+\alpha_3\frac{\partial^2}{\partial\alpha_1\partial\alpha_2}-\beta_3\frac{\partial^2}{\partial\beta_1\partial\beta_2}\right]P(\boldsymbol{\alpha},\boldsymbol{\beta}). \end{aligned} \tag{8.33}$$

This is a Fokker-Planck equation, and it can be shown that there exists a positive-P distribution that has a positive semi-definite diffusion matrix in terms of the real and imaginary parts of α_i and β_i [7]. Ignoring the subtleties involved, we can directly get the following system of stochastic differential equations

$$\begin{aligned}\frac{\mathrm{d}\alpha_1}{\mathrm{d}t} &= -i\kappa\beta_2\alpha_3+\sqrt{-2i\kappa\alpha_3}\mathrm{d}W_1, & \frac{\mathrm{d}\beta_1}{\mathrm{d}t} &= i\kappa\alpha_2\beta_3+\sqrt{2i\kappa\beta_3}\mathrm{d}W_2,\\ \frac{\mathrm{d}\alpha_2}{\mathrm{d}t} &= -i\kappa\beta_1\alpha_3+\sqrt{-2i\kappa\alpha_3}\mathrm{d}W_3, & \frac{\mathrm{d}\beta_2}{\mathrm{d}t} &= i\kappa\alpha_1\beta_3+\sqrt{2i\kappa\beta_3}\mathrm{d}W_4,\\ \frac{\mathrm{d}\alpha_3}{\mathrm{d}t} &= -i\kappa\alpha_1\alpha_2, & \frac{\mathrm{d}\beta_3}{\mathrm{d}t} &= i\kappa\beta_1\beta_2, \end{aligned} \tag{8.34}$$

where the $\mathrm{d}W_i$ are independent Wiener increments. These equations are similar to the classical equations of motion with the substitutions $A \longrightarrow \alpha$ and $A^* \longrightarrow \beta$, but here α and β are independent random variables that are only conjugate to each other in the mean. Also note that only the low frequency fields are driven by fluctuation terms; these produce spontaneous parametric down-conversion!

The main advantages of Eqs. (8.34) is that they represent the evolution of the positive P distribution exactly, i.e., no approximations were made in going from Eq. (8.33) to Eqs. (8.34). Also, any quantum state can be sampled as the initial condition since the distribution is always positive [11].

8.8 Conclusions

Using a stochastic initial condition can be formalized with the use of the *truncated* Wigner representation. However, there are several drawbacks. First, quantum states with negative Wigner distributions cannot be sampled as initial conditions. For instance, a simulation cannot be started on a number state. Second, because the method is not exact, one does not know for sure if the result of a given simulation is valid. The truncated Wigner representation has one enormous advantage to compensate for these shortcomings: the equations of motion are deterministic so one can use the same numerical solvers developed for classical wave propagation.

The positive-P representation solves the issues present with the truncated Wigner representation. All density matrices can be sampled since the representation is strictly positive. The method is exact, except in cases where the distribution does not go to zero fast enough at infinity; but these pathological cases can be spotted by trajectories that diverge to infinity. It comes with its own drawbacks. First, it requires a doubling in the number of variables used. Second, it leads to truly stochastic differential equations that may require specialized numerical solvers [12].

References

[1] W. H. Louisell, A. Yariv, and A. E. Siegman, "Quantum fluctuations and noise in parametric processes. I.," *Physical Review*, vol. 124, no. 6, pp. 1646–1654, Dec. 1961. doi: `10.1103/PhysRev.124.1646`.

[2] R. Nehra, R. Sekine, L. Ledezma, Q. Guo, R. M. Gray, A. Roy, and A. Marandi, "Few-cycle vacuum squeezing in nanophotonics," *Science*, vol. 377, no. 6612, pp. 1333–1337, Sep. 16, 2022. doi: `10.1126/science.abo6213`.

[3] R. Yanagimoto, E. Ng, L. G. Wright, L. G. Wright, T. Onodera, T. Onodera, and H. Mabuchi, "Efficient simulation of ultrafast quantum nonlinear optics with matrix product states," *Optica*, vol. 8, no. 10, pp. 1306–1315, Oct. 2021, issn: 2334-2536. doi: `10.1364/OPTICA.423044`. (visited on 11/12/2021).

[4] R. Yanagimoto, E. Ng, A. Yamamura, T. Onodera, L. G. Wright, M. Jankowski, M. M. Fejer, P. L. McMahon, and H. Mabuchi, "Onset of non-Gaussian quantum physics in pulsed squeezing with mesoscopic fields," *Optica*, vol. 9, no. 4, pp. 379–390, Apr. 2022, issn: 2334-2536. doi: `10.1364/OPTICA.447782`. (visited on 04/24/2023).

[5] D. A. Kleinman, "Theory of Optical Parametric Noise," *Physical Review*, vol. 174, no. 3, pp. 1027–1041, Oct. 1968. doi: `10.1103/PhysRev.174.1027`.

[6] P. D. Drummond and C. W. Gardiner, "Generalised P-representations in quantum optics," *Journal of Physics A: Mathematical and General*, vol. 13, no. 7, p. 2353, Jul. 1980, issn: 0305-4470. doi: `10.1088/0305-4470/13/7/018`. (visited on 04/24/2023).

[7] H. Carmichael, *Statistical Methods in Quantum Optics 1: Master Equations and Fokker-Planck Equations*. Springer Science & Business Media, 1999, ISBN: 978-3-540-54882-9.

[8] A. Gilchrist, C. W. Gardiner, and P. D. Drummond, "Positive P representation: Application and validity," *Physical Review A*, vol. 55, no. 4, pp. 3014–3032, Apr. 1997. DOI: `10.1103/PhysRevA.55.3014`.

[9] P. D. Drummond, "Fundamentals of higher order stochastic equations," *Journal of Physics A: Mathematical and Theoretical*, vol. 47, no. 33, p. 335 001, Aug. 2014, ISSN: 1751-8121. DOI: `10.1088/1751-8113/47/33/335001`.

[10] P. D. Drummond, "Higher-order stochastic differential equations and the positive Wigner function," *Physical Review A*, vol. 96, no. 6, p. 062 104, Dec. 2017. DOI: `10.1103/PhysRevA.96.062104`.

[11] M. K. Olsen and A. S. Bradley, "Numerical representation of quantum states in the positive-P and Wigner representations," *Optics Communications*, vol. 282, no. 19, pp. 3924–3929, Oct. 2009, ISSN: 0030-4018. DOI: `10.1016/j.optcom.2009.06.033`.

[12] C. Rackauckas and Q. Nie, "Differentialequations.jl–a performant and feature-rich ecosystem for solving differential equations in julia," *Journal of Open Research Software*, vol. 5, no. 1, p. 15, 2017.

Chapter 9

OUTLOOK

The field of lithium niobate nanophotonics has grown rapidly during these past few years (see Fig. 9.1). At the beginning of my time at Caltech, only electro-optic modulators [1] and second-harmonic generation [2] had been demonstrated on this plaftorm. Now there are optical parametric amplifiers and generators [3], [4], doubly-resonant and triply-resonant optical parametric oscillators [5]–[7], electro-optic frequency combs [8], supercontinuum generators [9], ultrafast switches [10], external cavity tunable lasers [11], and even a rudimentary quantum information processor [12], just to name a few. Indeed, a comprehensive review of the field from 2021 is already outdated [13].

After this rapid development of fundamental building blocks, the following years promise the arrival of increasingly complex nonlinear integrated systems. It is not hard to speculate about specific advancements, especially when closely related to the content of this thesis.

9.1 Visible to mid-infrared tunable sources

The results from this thesis show the feasibility of having a compact laser source capable of replacing several individual laser diodes, which was the main motiva-

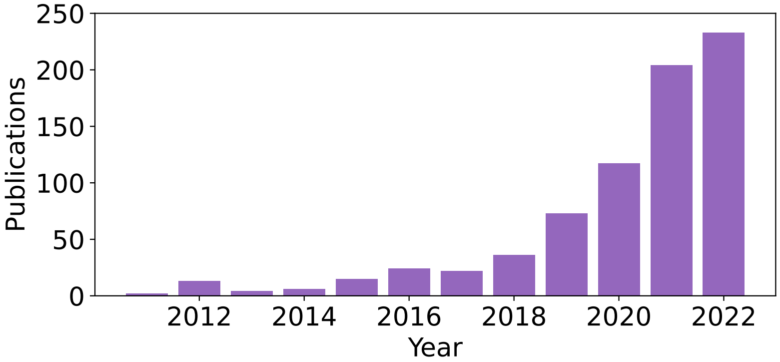

Figure 9.1: **Lithium niobate nanophotonics publications.** Total number of publications as indexed by Google Scholar (https://scholar.google.com/) having titles that include either of the following: “lithium niobate on insulator,” “lithium niobate nanophotonics,” “thin film lithium niobate,” or the corresponding abbreviations.

tion outlined in the introduction. Some future and ongoing developments include an extension of the tuning range, further enhancements in output power, and the demonstration of single mode operation that may be required by some applications.

The tuning range can be most easily extended by using a diode pump that can be tuned over more than 10 nm. Indeed, there are already efforts underway to produce tunable semiconductor lasers based on sampled grating DBR (SGDBR) designs, which include a gain section, a phase section, and front and back SGDBR mirrors [14]. Preliminary results show tuning ranges of more than 30 nm around a 1030 nm wavelength [15]. Another promising alternative is to harness the optical feedback from the TFLN chip to produce a tunable pump starting from a semiconductor gain chip [11]. Such pump can be integrated on the same chip as the OPO, it might be tunable over the entire semiconductor gain bandwidth, and it also inherently solves any issues related to optical feedback instabilities.

The tuning range of a single OPO can be further enhanced by implementing multiple poling periods on the same OPO. Moreover, since the wavelength coverage of the OPO appears to be limited by the loss of the SiO_2 buffer layer, a similar design with a different buffer layer material can allow operation towards the entire lithium niobate transparency window [16]. The OPO design we demonstrate here can also be readily applied to other emerging nonlinear photonic platforms with transparency windows deeper into the mid-infrared [17].

The output range of OPOs can be extended to visible wavelengths by additional $\chi^{(2)}$ processes. For instance, as shown in Fig. 9.2, red-green-blue (RGB) sources can be obtained from an OPO pumped at 1064 nm, with a signal at 1560 nm and an idler at 3346 nm as follows: red light at ~632 nm is obtained by sum-frequency generation of the signal and pump; green light at 532 nm can be generated directly from the second harmonic of the pump; blue light at 450 nm comes from the sum-frequency generation of the signal and the red light. Since only the signal is used, the OPO can be set to be singly resonant for the idler wave.

The maximum conversion efficiency of our on-chip OPOs is dominated by the escape efficiency, which is related to the ratio of output coupler transmittance to total resonator losses. For our devices, this ratio is ~9% at 1950 nm, indicating that the output coupling is small compared to the total losses in the resonator. This could be caused in part by the little transmission of the output coupler, particularly at mid-infrared wavelengths, and in part by intrinsic resonator losses and losses at the input coupler. Fine tuning of the coupler designs and reducing the cavity loss

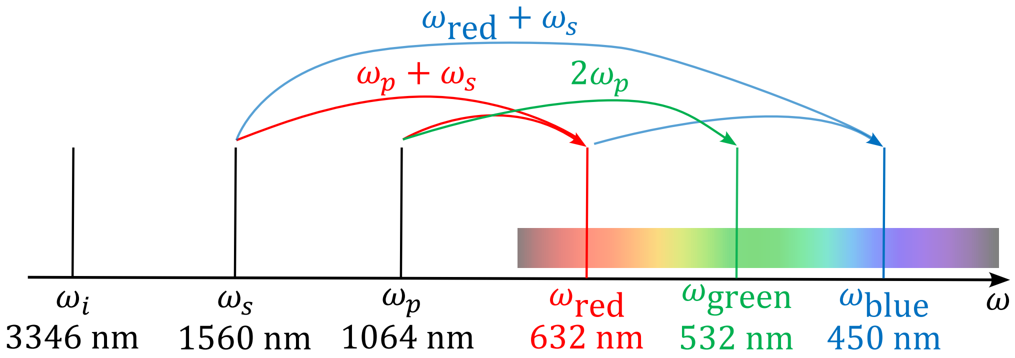

Figure 9.2: **Red-green-blue generation from infrared OPOs.** The output range of infra-red OPOs can be extended to visible wavelengths by additional $\chi^{(2)}$ processes like sum-frequency generation.

can lead to substantial improvement of efficiency. We used adiabatic couplers in this work since they provide a simple means to approximately achieve our requirements of high signal and idler coupling together with low pump coupling. However, the input coupler should, ideally, have 100% coupling at signal and idler frequencies since any transmission in this coupler behaves as additional resonator loss, leading to higher thresholds and lower efficiencies. Simultaneously, the input coupler should provide very low coupling at the pump wavelength, since any coupling just leaks pump power into the unused port, and also provides an undesired feedback path for the pump. These characteristics may be achievable through more advanced coupler designs such as those obtained by inverse design methods [18].

Continuous tuning of the OPO outputs may require a complex algorithm in order to exploit the interplay between all the tuning variables in a doubly-resonant OPO. An alternative would be to start developing singly-resonant OPOs if all the trade-offs among threshold, tunability, and output power turn out to be beneficial. This may be the case, for instance, in pulsed applications.

Applications requiring single spectral modes with high coherence would need modifying the OPO design. For example, an additional resonator can be added in other to increase the effective free spectral range and limit oscillation to a single mode. An electro-optic modulator on the additional resonator would enable hopping between adjacent longitudinal modes of the main resonator [19]. Continuous mode-hop-free tuning of such nested resonators can also be achieved by a coordinated shifts in both resonators [20].

OPOs offer a large number of options in terms of coherence and frequency stabilization due to the different frequencies involved and potential for additional $\chi^{(2)}$ processes like sum-frequency generation. The OPO outputs can be stabilized directly to a reference cavity achieving a few kilohertz of relative stability over hours [21]. They can also be absolutely locked to atomic transitions, for instance, in Ref. [22], the OPO signal at 852 nm was locked to a hyperfine transition of Cs over several minutes. Such method could be extended to the infrared, for example, using the same Cs transition to lock a signal at 1704 nm trough frequency doubling.

9.2 Frequency combs and ultrashort pulse generation

Fully stabilized frequency combs have revolutionized the field of precision metrology [23]. There are several ways in which an integrated platform with a $\chi^{(2)}$ nonlinearity can benefit this field. A promising route was shown by Roy [24], in which a picosecond electro-optic comb can be used to pump a degenerate OPO generating a femtosecond signal based on walk-off induced quadratic solitons. This approach can be combined with the generation of on-chip electro-optic combs [8] to deliver a CW pumped femtosecond source in the mid-infrared.

Another interesting path involves coherent supercontinuum generation by simultaneous and cascaded $\chi^{(2)}$ processes like sum-frequency generation or intra-pulse difference-frequency generation. We estimate that this could lead to coherent frequency combs covering several octaves, and even the full transparency window of lithium niobate.

References

[1] C. Wang, M. Zhang, X. Chen, M. Bertrand, A. Shams-Ansari, S. Chandrasekhar, P. Winzer, and M. Lončar, “Integrated lithium niobate electro-optic modulators operating at CMOS-compatible voltages,” *Nature*, vol. 562, no. 7725, p. 101, Oct. 2018, ISSN: 1476-4687. DOI: `10.1038/s41586-018-0551-y`.

[2] C. Wang, C. Langrock, A. Marandi, M. Jankowski, M. Zhang, B. Desiatov, M. M. Fejer, and M. Lončar, “Ultrahigh-efficiency wavelength conversion in nanophotonic periodically poled lithium niobate waveguides,” *Optica*, vol. 5, no. 11, pp. 1438–1441, Nov. 2018, ISSN: 2334-2536. DOI: `10.1364/OPTICA.5.001438`.

[3] L. Ledezma, R. Sekine, Q. Guo, R. Nehra, S. Jahani, and A. Marandi, “Intense optical parametric amplification in dispersion-engineered nanophotonic lithium niobate waveguides,” *Optica*, vol. 9, no. 3, pp. 303–308, Mar. 2022, ISSN: 2334-2536. DOI: `10.1364/OPTICA.442332`.

[4] M. Jankowski, M. Jankowski, M. Jankowski, N. Jornod, N. Jornod, C. Langrock, B. Desiatov, A. Marandi, M. Lončar, and M. M. Fejer, “Quasi-static optical parametric amplification,” *Optica*, vol. 9, no. 3, pp. 273–279, Mar. 2022, ISSN: 2334-2536. DOI: `10.1364/OPTICA.442550`.

[5] J. Lu, A. A. Sayem, Z. Gong, J. B. Surya, C.-L. Zou, and H. X. Tang, “Ultralow-threshold thin-film lithium niobate optical parametric oscillator,” *Optica*, vol. 8, no. 4, pp. 539–544, Apr. 2021, ISSN: 2334-2536. DOI: `10.1364/OPTICA.418984`.

[6] L. Ledezma, A. Roy, L. Costa, R. Sekine, R. Gray, Q. Guo, R. M. Briggs, and A. Marandi, “Widely-tunable optical parametric oscillator in lithium niobate nanophotonics,” *arXiv:2203.11482 [physics]*, Mar. 2022. arXiv: `2203.11482 [physics]`.

[7] A. Roy, L. Ledezma, L. Costa, R. Gray, R. Sekine, Q. Guo, M. Liu, R. M. Briggs, and A. Marandi, “Visible-to-mid-IR tunable frequency comb in nanophotonics,” *arXiv*, Dec. 2022. DOI: `10.48550/arXiv.2212.08723`.

[8] M. Zhang, B. Buscaino, C. Wang, A. Shams-Ansari, C. Reimer, R. Zhu, J. M. Kahn, and M. Lončar, “Broadband electro-optic frequency comb generation in a lithium niobate microring resonator,” *Nature*, vol. 568, no. 7752, pp. 373–377, Apr. 2019, ISSN: 1476-4687. DOI: `10.1038/s41586-019-1008-7`.

[9] M. Jankowski, C. Langrock, B. Desiatov, A. Marandi, C. Wang, M. Zhang, C. R. Phillips, M. Lončar, and M. Fejer, “Ultrabroadband nonlinear optics in nanophotonic periodically poled lithium niobate waveguides,” *Optica*, vol. 7, no. 1, pp. 40–46, 2020.

[10] Q. Guo, R. Sekine, L. Ledezma, R. Nehra, D. J. Dean, A. Roy, R. M. Gray, S. Jahani, and A. Marandi, “Femtojoule femtosecond all-optical switching in lithium niobate nanophotonics,” *Nature Photonics*, pp. 1–7, Jul. 2022, ISSN: 1749-4893. DOI: `10.1038/s41566-022-01044-5`.

[11] M. Li, L. Chang, L. Wu, J. Staffa, J. Ling, U. A. Javid, S. Xue, Y. He, R. Lopez-rios, T. J. Morin, H. Wang, B. Shen, S. Zeng, L. Zhu, K. J. Vahala, J. E. Bowers, and Q. Lin, “Integrated Pockels laser,” *Nature Communications*, vol. 13, no. 1, p. 5344, Sep. 2022, ISSN: 2041-1723. DOI: `10.1038/s41467-022-33101-6`.

[12] R. Nehra, R. Sekine, L. Ledezma, Q. Guo, R. M. Gray, A. Roy, and A. Marandi, “Few-cycle vacuum squeezing in nanophotonics,” *Science*, vol. 377, no. 6612, pp. 1333–1337, Sep. 16, 2022. DOI: `10.1126/science.abo6213`.

[13] D. Zhu, L. Shao, M. Yu, R. Cheng, B. Desiatov, C. J. Xin, Y. Hu, J. Holzgrafe, S. Ghosh, A. Shams-Ansari, E. Puma, N. Sinclair, C. Reimer, M. Zhang, and M. Lončar, “Integrated photonics on thin-film lithium niobate,” *Advances in Optics and Photonics*, vol. 13, no. 2, pp. 242–352, Jun. 2021, ISSN: 1943-8206. DOI: `10.1364/AOP.411024`.

[14] P. A. Verrinder, L. Wang, J. Fridlander, F. Sang, V. Rosborough, M. Nickerson, G. Yang, M. Stephen, L. Coldren, and J. Klamkin, “Gallium arsenide photonic integrated circuit platform for tunable laser applications,” *IEEE Journal of Selected Topics in Quantum Electronics*, vol. 28, no. 1, pp. 1–9, 2021.

[15] P. A. Verrinder, L. Wang, J. Fridlander, F. Sang, V. Rosborough, M. Nickerson, G. Yang, M. Stephen, L. Coldren, and J. Klamkin, “Gallium Arsenide Photonic Integrated Circuit Platform for Tunable Laser Applications,” *IEEE Journal of Selected Topics in Quantum Electronics*, vol. 28, no. 1: Semiconductor Lasers, pp. 1–9, Jan. 2022, ISSN: 1558-4542. DOI: `10.1109/JSTQE.2021.3086074`.

[16] J. Mishra, T. P. McKenna, E. Ng, H. S. Stokowski, M. Jankowski, C. Langrock, D. Heydari, H. Mabuchi, M. M. Fejer, and A. H. Safavi-Naeini, “Mid-infrared nonlinear optics in thin-film lithium niobate on sapphire,” *Optica*, vol. 8, no. 6, pp. 921–924, Jun. 2021, ISSN: 2334-2536. DOI: `10.1364/OPTICA.427428`.

[17] R. Becheker, M. Bailly, S. Idlahcen, T. Godin, B. Gerard, H. Delahaye, G. Granger, S. Fèvrier, A. Grisard, E. Lallier, and A. Hideur, “Optical parametric generation in OP-GaAs waveguides pumped by a femtosecond fluoride fiber laser,” *Optics Letters*, vol. 47, no. 4, pp. 886–889, Feb. 2022, ISSN: 1539-4794. DOI: `10.1364/OL.443896`.

[18] S. Molesky, Z. Lin, A. Y. Piggott, W. Jin, J. Vucković, and A. W. Rodriguez, “Inverse design in nanophotonics,” *Nature Photonics*, vol. 12, no. 11, pp. 659–670, Nov. 2018, ISSN: 1749-4893. DOI: `10.1038/s41566-018-0246-9`.

[19] D. J. M. Stothard, I. D. Lindsay, and M. H. Dunn, “Continuous-wave pump-enhanced optical parametric oscillator with ring resonator for wide and continuous tuning of single-frequency radiation,” *Optics Express*, vol. 12, no. 3, pp. 502–511, Feb. 2004, ISSN: 1094-4087. DOI: `10.1364/OPEX.12.000502`.

[20] P. Groß, I. D. Lindsay, C. J. Lee, M. Nittmann, T. Bauer, J. Bartschke, U. Warring, A. Fischer, A. Kellerbauer, and K.-J. Boller, “Frequency control of a 1163 nm singly resonant OPO based on MgO:PPLN,” *Optics Letters*, vol. 35, no. 6, pp. 820–822, Mar. 2010, ISSN: 1539-4794. DOI: `10.1364/OL.35.000820`.

[21] O. Mhibik, T.-H. My, D. Pabœuf, F. Bretenaker, and C. Drag, “Frequency stabilization at the kilohertz level of a continuous intracavity frequency-doubled singly resonant optical parametric oscillator,” *Optics Letters*, vol. 35, no. 14, pp. 2364–2366, Jul. 2010, ISSN: 1539-4794. DOI: `10.1364/OL.35.002364`.

[22] S. Zaske, D.-H. Lee, and C. Becher, “Green-pumped cw singly resonant optical parametric oscillator based on MgO:PPLN with frequency stabilization to an atomic resonance,” *Applied Physics B*, vol. 98, no. 4, pp. 729–735, Mar. 2010, ISSN: 1432-0649. DOI: `10.1007/s00340-009-3871-7`.

[23] S. A. Diddams, K. Vahala, and T. Udem, “Optical frequency combs: Coherently uniting the electromagnetic spectrum,” *Science*, vol. 369, no. 6501, eaay3676, 2020.

[24] A. Roy, R. Nehra, S. Jahani, L. Ledezma, C. Langrock, M. Fejer, and A. Marandi, “Temporal walk-off induced dissipative quadratic solitons,” *Nature Photonics*, vol. 16, no. 2, pp. 162–168, Feb. 2022, ISSN: 1749-4893. DOI: `10.1038/s41566-021-00942-4`.